SYNTHESIS AND CHARACTERIZATION OF ZIRCONIUM TUNGSTATE-ZIRCONIA CORE-SHELL COMPOSITE PARTICLES

A THESIS SUBMITTED TO
THE GRADUATE SCHOOL OF NATURAL AND APPLIED SCIENCES
OF
MIDDLE EAST TECHNICAL UNIVERSITY

BY

NASSER KHAZENI

IN PARTIAL FULFILLMENT OF THE REQUIREMENTS
FOR
THE DEGREE OF MASTER OF SCIENCE
IN
CHEMICAL ENGINEERING

JANUARY 2013

Approval of the thesis:

SYNTHESIS AND CHARACTERIZATION OF ZIRCONIUM TUNGSTATE-ZIRCONIA CORE-SHELL COMPOSITE PARTICLES

submitted by **NASSER KHAZENI** in partial fulfillment of the requirements for the degree of **Master of Science in Chemical Engineering Department, Middle East Technical University** by,

Prof. Dr. Canan Özgen _____
Dean, Graduate School of **Natural and Applied Sciences**

Prof. Dr. Deniz Üner _____
Head of Department, **Chemical Engineering Dept.**

Prof. Dr. Güngör Gündüz _____
Supervisor, **Chemical Engineering Dept., METU**

Assoc. Prof. Dr. Bora Maviş _____
Co-supervisor, **Mechanical Engineering Dept., HU**

Examining Committee Members:

Prof. Dr. Gürkan Karakaş _____
Chemical Engineering Dept., METU

Prof. Dr. Güngör Gündüz _____
Chemical Engineering Dept., METU

Prof. Dr. H. Önder Özbelge _____
Chemical Engineering Dept., METU

Prof. Dr. Macit Özenbaş _____
Metallurgical and Materials Dept., METU

Asst. Prof. Zeynep Çulfaz Emecen _____
Chemical Engineering Dept., METU

Date: **15.01.2013**

I hereby declare that all information in this document has been obtained and presented in accordance with academic rules and ethical conduct. I also declare that, as required by these rules and conduct, I have fully cited and referenced all material and results that are not original to this work.

Name, Last name : NASSER KHAZENI

Signature :

ABSTRACT

SYNTHESIS AND CHARACTERIZATION OF ZIRCONIUM TUNGSTATE-ZIRCONIA CORE-SHELL COMPOSITE PARTICLES

Khazeni, Nasser
M.Sc., Department of Chemical Engineering
Supervisor : Prof. Dr. Güngör Gündüz
Co-Supervisor : Assist. Prof. Dr. Bora Maviş

January 2013, 82 pages

Thermal mismatch between different components of a system could cause of problems like residual stress induced cracking, thermal fatigue or even optical misalignment in certain high technology applications. Use of materials with customized thermal expansion coefficient is a counter-measure to resolve such problems. Zirconium tungstate (ZrW_2O_8) with negative thermal expansion coefficient is capable of being used in synthesis of composites with tailored coefficient of thermal expansion (CTE). In this work, the sol-gel method which had been already set up in our group was characterized and the sources of the factors imposing impurities in the product were distinguished in all the steps of precursor preparation and heat treatment. In the second part of study, zirconium tungstate particles synthesized by the sol-gel method were utilized as core in synthesis of ZrW_2O_8–ZrO_2 core–shell composite particles. Shell layer was composed of ZrO_2 nanocrystallites and precipitated from an aqueous solution by urea hydrolysis. Volume of the shell was effectively controlled by concentration of the initial zirconium ion in the solutions. The rate of precipitation was a function of the ratio of initial urea concentration to zirconium ion. It is hypothesized that isolation of the ZrW_2O_8 within a layer of ZrO_2, will be a key element in solving problems associated with reactivity of ZrW_2O_8 towards other components in sintering of ceramic–ceramic composites with tuned or zero thermal expansion coefficient.

Keywords: ceramics, multilayers, chemical synthesis, X-ray diffraction, thermal expansion, composites.

ÖZ

ZİRKONYUM TUNGSTAT – ZİRKONYA GÖBEK – KABUK KARMA PARÇACIKLARIN SENTEZİ VE YAPISAL TANIMLAMASI

Khazeni, Nasser
Yüksek Lisans, Kimya Mühendisliği Bölümü
Tez Yöneticisi : Prof. Dr. Güngör Gündüz
Ortak Tez Yöneticisi : Yrd. Doç. Dr. Bora Maviş

Ocak 2013, 82 sayfa

Bir sistemin farklı bileşenleri arasındaki ısıl uyumsuzluk kimi yüksek teknoloji uygulamalarında artık gerilim nedenli çatlamalara, ısıl yorulmaya ve hatta optik hizalanma problemlerine yol açabilmektedir. Bu tür problemlerin çözümüne yönelik olarak ısıl genleşme sabitleri ayarlanmış malzemeler kullanılabilir. Negatif ısıl genleşme sabitine sahip zirkonyum tungstat (ZrW_2O_8) ayarlanmış ısıl genleşme sabitine (IGS) sahip karma malzemelerin sentezinde kullanılabilir. Bu çalışmada öncelikle, ZrW_2O_8 üretiminde kullanılmak üzere daha önce grubumuzda geliştirilmiş olan bir çöz-pel yönteminin ürünleri daha detaylı incelenmiş ve ürünlerde görülen safsızlıkların kaynağı olan etmenler, çöz-pel öncülünün kimyasal hazırlığı ve ısıl işlem basamakları için ayrı ayrı incelenmiştir. Çalışmanın ikinci bölümünde ise, gerekli değişikliklerin yapıldığı yöntemle üretilen zirkonyum tungstat parçacıklar, ZrW_2O_8–ZrO_2 göbek–kabuk karma parçacıklarının üretiminde kullanılmıştır. Kabuk katmanı, ZrO_2 nanokristalciklerinden oluşmuş ve sulu çözeltiden üre hidrolizi ile çökeltilmiştir. Kabuk katmanın hacmi çözeltideki başlangıç zirkonyum iyon derişimi ile etkili bir biçimde kontrol edilebilmiştir. Çökeltme tepkimesinin hızı başlangıç üre ve zirkonyum iyonlarının derişim oranlarına bağıntılı olarak değişiklik göstermiştir. ZrW_2O_8'ın ZrO_2 gibi bir katman ile yalıtılmasının, ayarlanmış ya da sıfır ısıl genleşme gösterecek seramik – seramik karma malzemelerin pişirilmesi sırasında ortaya çıkan ve ZrW_2O_8'ın diğer bileşene karşı tepkinirliğiyle ilgili olan problemlerin çözümünde kilit bir rol oynayacağı öngörülmektedir.

Anahtar sözcükler: seramik, çok-katmanlı yapılar, kimyasal sentez yöntemleri, X-ışınları kırınımı, ısıl genleşme, kompozit.

To Faezeh, Tasnim and My Parents

ACKNOWLEDGEMENTS

I would like to express my deepest gratitude to my supervisor Prof. Dr. Güngör Gündüz for his expertise and guidance throughout my studies. I cannot thank him enough for his encouragement, understanding, patience, and for these enlightening period during which I had the chance to work with him.

I would like to express my sincere thanks to my co-supervisor, Assist. Prof. Dr. Bora Maviş, for his endless helps, great ideas, guiding the research discussions, and for his enthusiastic motivating manner during my thesis research period.

I would like to express my sincere thanks to Prof. Dr. Üner Çolak for his invaluable advice, support, understanding, and kind attitude in every aspect.

I would like to thank METU Central Laboratory and Bilkent University Institute of Material Science and Nanotechnology – National Nanotechnology Research Center staff for characterization analyses. My special thanks go to Necmi Avcı from Metallurgical and Materials Engineering Department of METU for his endless help on XRD analysis.

Thanks are not enough to my laboratory friends Berker Özerciyes, Nihan Karakoç, Gülden Eroğlu, Simge Çınar, Berna Burcu Topuz, Nagehan Keskin, Anisa Çoniku, İdil Öğretim and Erkan Biber for their collaborative, motivating and friendly manner. I would like to thank İrem Vural, Korhan Sezgiker, Sevinç Sevim Kahya and Yashar Tavakkoli for helping me get through the difficult times and for all the supports. Their assistance through the course of this thesis is invaluable.

My deepest gratitude goes to my parents for their unflagging love and support throughout my life; this dissertation is simply impossible without them.

Last but not least, I owe my loving thanks to my wife Faezeh, who has been my biggest support all the way not only through my academic studies but also through my life. The words are not enough to express my appreciation to her for his dedication, love and persistent confidence in me.

The supports received from The Science and Technical Research Council of Turkey (TÜBİTAK) (Project Number: 107M006) and Middle East Technical University (METU) (Scientific Research Projects: BAP-2008-03-04-01 and BAP-07-02.2009.00.01) are gratefully acknowledged.

TABLE OF CONTENTS

ABSTRACT v
ÖZ vi
ACKNOWLEDGEMENTS viii
TABLE OF CONTENTS ix
LIST OF TABLES x
LIST OF FIGURES xii
LIST OF SYMBOLS AND ABBREVIATIONS xiii
CHAPTERS
1. INTRODUCTION 1
2. LITERATURE REVIEW 5
2.1 Thermal Properties of Solid Materials 5
2.2 Origin of Negative Thermal Expansion 7
2.3 Room Temperature Structure of Zirconium Tungstate 10
2.4 NTE of Zirconium Tungstate - High Temperature Structure 11
2.5 NTE of Zirconium Tungstate - High Pressure Structure 13
2.6 High Pressure-High Temperature Structure 18
2.7 Production Methods: Solid State Reaction 18
2.8 Production Methods: Wet Chemical Methods 21
2.8.1 Wet Chemical Methods: Combustion 22
2.8.2 Wet Chemical Methods: Co-precipitation 23
2.8.3 Wet Chemical Methods: Hydrothermal 25
2.8.4 Wet Chemical Methods: Sol-Gel 25
2.9 Zirconia as Composite Counterpart with Zirconium Tungstate 26
3. EXPERIMENTAL 29
3.1 Materials 29
3.1.1 Tungstic Acid (TA) and Ammonia 29
3.1.2 Zirconium(IV) Acetate (ZrAc) 29
3.1.2 Zirconium(IV) Oxychloride (ZrOc) and Urea 30
3.2 Modification of Synthesis of Zirconium Tungstate 30
3.2.1 Recipe of Sol-Gel Method 30
3.2.2 Modified Sol-Gel Method 30
3.2.3 Effect of pH of ATA Solution on Product Composition 31
3.3 Synthesis of ZrW_2O_8/ZrO_2 Core-Shell Composite Particles 32
3.4 Characterization Methods 33
3.4.1 XRD (X-ray Diffraction) Analysis 33
3.4.2 PSA (Particle Size Analysis) 33
3.4.3 SEM (Scanning Electron Microscope) Analysis 33
4. RESULTS AND DISCUSSIONS 35
4.1 Preliminary Study on Sol-gel Synthesis of ZrW_2O_8 35
4.2 Modifications on Sol-Gel Method 36
4.3 ZrO_2-ZrW_2O_8 Core-Shell Composite Particles 41
4.3.1 Synthesis 41
4.3.2 Reaction Analysis 43
4.3.3 Composition and Phase Analyses 44
5. CONCLUSIONS 53
6. RECOMMENDATIONS 55
REFERENCES 57
APPENDICES
A. XRD STANDARD PEAKS 63
B. CREATION OF XRD PEAKS 69

C. DECONVOLUTION OF XRD PEAKS 75

LIST OF TABLES

TABLES

Table 2.1 Ceramics categories based on their magnitude of CTE's. 7
Table 2.2 Oxide framework work structure capable of rocking in RUM based on $A_xM_yO_{3x+2y}$ formula. 9
Table 2.3 Fractional atom coordinates in ZrW_2O_8 unit cell at room temperature [1].....10
Table 2.4 Lattice parameter of zirconium tungstate as a function of temperature calculated from neutron and X-ray diffraction analyses as well as attributed space group. Neither $P2_13$ nor $Pa3$ could be attributed to the data belonging to 423K [1].....13
Table 2.5 Fractional atom sites in γ-ZrW_2O_8 unit cell at room temperature [41]. 15
Table 2.6 Important studies in which solid state reaction has been adopted to produce zirconium tungstate. 20
Table 2.7 Studies in which combustion method was adopted to produce zirconium tungstate.....23
Table 2.8 Studies in which sol-gel method has been adopted to produce zirconium tungstate. Hydrolytic sol-gel methods can be distinguished by existence of water in "Starting Materials" column. 27
Table 3.1 Experiments conducted to modify the sol-gel method to achieve phase pure product in which combination of modifications in both precursor and heat treatment levels has been considered in each experiment. 31
Table 3.2 Composition and pH of five ATA solutions prepared to investigate the effect of pH of ATA solution on composition of the product.....31
Table 3.3 Conditions of precipitation experiments. 32
Table 4.1 Phase mixture of the products yielded from precursors with varied pH values of ATA solution. 40
Table 4.2 Phase mixture of the products of different experiments. 43
Table A.1 Standard XRD pattern of different phases of ZrW_2O_8. 63
Table A.2 Standard XRD pattern of $ZrW_2O_7(OH)_2 \cdot 2(H_2O)$. 65
Table A.3 Standard XRD pattern of WO_3. 65
Table A.4 Standard XRD pattern of different phases of ZrO_2. 66
Table B.1 Data table associated with XRD pattern of γ-ZrW_2O_8. 71
Table C.1 Calculation pad of composites compositions produced in experiment A to D*. 80

LIST OF FIGURES

FIGURES

Figure 1.1 Phase diagram of WO_3-ZrO_2 binary system [4]. 2
Figure 2.1 Typical potential energy versus interatomic distance curve [18]. 5
Figure 2.2 Schematic illustration of lattice waves propagated by vibration of atoms of a crystal [18]. 6
Figure 2.3 Schematic crystal structure of AM_2O_7 and AM_2O_8 in cubic symmetry viewed down [001]. Shaded polyhedra are AO_6 octahedra [34]. 9
Figure 2.4 Thermal ellipsoidal (a) and polyhedral (b) representation of zirconium tungstate unit cell [1]. Incomplete unit cell of zirconium tungstate (c) represents alignment of W1 and W2 atoms on threefold axis [36]. 11
Figure 2.5 (a) Result of dilatometric analysis performed on synthesized zirconium tungstate bar from 297K to 593K [39] (b) XRD patterns of zirconium tungstate at 298K, 419K and 509K [1]. 12
Figure 2.6 Thermal ellipsoidal representation of WO_4 groups at high temperature after order-disorder phase transition [1]. 14
Figure 2.7 (a) Polyhedral representation of γ-ZrW_2O_8 unit cell. (b) Ball-bar representation of WO_4 pairs in cubic ZrW_2O_8 along with threefold axis. (c), (d) and (e) Ball-bar representation of distinct WO_4 pairs in γ-ZrW_2O_8. Shaded balls are W and white ones are O. The unit of interatomic distances is Å [41]. 16
Figure 2.8 Unit cell parameters and unit cell volume of γ-ZrW_2O_8 as a function of temperature [43]. 17
Figure 2.9 Structural response of zirconium tungstate to different processing routes involving changes in pressure and temperature. 19
Figure 2.10 Classification of the methods suitable for synthesis of zirconium tungstate. 22
Figure 2.11 Flowchart of H_2O_2 assisted co-precipitation method to synthesize zirconium tungstate from TA and zirconium oxychloride with low temperature heat treatment [61]. 24
Figure 4.1 Fish-bone representation of potential modifications of the sol-gel method developed in our group. 36
Figure 4.2 XRD pattern of a typical specimen prepared by former sol-gel method developed in our group [66]. 37
Figure 4.3 XRD pattern of the products from modified sol-gel experiments. 37
Figure 4.4 XRD pattern of the products treated at different temperatures; 1150, 1140 and 1130°C. 38
Figure 4.5 XRD pattern of the sample prepared to identify the role of alumina type crucible on the purity of the product. 39
Figure 4.6 XRD patterns of the products yielded from precursors with varied pH's of ATA solution. 40
Figure 4.7 XRD patterns of the products yielded from heat treatment of the same calcined mixture; half of mixture was pressed and half was left in powder form. 41
Figure 4.8 XRD patterns of (a) ZrW_2O_8 products used in the production of core–shell particles. (b) A zoomed section (21–25°) from the patterns given in (a) with the marked positions and relative intensities of standard peaks of m-WO_3 and γ-ZrW_2O_8 phases. 42

Figure 4.9 (a) Trends of pH variation with time in different experiments (as the amount of 'core' particles which act as seeds is different in experiment A, this experiment is excluded from the plot), (b) Rate of precipitation with respect to the [Urea]/[$ZrOCl_2$] ratio. Time needed to reach to the deflection point of the pH versus time curves was used as time values of y-axis. 45
Figure 4.10 (a) XRD patterns of core–shell particles produced in experiments. (b) For clarity data are given between 15° and 40° 2θ. Positions and relative intensities of standard peaks of the phases are marked. 46
Figure 4.11 Deconvolution analysis performed on XRD pattern of the product produced in experiment A. The observed peaks between 21.0 to 22.4° (a) and 28.5 to 31.5 (b) were generated and deconvoluted into two and five peaks respectively. 47
Figure 4.12 Relationship between crystallite size of ZrO_2 and ratio of cubic to tetragonal phases of ZrO_2 in the shells of products. 49
Figure 4.13 Sketch of phase transformations during heat treatment of the core–shell particles. After calcination volume of ZrO_2 will be smaller than that of its precursor. 50
Figure 4.14 (a) and (b) SEM micrographs of as-synthesized ZrW_2O_8 particles and (c) and (d) the images of core–shell particles from experiment B. 51
Figure B.1 Different parts of cell creation window. 69
Figure B.2 (a) Cell creation window and (b) crystal structure of γ-ZrW_2O_8. 70
Figure B.3 Dialogue box creation of XRD pattern. 71
Figure B.4 XRD pattern of γ-ZrW_2O_8. 71
Figure C.1 Deconvolution analysis of experiment B. The observed peaks between 21.0 to 22.4° (a) and 28.5 to 31.5 (b) were generated and deconvoluted into two and five peaks respectively. 76
Figure C.2 Deconvolution analysis of experiment C. The observed peaks between 21.0 to 22.4° (a) and 28.5 to 31.5 (b) were generated and deconvoluted into two and five peaks respectively. 77
Figure C.3 Deconvolution analysis of experiment D. The observed peaks between 21.0 to 22.4° (a) and 28.5 to 31.5 (b) were generated and deconvoluted into two and five peaks respectively. 78
Figure C.4 Deconvolution analysis of experiment D*. The observed peaks between 21.0 to 22.4° (a) and 28.5 to 31.5 (b) were generated and deconvoluted into two and five peaks respectively. 79

LIST OF SYMBOLS AND ABBREVIATIONS

α	Linear coefficient of thermal expansion ($°C^{-1}$ or $°F^{-1}$)
ω	Vibration frequency (Hz)
a	Area (m^2)
A	Cations at octahedral sites
ATA	Ammoniacal Tungstic acid
C	Number of topological constraints
CTE	Coefficient of Thermal Expansion
DTA	Differential Thermal Analysis
F	Number of topological degrees of freedom
FT-IR	Fourier Transform Infrared Spectroscopy
FWHM	Full With at Half Maximum
gr	Gram
hr	Hour
K	Kelvin
L	Liter
m	Milli (10^{-3})
M	Cations at tetrahedral sites, Mega (10^{+6})
NTE	Negative Thermal Expansion
α-ZrW_2O_8	Cubic structure of zirconium tungstate at room temperature
γ-ZrW_2O_8	Orthorhombic phase of zirconium tungstate
c-ZrW_2O_8	Cubic (both centro and noncentrosymmetric) ZrW_2O_8
Pa	Pascal (pressure unit in SI system)
PSA	Particle Size Analysis
PSD	Particle Size Distribution
SEM	Scanning Electron Microscopy
SHS	Self-propagating High-temperature Synthesis
T	Temperature (°C)
TA	Tungstic Acid
TGA	Thermogravimetric Analysis
XRD	X-Ray Diffraction
V	Volume (mL)
ZrAc	Zirconium Acetate
ZrOc	Zirconium oxychloride
µm	Micrometer

CHAPTER 1

INTRODUCTION

The most familiar phenomenon observed during exposure of a material to thermal energy is expansion. The phenomenon is so common that quantified index to compare the dimensional change of materials while introducing to the thermal energy has been based on "expansivity" and has been named as "coefficient of thermal expansion", CTE. Therefore, rare number of materials that have a contracting nature with the increase of temperature are represented with negative coefficients. Though accounting for a negligible percent among materials, materials with negative CTE's (NTE) have attracted interests of researchers as a result of their exceptional structure and potential applications.

Thermal expansion is commonly justified by bond stretching as a result of exposure to the thermal energy. Such an explanation implies the bond strength has a core role in the magnitude of CTE. Therefore, near zero CTE is expected from a material with very strong bonds (e.g. of bonds between oxygen and most of transition metals like zirconium). However, NTE is not interpretable by consideration of mere bond behavior. Materials with negative CTE's have crystalline structures and hence, NTE mechanisms must be tracked in the arrangement of atoms within the unit cells and how the arrangement changes to accommodate thermal energy without distortion of the crystal structure. Rotation of polyhedra, change in distribution of interstitial cations, increase in regularity and of transversal vibration is amongst the responses of crystal structures against thermal energy that can lead to overall contraction of crystal structure [1].

Most NTE materials suffer from anisotropic thermal expansion and/or contraction in a limited temperature range. For instance, $PbTiO_3$ has negative CTE in the temperature range around 500ºC. Moreover, as $PbTiO_3$ gains negative CTE when it is in noncubic phase, and so NTE cannot be isotropic [1]. Therefore, any material exhibiting isotropic NTE over a wide range of temperature is considered as an exception and it has been observed in zirconium tungstate. Zirconium tungstate, ZrW_2O_8, retains its cubic structure at ambient pressure over the range of temperature from 0.3 to 1050K. On the other hand, with a transversal vibration mechanism, zirconium tungstate unit cell accommodate thermal energy by contraction with CTE of $-8.7\times10^{-6}K^{-1}$. It is comparable with CTE of moderately expanding materials (e.g. CTE of alumina is $8\times10^{-6}K^{-1}$) [1, 2]. Observation of such exceptional properties in ZrW_2O_8 persuades physicists, materials scientists and chemists to expend their effort on disclosing its structure, setting up the advantageous production methods, synthesizing it in different forms like nanofibers and using it in different composites.

Structurally, zirconium tungstate consists of ZrO_6 octahedra and WO_4 tetraheda. All oxygens of octahedra are shared with tetrahedra. Only one oxygen from each tetrahedron is not shared. Having such a terminal oxygen in the structure lets the M-O-M linkages pivot around O without distortion of crystal structure.

ZrW_2O_8 was firstly synthesized when study of structural stabilization of zirconia in the presence of highly valance cations, i.e. W^{6+}, was aimed in a solid state reaction [3]. Formation of ZrW_2O_8 from 1:2 stoichiometric mixture of ZrO_2 and WO_3 in the temperature range of 1100 to 1250ºC is inferred from phase diagram of binary ZrO_2-WO_3 system (Figure 1.1). Phase diagram gives information about the thermodynamic metastability of ZrW_2O_8 at ambient temperature. Therefore, to prevent the decomposition of ZrW_2O_8 to its constituent

oxides, while cooling the product down from temperatures above 1100ºC, quenching is crucial. Moreover, in any heat treatment operation ZrW_2O_8 available at room temperature would start to decompose at around 777ºC upon heating [2]. Based on these information, solid state reaction followed by quenching was developed as the pioneering method to synthesize ZrW_2O_8. It involves one-week heat treatment of mixed and ground stoichiometric mixture of WO_3 and ZrO_2 at 1200 ºC with intermittent regrinding steps after quenching.

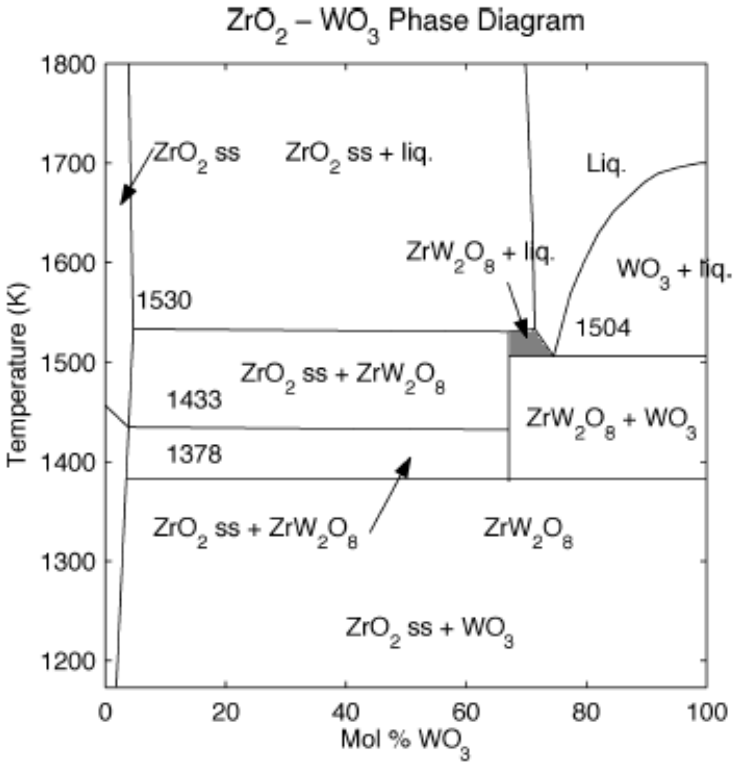

Figure 1.1 Phase diagram of WO_3-ZrO_2 binary system [4].

Solid state method involves inherent difficulties like long reaction time, high reaction temperature, inhomogeneous mixture of reactants, intermittent reprocessing of reaction mixture and loose of control on the physical characteristic of the products. As the subtleties of ZrW_2O_8 synthesis like preserving stoichiometic ratio of constituent oxides adds more considerations to the production by solid state reaction, achieving phase pure product by this method is very intricate. Hence, alternative wet chemical methods have been developed. Hydrolytic [5-7] and nonhydrolytic [8, 9] sol-gel, combustion [7, 10], precipitation [7, 11, 12], and precipitation followed by hydrothermal aging [7, 13-17] are the wet chemical methods that have been adopted. As the methods provide a homogeneous mixture of zirconium and tungsten sources at molecular level, phase pure ZrW_2O_8 could be produced in considerably short reaction times. However, precursor preparation, i.e. ageing, takes long in most of these methods and the time needed to reach to the product from reactants could not be shortened significantly compared to solid state reaction. In addition, the cost of zirconium and tungsten sources applied in these methods is high and large scale production is in stake. In a wet chemical method which makes use of a fairly abundant zirconium source together with a relatively low-cost tungsten source, also the precursor preparation time

could be shortened significantly. This ammonia-assisted sol-gel method that had been studied in our group involved the use of zirconium acetate (ZrAc) and tungstic acid (TA) and the precursor aging time was two hours. However, the purity of the ZrW_2O_8 product could not be increased above 65%. The first aim of this study was optimizing the precursor preparation method and heat treatment conditions to achieve phase pure ZrW_2O_8.

Unless used with a material with positive CTE within a composite, applicability of a material with negative CTE is limited. Production of composites by combining materials with positive and negative CTEs and tuning the CTE of the bulk composite by changing the volume fraction of constituents is important. Such a composite with tailored CTE can be utilized in any application that thermal expansion of different parts of the system must be matched to prevent stresses that would otherwise form. For instance, dental cavity fillers must have the same CTE as teeth have. Otherwise, either cracking or separation will occur. In a special case, the CTE can be tuned on zero. A composite with zero thermal expansion would be a candidate to apply in the systems that cannot tolerate dimensional changes or cyclic thermal stresses (e.g. variety of optics and electronics applications). Regarding isotropic CTE of ZrW_2O_8 in a wide temperature range, ZrW_2O_8 is the best candidate to be utilized as the counterpart with materials that show positive CTE. Nevertheless, thermodynamic and kinetic metastability of ZrW_2O_8 is a constraint that puts burdens in heat treatment steps which in general is an essential part of the synthesis and/or densification steps of the composite production. Especially the volatility of tungsten in the form of WO_3, and reactivity of tungsten towards elements like Y and Al, which exist in the positively expanding potential oxide counterparts of the composites envisioned, have been observed to yield problems like loss of stoichiometry or early and excessive liquefaction. On the other hand, isolation of ZrW_2O_8 particles by a precursor of zirconia to form core-shell composite particles could be a countermeasure to solve specific composite processing challenges (e.g. sintering). In this case the sintering interface will be limited to just the material with positive CTE and zirconia. Since ZrW_2O_8 will be secured inside the zirconia shell and the binary system between the two is well-behaved, this can be expected to decrease ZrW_2O_8's liquefaction tendency which shows itself when ZrW_2O_8 is brought in direct contact with oxides like alumina. Therefore as a second step in this study, precipitation of a thin layer of zirconia precursor on ZrW_2O_8 particles by urea hydrolysis method was aimed to achieve ZrW_2O_8-ZrO_2 core-shell composite particles.

CHAPTER 2

LITERATURE REVIEW

This chapter includes a brief description of thermal properties of solid materials as well as the origin of negative thermal expansion, besides the description of crystal structure of ZrW_2O_8 at room temperature, high temperature and elevated pressure, NTE of ZrW_2O_8, ZrW_2O_8 production methods and ZrW_2O_8-ZrO_2 composite.

2.1 Thermal Properties of Solid Materials

As an atom consists of electron(s) and proton(s), the net force that two approaching atoms exert is the balance between repulsive and attractive forces. There is a specific separation, r_0, where the net force is zero and the two atoms reach to a dynamic equilibrium by vibration around the separation. Equivalently, if potential energy is adopted to develop the discussion, the net energy between the two atoms is summation of repulsive and attractive energies. At the stated equilibrium the net energy reaches to its minimum value, E_0, that is named bonding energy. Therefore, potential energy versus atomic separation plot will form an energy well with minimum at r_0. A typical well is illustrated in Figure 2.1. The magnitude of E_0 and shape of the energy curve is a character for each material which is evidently a function of interatomic bond strength and temperature. For instance, materials with strong bonds form deeper and more symmetric energy wells and the lowest E_0 corresponds to 0K.

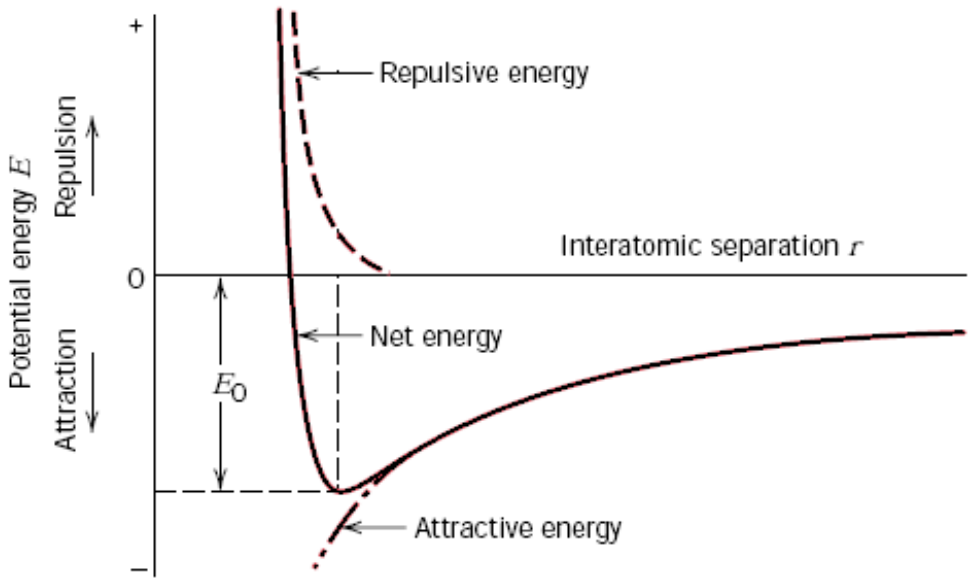

Figure 2.1 Typical potential energy versus interatomic distance curve [18].

From a microscopic point of view, increase in mean interatomic separation leads to expansion of the materials. With increase in temperature the vibrational energy will rise to higher levels in the energy well. Higher energy levels correspond to wider well widths and, therefore, higher mean interatomic separations. It could also be concluded that materials with asymmetric curvature expands more with increases in temperature. On the contrary, materials with deeper and more symmetric well have smaller and even zero expansion.

The discussion developed above ideally involves the treatments of two approaching atoms. But in real condition, especially in solids, complex interactions of more than two atoms must be evaluated. Atoms of a solid material continuously vibrate with low amplitude and high frequency. Having the atoms bound with each other by atomic bond, the vibration of a particular atom cannot be independent of the atom in the neighborhood. The overall effect of vibration and chemical bonding appear in the form of travelling lattice waves, illustrated for a crystal in Figure 2.2. Absorption of thermal energy by a material leads to increase in vibrational energy of the atoms which are made up of lattice waves with specific range of frequencies. Moreover, the magnitudes of vibrational energy are quantized and the smallest package of the energy is named phonon.

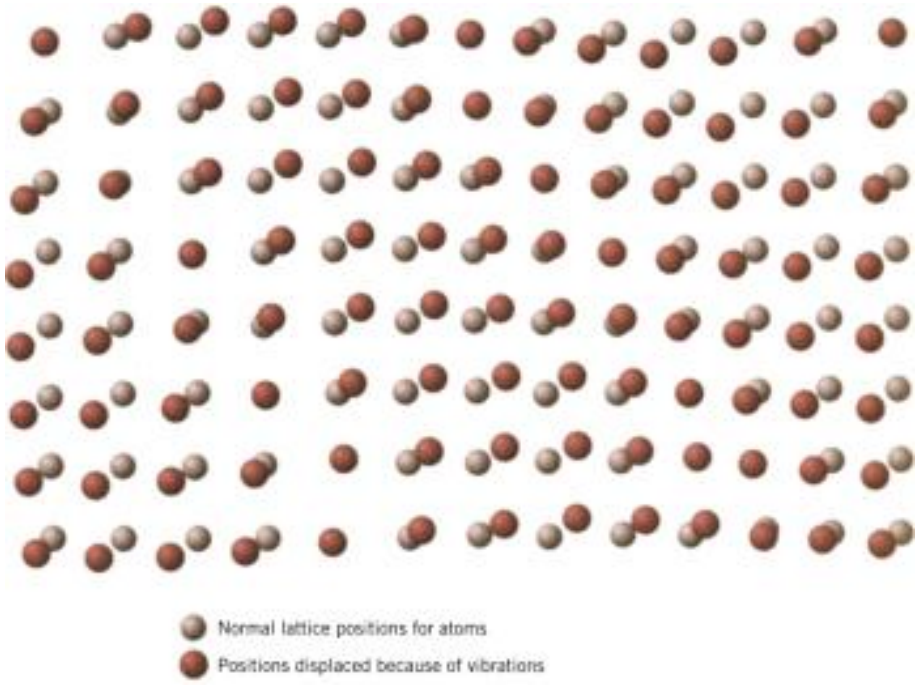

Figure 2.2 Schematic illustration of lattice waves propagated by vibration of atoms of a crystal [18].

Macroscopic response of a material to thermal energy mostly appears in the forms of increase in its dimension. For a material which extended in one dimension, this expansion can be formulated as:

$$\frac{l_f - l_i}{l_i} = \alpha_l (T_f - T_i) \qquad (1)$$

Where l_i and l_f are initial and final length of the material, respectively, for temperature change from T_i to T_f. α_l is a property for materials and is named linear coefficient of thermal expansion and expresses the extend of length increase as a result of exposure to thermal energy. Its unit is $°C^{-1}$ or $°F^{-1}$. For the material state with comparable dimensions at all three coordinates, volumetric increase must be regarded in the expansion formulation [18].

The linear coefficients of thermal expansion for polymers vary from 100 to 200×10^{-6}°C. α_l's of metals are between 10 to 20×10^{-6}°C, an order of magnitude less than polymers. Ceramics have the lowest linear CTE's that vary from 1 to 10×10^{-6}°C [18]. Conventionally, ceramics have been classified into three groups based on their CTE's, namely very low expansion, low expansion and high expansion ceramics which is summarized in Table 2.1 [19].

Table 2.1 Ceramics categories based on their magnitude of CTE's.

Ceramic Category	**CTE range ($\times10^{-6}$°C^{-1})**
Very Low Expansion	$0 \leq \alpha \leq +2$
Low Expansion	$+2 \leq \alpha \leq +8$
High Expansion	$\alpha \geq +8$

2.2 Origin of Negative Thermal Expansion

Expansion is common response of materials to thermal energy. However, there is a group of materials which contract during exposure to thermal energy. Although the contraction mostly happens in a limited temperature range and some members of the group exhibit a directional contraction, the NTE behavior is worthy of attention. It is evident that the interaction of two atoms, i.e. interatomic bonds, which was discussed beforehand, is not capable of interpreting NTE. Bond behavior domain could reach to zero thermal expansion for very strong bonds that plot a deep and symmetric potential well with steep walls. But in crystal structure, atoms could arrange in way that accommodate thermal energy by shrinkage of unit cell. Shrinkage may happen in all three coordinates of unit cell but it is not imperative. In the case that unit cell expand in, e.g. a and b directions, and contract in c direction, if the overall unit cell volume decreases as a result of heating the directional NTE behavior will be observed. Moreover, if the contraction takes place when the crystal is not in cubic phase, even though all three coordinates of unit cell contract, the negative CTE cannot be isotropic. In addition, phase behavior of most crystal structures are temperature dependant. On the other hand, as the response to thermal energy can easily change from contraction to expansion by phase change, the negative thermal expansion is strictly temperature dependent.

There are four known mechanisms for NTE behavior. First mechanism involves the condition when decrease in bond length within a polyhedron leads to decrease in polyhedron distortion. If increase in temperature results in less distorted polyhedron, that it is often so, temperature increase will decrease the average bond length to reach to a regular polyhedron. NTE have been seen just before phase transition in $BaTiO_3$ and $PbTiO_3$ with perovskite structures [20, 21]. It was attributed to mean decrease in Ti-O bond lengths in TiO_6 octahedra that get more regular with temperature increase. In the second mechanism as a result of temperature increase bonds would stretch normally, but the stretch lead to the rotation of polyhedra so that a contraction occurs in one or two directions. In this

mechanism, overall volume of structure may decrease slightly. A negligible thermal contraction is observed in cordierite ($Mg_2Al_4Si_50_{18}$) and NZP ($NaZr_2P_3O_{12}$) has been attributed to this mechanism [22]. Having interstitial cation vacancies in the structure and the change in the distribution of the sites as a result of temperature increase can be another source of NTE. This mechanism was suggested for thermal volume contraction in β-eucryptite and NZP [22]. The last mechanism which is the most frequent one among NTE materials is existence of transversal vibration possibility in the crystal structure. NTE of materials with two coordinate cations, e.g. Cu_2O below room temperature, and anions, e.g. SiO_2 above 1000°C, have been attributed to the transversal vibration of Cu at O-Cu-O linkages and O at Si-O-Si linkages, respectively.

It is proposed that special structural geometry can lead to NTE. Such framework structures consist of polyhedral units that share atoms in the corners. The bonds inside such poyhedra must be so tight that polyhedral structure is preserved against thermal fluctuations, example of which is the bond between oxygen and high valence metals (e.g. W-O bond). In addition, as the expansion of tight bonds is negligible, it will not neutralize the NTE results from the rocking motion of polyhedra. On the contrary, the link in the junction point of two polyhedra must be weak enough to facilitate pivoting of two adjacent polyhedra. It has been proven that for a 2D structure [23]:

$$\Delta a \propto -(T/\omega^2) \quad \text{and} \quad \alpha \propto -(1/\omega^2) \qquad (2)$$

Therefore, low frequency of transversal vibration maintains negative thermal expansion. Moreover, as the frequency is closely related to transversal vibrational energy, low energy mode of the vibration is necessary to prevent distortion of polyhedral structure. Such a framework structure that is capable of rocking motion with low energy vibrational mode has been named as rigid unit mode (RUM). Sometimes the pivoting of polyhedra is accompanied with a slight distortion of polyhedra. Such a case has been termed as quasi rigid unit mode, quasi-RUM.

Having RUM(‘s) in the structure is a function of the balance between topological constraints, C, and degrees of freedom, F. If the numbers of constraints are more than that of degrees of freedom the structure is rigid. Otherwise, the structure is “floppy” and, hence, RUM is expected. Having identical F and C in the structure means that the structure is in the border of rigidity and floppiness. It is noteworthy that symmetry decreases the number of constraints; therefore, while counting the constraints, the independent ones must be taken into account [24].

Oxide framework structures with octahedral and/or tetrahedral rigid units account for the main part of material structures capable of rocking in rigid unit phonon mode. The general formula for such frameworks with shared oxygen at all the polyhedral vertices is $A_xM_yO_{3x+2y}$ where M and A are cations with tetrahedral and octahedral building blocks. The well-known families of the structure have been listed in Table 2.2 along with examples for each family and their CTE’s. Table shows that AO_3 family members have RUM in the structure but CTE of the members are positive. On the other hand, $A_2M_3O_{12}$ family exhibit considerable negative CTE without having RUM in the structure. Therefore, having RUM in the structure does not guarantee the NTE effect. AM_2O_7 family (except $ZrV_{2-x}P_xO_7$) which exhibits cubic symmetry at high temperatures is the only group among the framework structures that shows isotropic NTE behavior. Amorphous SiO_2 and Cu_2O also have isotropic NTE below room temperature [25, 26].

AM_2O_7 family consists of one AO_6 octahedron and two MO_4 tetrahedra. Each octahedron AO_6 shares vertices with six MO_4 tetrahedra whereas each MO_4 shares corners with three AO_6

octahedra and one other MO_4 tetrahedron. In other words, each AO_6 octahedra is corner-shared with six M_2O_7 polyhedra (refer to Figure 2.3).

Table 2.2 Oxide framework work structure capable of rocking in RUM based on $A_xM_yO_{3x+2y}$ formula.

x and y values	Family	Examples	α ($\times 10^{-6}K^{-1}$)
x=1, y=0	AO_3	ReO_3, TaO_2F	0.6[a]
x=0, y=1	MO_2	$AlPO_4$-17, silicates	-11.7[b]
x=1, y=1	AMO_5, $AOMO_4$	$NbOPO_4$, $TaOPO_4$	-1.0[c]
x=1, y=2	AM_2O_7	ZrV_2O_7, ThP_2O_7, UP_2O_7	Negative at >100°C[d]
x=2, y=3	$A_2M_3O_{12}$	$Sc_2W_3O_{12}$, $Y_2W_3O_{12}$, $Lu_2W_3O_{12}$	-2.2, -7.0, -6.8[e]

[a] Rocking motion along all three axes [27].
[b] Over 18–300K [28] for $AlPO_4$-17.
[c] For $NbOPO_4$ over 200-400°C for a axis of tetragonal phase [29].
[d] Quasi-RUM structure [26, 30].
[e] Over 10–1073K [31], 15–1373K [32] and 127–627K respectively [33]. No RUM is available for this family [26].

In AM_2O_7 family if each MO_4 tetrahedron restricts its corner linkages to three AO_6 octahedra and one corner is left unshared, another framework with general formula of AM_2O_8 is created. One may imagine that one M_2O_7 polyhedra of AM_2O_7 gets an oxygen atom and splits into two MO_4 tetrahedra so that the split vertices remain unshared and so forms the AM_2O_8 family. Figure 2.3 illustrates the crystal structures of AM_2O_7 and AM_2O_8 family in cubic phase viewed down [001] direction. $ZrMo_2O_8$, ZrW_2O_8 and HfW_2O_8 are members of this family among which ZrW_2O_8 and its isostructure, HfW_2O_8, exhibit isotropic NTE behavior. $ZrW_{2-x}Mo_xO_8$ in which $x \leq 1.5$ can also exhibit cubic symmetry, but $ZrMo_2O_8$ has hexagonal structure [25].

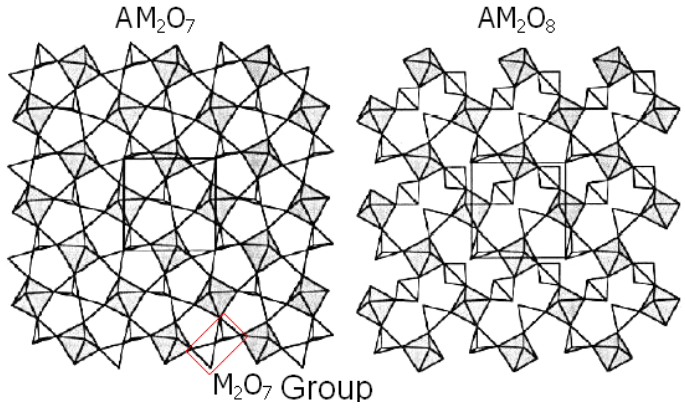

Figure 2.3 Schematic crystal structure of AM_2O_7 and AM_2O_8 in cubic symmetry viewed down [001]. Shaded polyhedra are AO_6 octahedra [34].

2.3 Room Temperature Structure of Zirconium Tungstate

Graham who discovered zirconium tungstate phase during his study on stabilization of zirconia structure by tungsten oxide utilized XRD pattern analysis and attributed a cubic structure for the new phase with unit cell edge of 9.154Å at room temperature [3]. In the later studies both X-ray and neutron powder diffraction data were utilized examples of which are Auray's [35] and Evans's [1]. Both studies approved cubic structure for zirconium tungstate. Though comparable, the calculated lattice parameters slightly differed from Graham's value, 9.1546Å and 9.1575Å respectively. The studies also proved a noncentrosymmetric nature for cubic structure; hence, $P2_13$ (No. 198) was assigned as the space group. Positions of atoms in the unit cell are tabulated in Table 2.3.

Table 2.3 Fractional atom coordinates in ZrW_2O_8 unit cell at room temperature [1].

Atom	x/a	y/b	z/c
Zr1	0.0004	0.0004	0.0004
W1	0.3409	0.3409	0.3409
W2	0.6009	0.6009	0.6009
O1	0.0529	-0.2069	-0.0619
O2	0.0697	-0.0575	0.2132
O3	0.4941	0.4941	0.4941
O4	0.2322	0.2322	0.2322

Figure 2.4(a) illustrates the positions of atoms in thermal ellipsoids representation which is indicative of anisotropic thermal vibration of atoms in the crystal structure and hence position of atoms in the structure. Properly linking the oxygen atoms ellipsoids by imaginary lines will lead to polyhedral representation of zirconium tungstate structure which is the same as aforementioned AM_2O_8 framework structure. The structure is made up of ZrO_6 octahedra, each of them isolated from the other by six WO_4 that share oxygens in the corners whereas each WO_4 tetrahedron keeps one corner oxygen unshared. Therefore, neglecting a slight interaction between unshared oxygen and adjacent W atom, WO_4 tetrahedra are also isolated from each other.

The Zr-O bond length is 2.07Å which corresponds to the ionic radii of O^{-2} plus Zr^{+4}, 1.35Å and 0.72 Å respectively [37]. In tetrahedra, bond length of unshared oxygen and tungsten is shorter than that of shared ones (1.705 versus 1.801 Å and 1.731 versus 1.783 Å for W1 and W2 respectively). The bond lengths are also very close to the sum of corresponding ionic radii, O^{-2} and W^{+6}.

W1 and W2 are aligned on threefold axis of unit cell. The incomplete representation of unit cell in Figure 2.4(c) helps to see this alignment. The distance between terminal oxygen of one tetrahedron and W of neighbor tetrahedron is 2.4Å. As the bond length between W and O in WO_3 with octahedral structure varies from 1.73 to 2.18Å [38], no normal bond can be considered for terminal oxygen and W of two adjacent tetrahedra. Moreover, as the distance between W1-O3 and O3-W2 are different (2.4 and 1.7 Å respectively); inversion center, which is available in ZrV_2O_7, can not be imagined for zirconium tungstate.

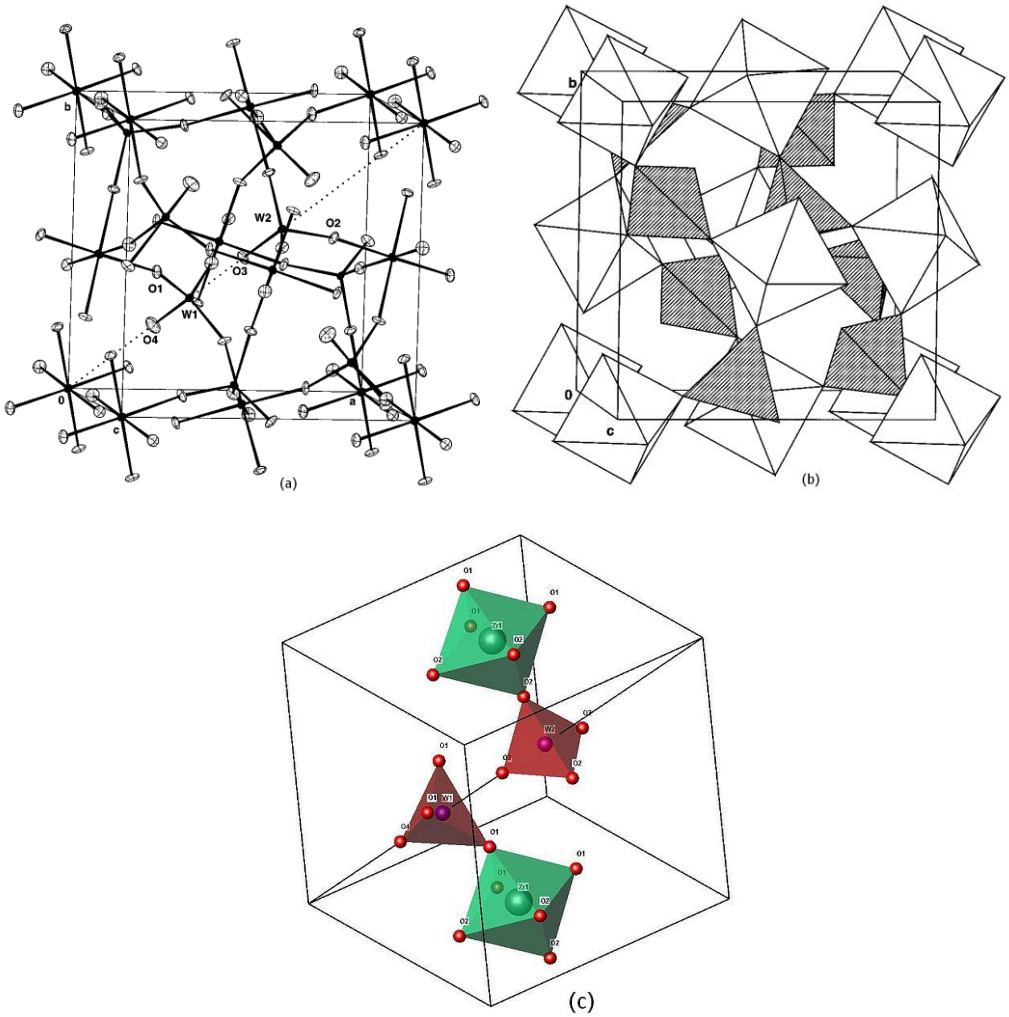

Figure 2.4 Thermal ellipsoidal (a) and polyhedral (b) representation of zirconium tungstate unit cell [1]. Incomplete unit cell of zirconium tungstate (c) represents alignment of W1 and W2 atoms on threefold axis [36].

2.4 NTE of Zirconium Tungstate - High Temperature Structure

Dilatometer is a device that is capable of measuring the change in dimension of bar shaped specimen at varied temperatures. Figure 2.5(a) shows the result of dilatometric analysis performed on a zirconium tungstate bar in a temperature range from 297K to 597K [39]. The graph shows a linear decrease from 297K to 398K. The coefficient of thermal expansion, α, in the temperature range was calculated as $-9.6\times10^{-6}K^{-1}$. The instability in dimension change from 398K to 473K implies a phase transition in this temperature range. From 473K afterwards dimension change regains a linear behavior with lower slope. α was calculated as $-4.7\times10^{-6}K^{-1}$ for this temperature range. X-ray and neutron diffraction analyses performed confirmed the phase transition observed in dilatometry experiments.

Figure 2.5(b) illustrates the XRD patterns of zirconium tungstate at temperatures below, within and above transition range introduced in Figure 2.5(a). XRD patterns have common

features but the peaks representing the planes with odd h values (e.g. (310)) were weakened at 419K and disappeared at 509K. This fact proves a phase transition from noncentrosymmetric to centrosymmetric cubic structure with increase in temperature. Therefore, $Pa\bar{3}$ has been attributed as space group to this high temperature structure [2].

Lattice parameters at different temperatures from 0.3 to 693K calculated from both neutron and X-ray diffraction analyses are tabulated in Table 2.4. Considering the lattice parameter of at arbitrary temperature, e.g. 293K, as reference, relative expansion of zirconium tungstate as a function of temperature was calculated. The calculated figures revealed an acceptable agreement between the data extracted from diffractions and dilatomety analyses. Assuming a linear contraction from 0.3 to 693K, coefficient of thermal expansion, α, was calculated as $-8.7\times10^{-6}K^{-1}$ [1]. High temperature structure of zirconium tungstate can be maintained up to 1050K above which metastable zirconium tungstate dissociates to constituent oxides [2].

Refinement of diffraction data by applying a model with disordered sites rather than single sites for W and O atoms located on threefold axis emerged the best fit with observed data. This fact has been used to justify the centrosymmetric arrangement of the atoms on threefold axis.

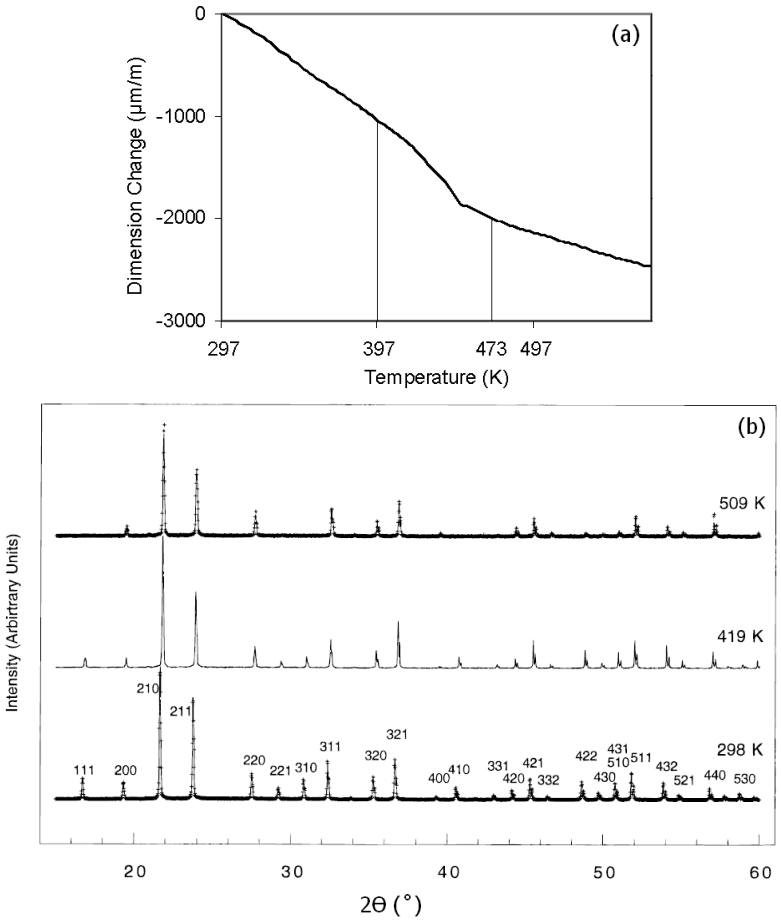

Figure 2.5 (a) Result of dilatometric analysis performed on synthesized zirconium tungstate bar from 297K to 593K [39] (b) XRD patterns of zirconium tungstate at 298K, 419K and 509K [1].

Table 2.4 Lattice parameter of zirconium tungstate as a function of temperature calculated from neutron and X-ray diffraction analyses as well as attributed space group. Neither $P2_13$ nor $Pa\bar{3}$ could be attributed to the data belonging to 423K [1].

Temperature (K)	Cell Parameter (Å)	Space Group
0.3	9.1823	$P2_13$
3.3	9.1810	$P2_13$
12	9.1810	$P2_13$
20	9.1797	$P2_13$
80	9.1758	$P2_13$
150	9.1686	$P2_13$
220	9.1631	$P2_13$
293	9.1568	$P2_13$
333	9.1530	$P2_13$
373	9.1500	$P2_13$
423	9.1416	
483	9.1371	$Pa\bar{3}$
583	9.1318	$Pa\bar{3}$
693	9.1269	$Pa\bar{3}$

In low temperature structure the unshared corners of the two tetrahedra located on threefold axis are aligned on [111] direction but at high temperatures the unshared vertices of tetrahedra change their orientation from [111] to $[\bar{1}\bar{1}\bar{1}]$ direction randomly [40]. In other words, if the two tetrahedra on threefold axis of room temperature structure are inverted around (½,½,½) and the direct and resultant inverted arrangement are superposed upon each other, arrangement of tetrahedra at high temperature after order-disorder phase transition will appear (Figure 2.6). Such a phase transition necessitates highly mobility of O4 atom and short distance displacement of O3 atom. In this case the coordination number of unshared O atoms, that is one for room temperature structure with fixed unshared oxygens, has increased to 1+1 for at least one of unshared oxygens namely O3. Increase in coordination number of unshared oxygens implies a decrease in flexibility of framework structure and, thus, decrease in negative thermal expansivity [41].

2.5 NTE of Zirconium Tungstate - High Pressure Structure

Aiming to find out the structural behavior of zirconium tungstate while subjecting it to high pressures, Evans et al. collected neutron diffraction data as a function pressure [41]. The analysis revealed that a phase transition from cubic to orthorhombic with space group of $P2_12_12_1$ starts at 2kbar and is completed at 6kbar (R#1 in Figure 2.9). The orthorhombic structure retained when the pressure released to room pressure but subjecting it to a temperature of 393K transformed back the structure to cubic. Thus, orthorhombic structure under ambient conditions is metastable.

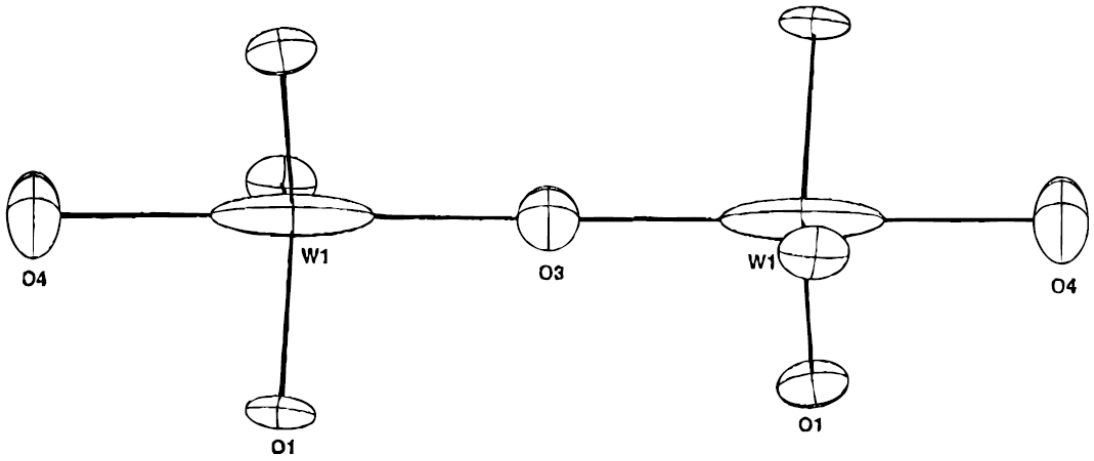

Figure 2.6 Thermal ellipsoidal representation of WO_4 groups at high temperature after order-disorder phase transition [1].

The lattice parameters of orthorhombic form of zirconium tungstate (hereafter γ-ZrW_2O_8) at room temperature were calculated as 9.067, 27.035 and 8.921Å for a, b and c, respectively. A rough comparison between lattice parameters of α and γ phase declares that a of α-ZrW_2O_8 is approximately equal to a and c and one third of b parameters of γ-ZrW_2O_8. The calculation of unit cell volume shows a 4.98% volume decrease as a result of phase transition. From the diffraction analysis the atomic position of Zr, W and O in the unit cell were also calculated. The results are tabulated in Table 2.5. Polyhedral representation of γ-ZrW_2O_8 arises by linking oxygens atoms in the unit cell by imaginary lines which has been illustrated in Figure 2.7 (a).

Alike to cubic phase, polyhedral units of orthorhombic phase consist of ZrO_6 octahedra and WO_4 tetrahedra. Three crystallographically distinct pairs of WO_4 tetrahedra can be distinguished in the unit cell which were depicted in Figure 2.7 (c), (d) and (e). In comparison with α-ZrW_2O_8 structure (Figure 2.7(b)) W-W interatomic distances of all three WO_4 pairs have significantly been decreased in orthorhombic structure and it could be the source of 5% decrease in unit cell volume. Moreover, unlike α-ZrW_2O_8 in which W-O-W bond are aligned on threefold axis, W-O-W bonds angle deviates from 180°. It is worthy of note that in γ-ZrW_2O_8 orientation of W3-W4 tetrahedra pair is reversed in comparison with that of other two tetrahedra pairs as a result of unshared oxygen (O103) migration from W3 to W4 and consequent migration of unshared O (O104) from W4 to W3 tetrahedra (Figure 2.7(d)). The orientation reversal of one third of W-W pairs has been claimed as the way cubic phase accommodates hydrostatic pressure and, thus, forms orthorhombic phase [42].

To find out the coefficient of thermal expansion, unit cell parameters of γ-ZrW_2O_8 and, thus, unit cell volume were calculated from neutron diffraction data as a function of temperature [41-43]. The results have been represented in Figure 2.8. From the figure it can be deduced that both unit cell parameters and unit cell volume decrease with a nearly linear behavior below room temperature. The linear coefficient of thermal expansion for a, b and c directions in the interval of 4 to 150K were calculated as -2.09, -1.95 and $-1.82\times10^{-6}K^{-1}$, respectively. The volume coefficient of thermal expansion was calculated as $-5.85\times10^{-6}K^{-1}$ for the same temperature interval [43]. The linear coefficients of thermal expansion in all three directions are about an order of magnitude less than the coefficient of cubic phase.

Table 2.5 Fractional atom sites in γ-ZrW_2O_8 unit cell at room temperature [41].

Atom	x/a	y/b	z/c
Zr1	0.2161	0.4206	0.8080
Zr2	0.7225	0.4239	0.2344
Zr3	0.7438	0.2538	0.7394
W1	0.9021	0.3738	0.5809
W2	0.6276	0.4462	0.8250
W3	0.1395	0.2153	0.8564
W4	0.3786	0.3150	0.6096
W5	0.4053	0.4508	0.4585
W6	0.1279	0.3786	0.2094
O11	0.7104	0.5940	0.9561
O12	0.6541	0.6890	0.1477
O13	0.4974	0.5916	0.2286
O101	0.4599	0.6396	0.9564
O21	0.6929	0.4381	0.0130
O22	0.4395	0.4371	0.8510
O23	0.7050	0.5055	0.7775
O102	0.7883	0.6046	0.2382
O31	0.6705	0.3475	0.1934
O32	0.6910	0.2793	0.9442
O33	0.4544	0.2657	0.1755
O103	0.4455	0.3672	0.5074
O41	0.2302	0.6514	0.2426
O42	0.9593	0.7183	0.1656
O43	0.2230	0.7179	0.9639
O104	0.7693	0.2488	0.2521
O51	0.3531	0.5136	0.3995
O52	0.9833	0.5669	0.7926
O53	0.2417	0.5563	0.1024
O105	0.9480	0.5327	0.0945
O61	0.1865	0.3909	1.0169
O62	0.1602	0.3130	0.2038
O63	0.9360	0.4023	0.1825
O106	0.2625	0.5824	0.8151

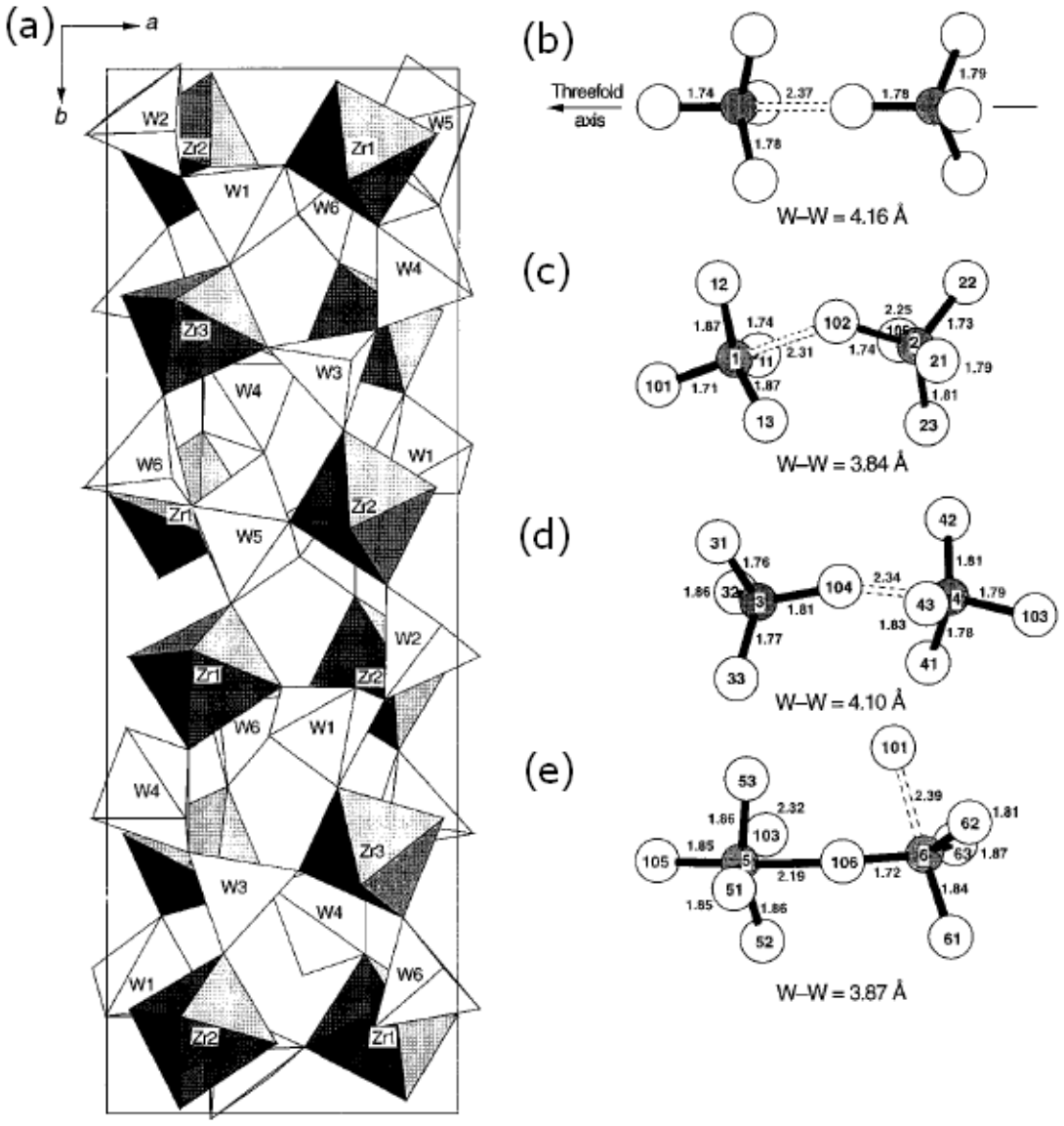

Figure 2.7 (a) Polyhedral representation of γ-ZrW_2O_8 unit cell. (b) Ball-bar representation of WO_4 pairs in cubic ZrW_2O_8 along with threefold axis. (c), (d) and (e) Ball-bar representation of distinct WO_4 pairs in γ-ZrW_2O_8. Shaded balls are W and white ones are O. The unit of interatomic distances is Å [41].

As the distance between terminated oxygen and adjacent W atom in γ-ZrW_2O_8 has decreased in comparison with cubic phases and, moreover, all three pairs of W-O-W bonds are bended, the effective coordination numbers of all terminal oxygens in orthorhombic topology are 1+1 (Figure 2.7). The function of increase in coordination number is as having cross-bracing agent of adjacent polyhedra in the framework that decrease the flexibility of the framework significantly in comparison with α-ZrW_2O_8 (that all terminal oxygens have coordination number of 1) and even centrosymmetric (β) ZrW_2O_8 (that half of terminal oxygens have coordination number of 1+1). Above 150K, the volume thermal expansion

gets less negative and reaches zero value at 225K. Above room temperature the linear coefficient of thermal expansion is highly anisotropic. The coefficient was calculated as +11.5, +4.5 and $-10.5\times10^{-6}K^{-1}$ for a, b and c directions, respectively [44]. The overall effect of expansion in a and b direction and contraction in c direction is a slight volume increase with increase in temperature above room temperature. Transforming back to cubic phase at 393K, thermal expansion coefficient zirconium tungstate regains negative values accompanied with 5% volume increase.

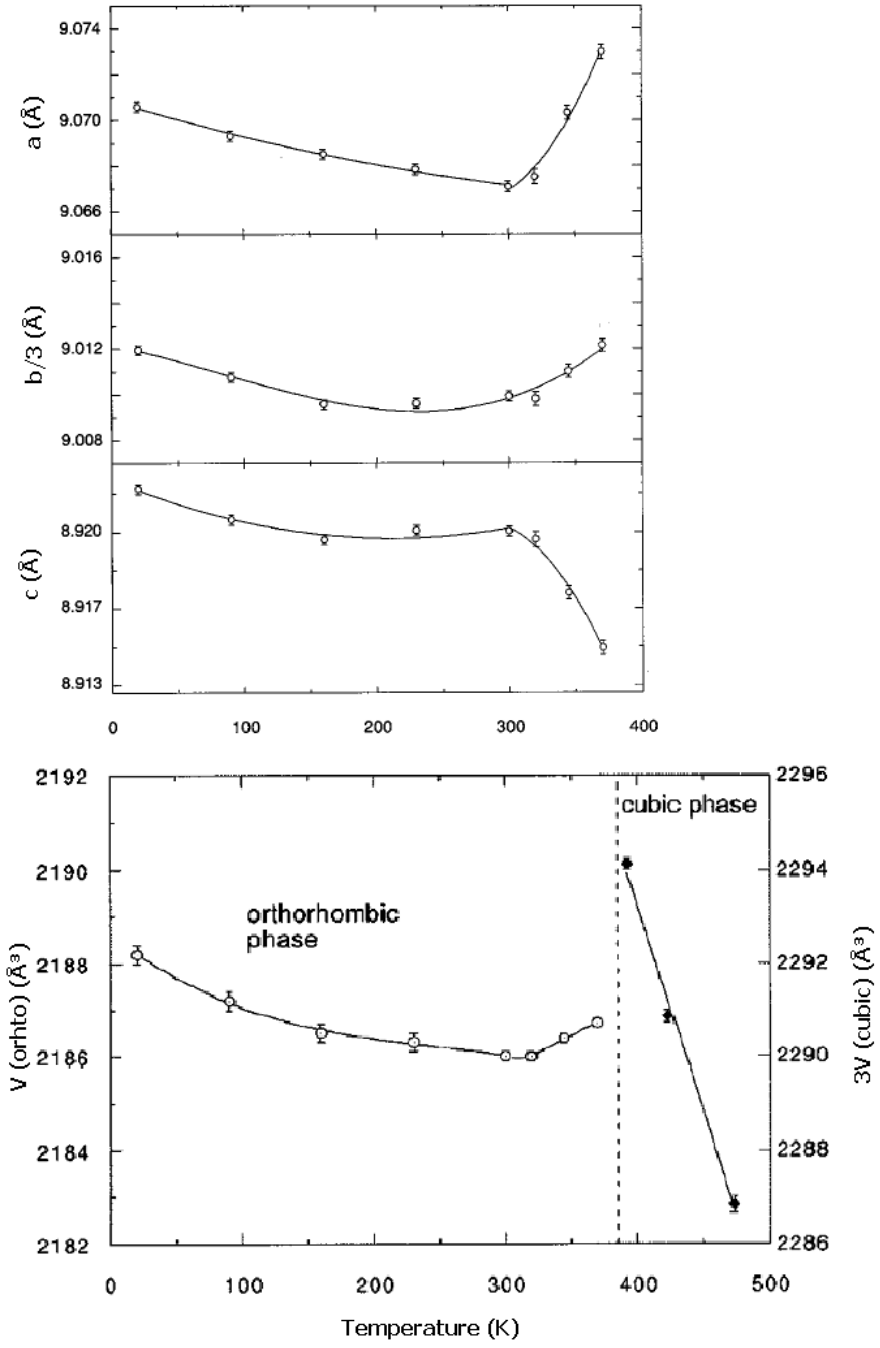

Figure 2.8 Unit cell parameters and unit cell volume of γ-ZrW_2O_8 as a function of temperature [43].

Structural behavior of γ-ZrW_2O_8 upon further increase in pressure at ambient temperature has also been investigated [45-47]. The γ structure accommodated induced pressure by further decrease in unit cell volume. The minimum volume was achieved at 10kbar where the unit cell volume reached to 2182Å^3. XRD analysis showed no decomposition to constituent oxides as a result of induced pressure. From 13kbar onwards, widening of XRD peaks and increasing of unit cell volume indicated the starting of an amorphization process. At 40kbar even the main feature of γ-ZrW_2O_8 peaks were faded away implying the completion of amorphization process. No phase transformation was observed upon further pressure increase. The amorphous ZrW_2O_8 was retained upon releasing the pressure to ambient. Heat treatment of the amorphous specimen at 1000K for 30 minutes caused the crystallization back to cubic phase (R#1 Figure 2.9).

2.6 High Pressure-High Temperature Structure

Structural behavior of zirconium tungstate at elevated temperature and pressure depends on the adopted path [46, 48]. Heat treatment of a sample up to 1142K which had already been pressed and, thus, amorphized at 51kbar under ambient temperature, led to decomposition to crystallized constituent oxides (R#2 in Figure 2.9) [48]. On the other hand, heat treatment of the sample up to 1042K which had been pressed to 25kbar, resulted in formation of a distinct trigonal (or hexagonal) phase. This new phase was retained at ambient condition after quenching [48]. In another route, a sample with cubic structure was pressed at a constant temperature of 740K [48].

The sample started amorphization at 10kbar. The temperature was increased after the sample had been pressed up to 12kbar. In this case the trigonal phase started to appear at approximately 800K and the formation completed at 850K. Sample with trigonal structure could be retained at ambient condition after quenching [48]. The two routes resulting in trigonal structure have also been illustrated in Figure 2.9 (R#3 and 4). The structural investigation revealed that the new polymorph has α-U_3O_8 type trigonal system and $P\bar{6}2m$ as space group. The lattice parameters were calculated as 6.4145Å and 3.7941Å for a and c, respectively. The unit cell volume was also calculated as 135.20Å^3 which is approximately half of that of cubic and two thirds of orthorhombic structures.

It is worthy of attention that trigonal structure have also been reported to be observed in the production of ZrW_2O_8 in case a nonhydrolytic sol-gel method is used [9, 49]. Hence, unlike orthorhombic phase which can only be achieved with the application of pressure, trigonal structure cannot be considered only specific to high pressures.

2.7 Production Methods: Solid State Reaction

Zirconium tungstate was synthesized first by Graham and coworkers [3]. Attempting to stabilize ZrO_2 crystal structure they added cations with valences of more than two. The new phase was produced when they tried W^{6+} as stabilizer. Mechanically mixing ZrO_2 and WO_3 with a variety of compositions, they heat treated the mixture in the temperature range from 1000 to 1400°C to build up a partial phase diagram. Annealing of a mixture that consists of 60mol% of WO_3 at 1200°C for 15 minutes was claimed to produce the highest yield of new phase. Observation of the decomposition of zirconium tungstate to constituent oxides during slow cool down proved metastability of the new phase at ambient condition and 1150°C was determined as minimum limit of stability from which, at least, the annealed mixture should be quenched.

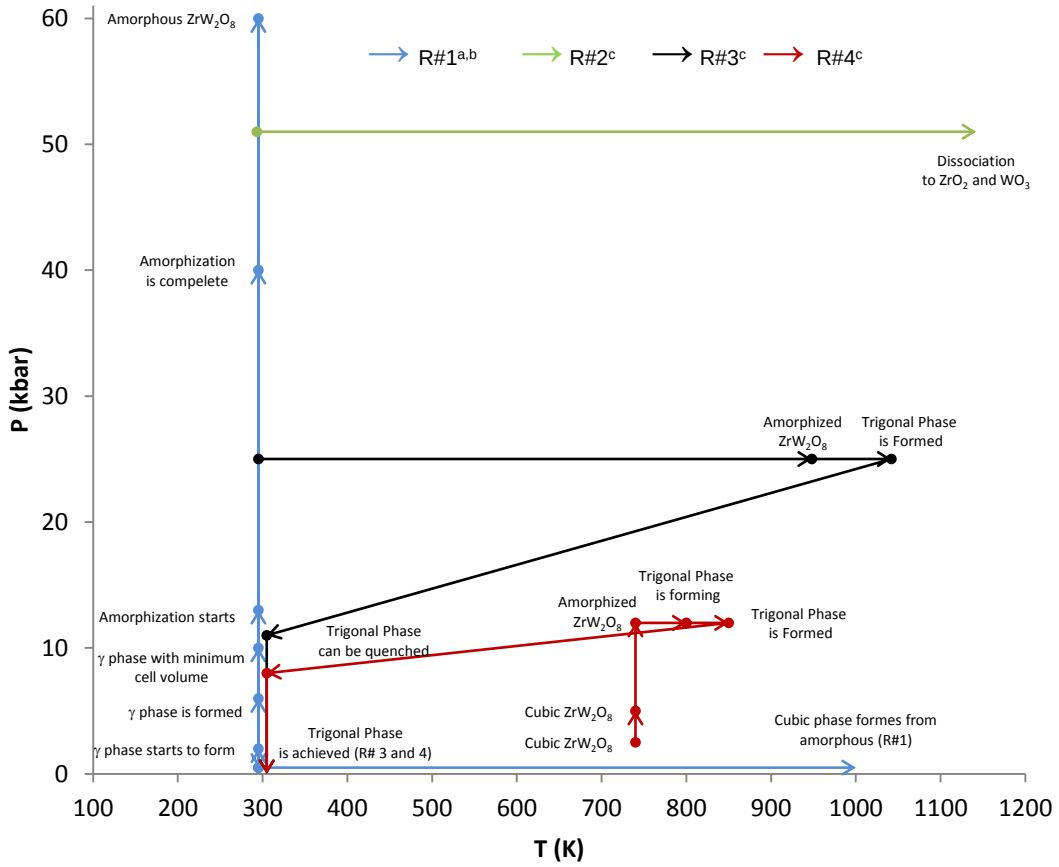

[a] [41].
[b] [46].
[c] [48].

Figure 2.9 Structural response of zirconium tungstate to different processing routes involving changes in pressure and temperature.

Such a practice was typical of a solid state reaction to produce a metastable substance. The advantages of solid state reaction can be summarized as:

- Economic because of absence of solvent
- Easy separation because of absence of solvent
- Environmentally friendly because of absence of solvent effluent

However, solid state reaction has inherent drawbacks. Although rigorous mechanical mixing can usually be applied, approaching to a uniform reactant mixture is very difficult. Regarding the severe effect of deviation of reactants' composition from stoichiometric ratio on purity of zirconium tungstate (Figure 1.1), inhomogeneity of reactants mixture could result in impure product. Wet ball milling was claimed to be effective in approaching to more homogeneous mixture [50]. Moreover, the reaction takes place at the surface layer of contacting reactants particles and as solid reactants are typically micron sized, diffusion of one reactant into the core of the other one necessitates long reaction times. Intermittent regrinding-reheating has been advised to mitigate this problem but the measure has not been effective as a result of long diffusion distance [7]. Special case of zirconium tungstate synthesis encounters additional problem of volatility of WO_3 at high temperatures. Therefore, long dwell time at

high temperature in the oven results in vaporization of a portion of WO_3 and disturbance of stoichiometry and, hence, impure product. Covering the reactant mixtures by a layer of excess WO_3 [51] or by a platinum plate [52] were used as counter-measures. Solid state reaction in which sintering step was performed by CO_2 laser could effectively decrease the reaction time but compressive stress originated from rapid solidifying of product melt caused formation of orthorhombic phase [53]. Main features of important studies in which solid state reaction has been adopted to synthesize zirconium tungstate are summarized in Table 2.6.

Table 2.6 Important studies in which solid state reaction has been adopted to produce zirconium tungstate.

Author	Starting Materials	Annealing temperature and duration	Product phase	Remark(s)
Martinek et al. (1968) [54]	ZrO_2 - luminescent grade – TA	600°C overnight & 1150°C for 4hr	Cubic	CTE was calculated
Martinek et al. (1970) [55]	zirconium carbonate ($2ZrO_2 \cdot CO_2 \cdot XH_2O$)-TA	300, 450 and 600°C & 1200°C for 48h	Cubic	
Kowach (1999) [51]	ZrO_2–WO_3	1300°C (at a rate of 700°C /hr) for 2hr & cooling at a rate of 0.5°C/h to 1230°C	Cubic	•The reactants were covered with WO_3 layer •Single crystals were obtained
Kameswari et al. (2000) [7]	• ZrO_2–WO_3 • $ZrO(NO_3)_2 \cdot 2H_2O$–$(NH_4)_{10}W_{12}O_{41} \cdot 5H2O$	•1200°C for 18hr •1200°C for 6hr	Cubic	•Impure product •Synthesis from salts rather than oxides.
Chen et al. (2003) [52]	ZrO_2–WO_3	1155, 1170, 1185, and 1200°C for 6hr	Cubic	The WO_3–ZrO_2 mixture was placed between two Pt plates to avoid the volatilization of WO_3 during the sintering process.
Nishiyama et al. (2005) [56]	ZrO_2–WO_3	1200°C for 2hr & quenched & again 1200°C for 2hr	Cubic	Effects of quenching rate on purity were investigated.
Liang et al. (2007) [53]	ZrO_2–WO_3	By CO_2 laser	•γ phase •Cubic	•γ phase dominates when the scan speed is>2mms^{-1}. •With lower scan speed, the α phase is produced.
Mancheva et al. (2007) [57]	ZrO_2–WO_3	• 1300°C for 20min • 600°C for 15hr (for γ → β phase transition)	•γ phase •Cubic	•Melt quenching technique •The melt was quenched at high cooling rates (10^4 to 10^5 K/s) using a roller quenching technique.
Tani et al. (2008) [50]	ZrO_2–WO_3	1200°C for 5min to 8hr	Cubic	•The last 3 synthesis methods were partially wet chemical (precipitation). •Avrami's equation constants were obtained.
	•$ZrO(NO_3)_2 \cdot 2H_2O$–WO_3 •$ZrCl_2O \cdot 8H_2O$–WO_3 •ZrO_2–$(NH_4)_{10}W_{12}O_{41} \cdot 5H2O$	600°C for 3hr & 1200°C for 5min to 8hr		

2.8 Production Methods: Wet Chemical Methods

If, instead of firing the mechanically mixed tungsten and zirconium oxides, chemically mixed oxides are prepared to be annealed a significant decrease in reaction time and increase in product purity can be anticipated. By dissolution of compound in a solvent, the intermolecular as well as ionic bods in the compound can be broken. Hence, mixing of two solutions of the components of a desired compound permits the preparation of a mixture that is homogeneous at atomic scale. For the special case of preparation of a wet mixture of tungsten and zirconium oxides the following steps can be generalized from the procedures followed in the literature:

- As WO_3 and ZrO_2 are not easily dissolved in any solvent, two respective tungsten and zirconium sources which can be dissolved in regular solvents are adopted. Sources can be any organometallic or inorganic compound.
- Each W and Zr source is dissolved in an appropriate solvent.
- The two solutions are mixed to achieve a precursor of W and Zr sources in which Zr and W species are mixed at atomic level.
- The mixed state is captured in a way that the state is preserved while drying and any phase separation and inhomogeneity is prevented.
- The mixture is dried to remove solvent and calcined to achieve mixed tungsten and zirconium oxides in molecular level from dried precursor.
- The oxides mixture is fired and quenched based on the phase diagram (Figure 1.1) to reach to zirconium tungstate product.

To preserve the mixed state of W and Zr sources while drying, two approaches are usually applied. In the first approach the mixed state is captured by evolution of a gel network through a colloidal reaction. This approach has been termed as sol-gel process. If the solvent used is water the process is classified as hydrolytic; otherwise, it is called non-hydrolytic sol-gel process. As second approach an agent is added to the mixture to precipitate the precursor. This approach has been termed as co-precipitation.

An alternative approach can also be applied in which drying, calcinations and sintering steps has been combined by adding a fuel to the mixture of solutions of W and Zr sources. If the fuel included mixture is heated in a furnace the temperature of the mixture can rise to the extent which is well enough to perform all heat treatment steps instantaneously. For a fuel like magnesium respective oxide ash remains after burning, and a step of leaching is necessary to separate product from ash. This method has been termed as self-propagating high-temperature synthesis, SHS.

Like in solid state method, in the described wet chemical methods above the mixture is prepared and generally fired at the compound's thermodynamic stability range (1100 to about 1200°C) and quenched below where it is kinetically stable (i.e. 777°C) or preferably room temperature. All these methods could also be named as "high temperature" approaches, in which heat treatment at high temperature of 1200°C is crucial. Because of exposure to the high temperature control on particle size growth in these methods is very difficult and the zirconium tungstate crystals grow over micron size. To be able to control particle size of the product setting up of bench chemistry which is capable of synthesis of zirconium tungstate at lower temperature is essential. These groups of methods could be termed as "low temperature" approaches. Production of amorphous [8, 58] and trigonal [6, 9, 49] zirconium tungstates by non-hydrolytic sol-gel approach at temperature range of 450 to 600°C was reported. Cubic phase could also be synthesized at 600°C by co-precipitation provided that the precipitate is aged for a long time, e.g. 2 weeks, in a concentrated solution of a strong acid, e.g. HCl [7, 11, 12]. As an alternative to decrease the aging time after precipitation, the precipitate mixtures were aged under autogenous high vapor pressure and

temperature medium. The medium is formed by vaporizing a liquid under pressure in an autoclave. Depending on the type of liquid, the process is named hydrothermal, glycothermal, alcothermal, etc. It was hypothesized that in low temperature co-precipitation approaches an intermediate phase, i.e. $ZrW_2O_7(OH)_2 \cdot 2(H_2O)$, was formed at around 180°C which could be dehydrated to orthorhombic polymorph and transformed to cubic zirconium tungstate during heat treatment at 600°C [13]. The crystallization of zirconium tungstate hydroxide hydrate was affected by halide and hydronium ion concentrations in the ageing solutions. The flowchart of proposed methods to synthesize zirconium tungstate is illustrated in Figure 2.10.

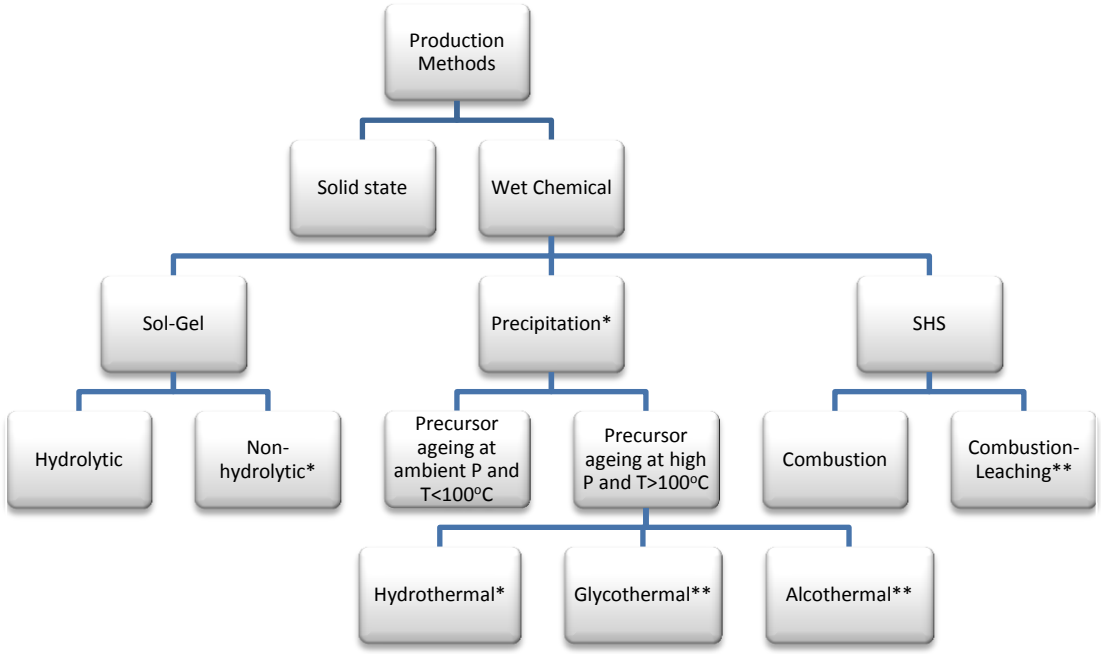

Figure 2.10 Classification of the methods suitable for synthesis of zirconium tungstate.
* Methods after which a low temperature heat treatment around 600°C is sufficient for crystallization of the synthesized and aged precursor.
** Methods which have not yet been tried to synthesize zirconium tungstate.

Details of wet chemical methods used for synthesis of zirconium tungstate will be described in the coming subsections.

2.8.1 Wet Chemical Methods: Combustion

Adoption of W and Zr source and fuel suitable for combustion process is the first step. As ammonium metatungstate ($(NH_4)_6H_2W_{12}O_{40} \cdot xH_2O$) and zirconium oxynitrate ($ZrO(NO_3)_2 \cdot nH_2O$) provides sufficient oxygen atoms in the formulas for combustion, they are suitable as W and Zr sources. Since no oxide ash is remained from organic fuels, e.g. urea, their application is advantageous. Next step is to calculate the stoichiometric ratios of the

combustion reaction based on total reducing and oxidizing coefficients of the reactants. In the next step, W and Zr sources are dissolved in 3M nitric acid and the fuel is added to the reactant solution.

To prevent any precipitation, combusting mixture should be quickly heat treated in furnace preheated at 500°C. Boiling of the mixture is accompanied by decomposition of the reactants and evolution of gases, e.g. CO_2, N_2, H_2O and nitrogen oxides, as well as rapid temperature rise to about 1200°C. The temperature comes back to 500°C within several minutes. Though majorly cubic zirconium tungstate, the product of the combustion process has minor impurities in the form of WO_3. Heat treatment of this product at 1200°C for 1 hour results in phase pure product. Table 2.7 summarizes the studies combustion method is used.

Table 2.7 Studies in which combustion method was adopted to produce zirconium tungstate.

Author	Starting Materials	Annealing temperature and duration	Product phase
Kameswari et al. (2000) [7]	$ZrO(NO_3)\cdot xH_2O$ - $(NH_4)_6H_2W_{12}O_{40}\cdot xH_2O$ – urea – HNO_3(3M)	•500 →1050°C for 2-3min (by combustion) •1200°C for ?hr	•Cubic (impure) •Cubic (pure)
Yang et al. (2007) [10]	$ZrCl_2O\cdot nH_2O$ - $(NH_4)_5H_5[H_2(WO_4)_6]\cdot nH_2O$ - H_3BO_3+Urea - HNO_3(3M)	•500 →????°C for ?min (by combustion) •1200°C for 1hr	•Cubic (impure) •Cubic (pure)
Yan et al. (2007) [59]	$ZrCl_2O\cdot nH_2O$ - $(NH_4)_5H_5[H_2(WO_4)_6]\cdot nH_2O$ - H_3BO_3+Urea - HNO_3(3M)	•500 →????°C for ?min (by combustion) •1200°C for 1hr	•Cubic (impure) •Cubic (pure)

2.8.2 Wet Chemical Methods: Co-precipitation

Both high and low temperature heat treatments were applied to the precursors obtained by co-precipitation methods in synthesis of zirconium tungstate. High temperature heat treatment was applied to precursor obtained from a solution prepared by pouring zirconium oxynitrate and ammonium metatungstate solutions at the stoichiometric ratio into a container in which water had been preheated at 60°C [7]. The amorphous precipitate formed was filtered and calcined at 800°C for 10 hours and finally annealed at 1200°C to reach the phase pure product.

Regarding the heat treatment at high temperature a product with controlled particle size cannot be anticipated. In studies, which embodied a low temperature heat treatment to the co-precipitated precursor, researchers followed fairly similar procedures [11, 12, 60]. Ammonium metatungstate and zirconium oxychloride were adopted as W and Zr sources, respectively. Their solutions in water were prepared so that the molar concentration of W source was twice as Zr source. The same volumes of the solutions were dripped in the third container in which preheated water was being stirred. Volume of water in the third container was half the volume of aimed Zr or W solution volume. The formed precipitate was stirred for 10 hours. Aiming to reach to the molarity of 3mol/lit of acid, 6M HCl was added to the mixture. After refluxing the mixture for 48 hours, the mixture was cooled down and filtered

to separate the precipitate. The filtrate was washed and aged for 7 more days. Calcination of the aged precipitate at 600°C for 10 hours resulted in phase pure product. The reaction occurred while refluxing the precipitate in acidic medium and aging was predicted to be a co-condensation between W and Zr sources which resulted in $ZrW_2O_7(OH)_2 \cdot 2H_2O$ phase [16]:

$$WO_4^{-2} + 2H^+ + (y-1)H_2O \rightarrow WO_3 \cdot yH_2O \quad (3)$$
$$ZrO^{+2} + (x+1)\,H_2O \rightarrow ZrO_2 \cdot xH_2O + 2H^+ \quad (4)$$
$$ZrO_2 \cdot xH_2O + WO_3 \cdot yH_2O \rightarrow ZrW_2O_7(OH)_2 \cdot 2H_2O + (x+2y-3)H_2O \quad (5)$$

Calcination dehydrated and transformed the hydrated phase to ZrW_2O_8 [60]. The particle size of the product was in submicron range. Both heterogeneous [60] and rod like [12] shaped particles have been reported. The advantage of this method is considerable decrease in heat treatment temperature and duration. But the method suffers from long precursor preparation time, i.e. nearly 10 days, and high cost of starting materials. Unless ageing under hydrothermal conditions were adapted, any attempt to decrease the reflux time, ageing time or acid exclusion resulted in impure product. A H_2O_2 assisted co-precipitation method has been developed in our group in which fairly economical W source, TA, was replaced by ammonium metatungstate and long ageing time was shortened without resorting to hydrothermal ageing. In this case, the preparation time could be decreased to 3 days [61]. The flowchart of synthesis method is depicted in Figure 2.11.

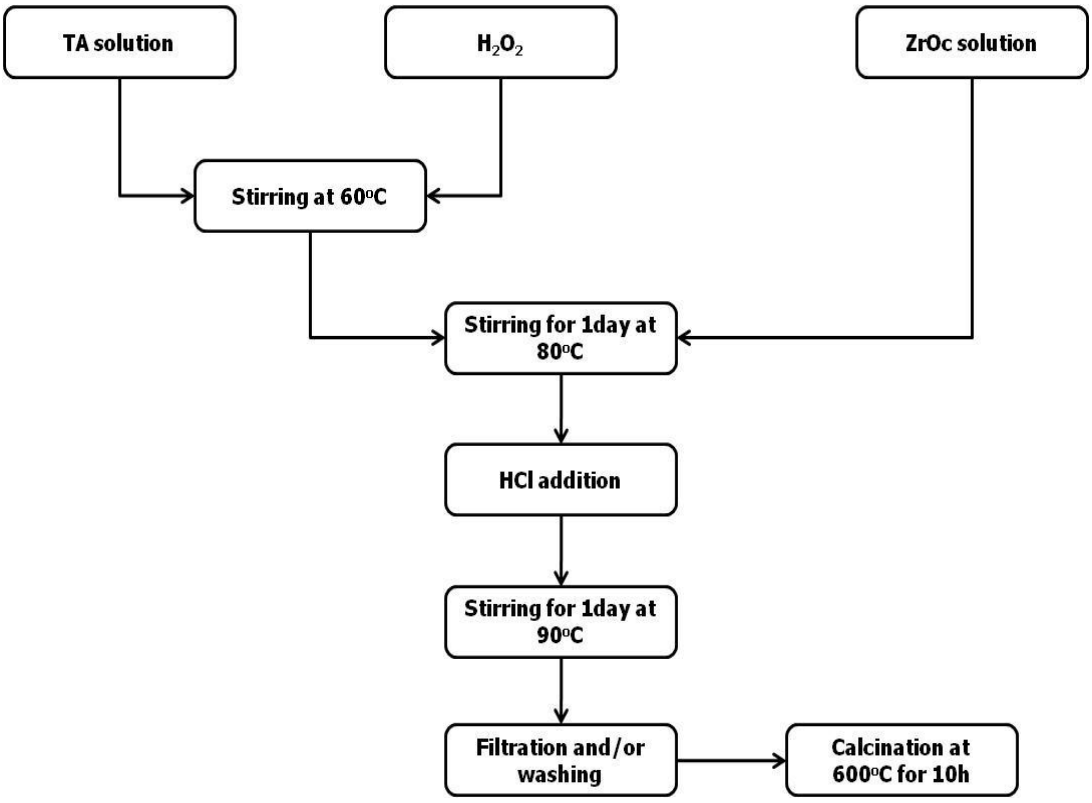

Figure 2.11 Flowchart of H_2O_2 assisted co-precipitation method to synthesize zirconium tungstate from TA and zirconium oxychloride with low temperature heat treatment [61].

2.8.3 Wet Chemical Methods: Hydrothermal

Hydrothermal synthesis involves a heterogeneous reaction within water as solvent and occur at temperatures higher than normal boiling point of water; hence, at higher pressures to create vapor-liquid equilibrium. Though the control of temperature is preferable, since the degree of freedom in this case is one, the synthesis condition can be controlled by control of either temperature or pressure. Reactants mixture in water is fed to an autoclave which contains water and the lid of the apparatus is closed. The water in the autoclave starts to boil as a result of thermal energy and, therefore, the pressure of the vessel rises. The pressure will stop rising at the saturated vapor pressure of the set point temperature. The condition of the reactant mixture will obviously follow the condition of the vessel. Reaction in that high temperature and pressure is a matter of dissolution of reactants in the solvent and crystallization in the form of new phase which is restricted or impossible at ambient condition by refluxing. Such a condition is very suitable to grow single crystals. Growth of single crystals of zirconium tungstate by hydrothermal method has been studied [16].

Hydrothermally aging a precursor that consists of zirconium oxychloride and sodium tungstate in 3.4M HCl solution at different temperatures, Colin et al. found out that the co-condensation reaction time decreased exponentially from 1 week to several hours with an increase in temperature from 110 to 200°C [13]. Nevertheless the product of refluxing process in this condition, even after several days, was amorphous. Therefore, hydrothermal aging was found capable of decreasing the reaction time by accelerating the zirconium hydroxide hydrate formation. Among the research in which hydrothermal aging has been applied to synthesize zirconium tungstate [7, 15-17], Kozy et al. [14] did an extensive effort to clarify the role of reaction time, temperature, acid type and concentration on product morphology and size. The smallest particle size was achieved in intermediate concentrations and reaction temperature; hence, they claimed that both nucleation and growth are influential on the particle size of the product. They also showed incorporating alcohols into reaction slurry effectively decreased particles' agglomeration. Needle-like shape was dominant morphology of the products synthesized by strong acids assisted co-precipitation (either refluxed or hydrothermally aged). This fact suggests a preferential interaction of acid ions with certain surfaces the crystal, structure of which is tetragonal for zirconium tungstate hydroxide hydrate.

2.8.4 Wet Chemical Methods: Sol-Gel

The sol-gel process involves two steps. Firstly, an inorganic network of colloidal suspension (sol) is evolved from a chemical solution. Secondly, the sol is gelated to form a network in a continuous liquid phase (gel). Metal alkoxides and chlorides are usually used as starting material to dissolve in a solvent and form a precursor. The process is named hydrolytic sol-gel if the solvent is water. If other solvents are alternatively used, the process is termed as non-hydrolytic sol-gel. Hydrolysis and polycodensation are proposed as mechanisms for formation of sol from the precursor of starting material and gelation. The summary of the researches in which sol-gel has been adopted as production method are tabulated in Table 2.8. Both hydrolytic and non-hydrolytic versions of sol-gel process have been tried to produce zirconium tungstate. Studies in which hydrolytic version was adopted high temperature heat treatment approach was needed for crystallization [5, 62-64]. Nevertheless, Georgi [6] succeeded in synthesizing a crystalline zirconium tungstate by citric acid assisted hydrolytic sol-gel method by using a low temperature heat treatment to the precursor as an exception. However, the product had trigonal arrangement which was transformed to cubic phase by short time heat treatment at 1125°C. Kanamori [8] could also produce crystalline zirconium tungstate after heat treatment at low temperatures. Here water was adopted as one of the three solvents to dissolve the zirconium source. As water

was a minor solvent in synthesis of the product, the method can also be classified within non-hydrolytic sol-gel category. Moreover, the product was amorphous with particle size of 50 to 300nm. Regarding the submicron ranged size of the product, Kanamori [58] applied spark plasma sintering to achieve well- crystallized product with relative density of 98.6% at a temperature less than 600°C. Researchers who adopted non-hydrolytic sol-gel method to produce zirconium tungstate usually followed the precursor preparation step with low temperature heat treatment step to achieve the crystalline products [9, 49]. However, like the products of hydrolytic sol-gel precursors treated at low temperature [6], their products had trigonal arrangement which transformed to cubic phase upon heat treatment at high temperatures. Lind, coworker of Wilkinson, added cubic zirconium tungstate powder to the precursor prepared by Wikinson's method [9] and succeeded in production of cubic phase by non-hydrolytic sol-gel method with a low temperature heat treatment [65].

The common characters of sol-gel studies that were mentioned in Table 2.8 are high cost starting materials and long processing times, e.g. 72 hours aging time. To overcome the mentioned drawbacks, an ammonia assisted hydrolytic sol-gel method was used in our group in which fairly abundant starting materials, namely tungstic acid and zirconium acetate were used [66]. An investigation on the effect of aging time and pH of the precursor on the purity of the product was performed. It was shown that the purity was mostly affected by pH rather than aging time. Therefore, the aging time was fixed on 2 hours. Method was a typical hydrolytic sol-gel production method followed by a high temperature heat treatment, but with shorter processing times and starting materials with lower cost. Nevertheless, the purity of the product did not exceed 64vol.%. The first aim of this study was close investigation of precursor preparation as well as heat treatment procedures of prior work in our group to obtain a phase pure product.

It is noteworthy that both coprecipitation and sol-gel methods can be combined with microemulsion strategy to achieve zirconium tungstate nanoparticles. Sullivan [60] combined the sol-gel method inspired from Kameswari's method [7] with reverse microemulsion method and produced nanoparticulate ceramic which consists of predominantly parallelepiped particles with dimension of 200nm×200nm×100nm. Vural [67] could also combine the novel coprecipitation method developed in our group [61] with microemulsion technique and synthesized a product which consists of zirconium tungstate nanoparticles.

2.9 Zirconia as Composite Counterpart with Zirconium Tungstate

As descried before, unless it is put together with another component into a composite to control CTE, no significant application can be envisioned for zirconium tungstate alone. So far, several counterparts from all groups of materials have been examined to make composite with zirconium tungstate. From metals, copper [68-70] and aluminum [71] have been tried. Among polymers, polyimide [60] and phenolic resin [72] have been put into composite with zirconium tungstate. Kanamori [73] tried to make ceramic-ceramic composite of SiO_2 and zirconium tungstate by spark plasma sintering. Among the composites produced between ZrW_2O_8 and other ceramics, ones with ZrO_2 have been investigated closely compared to any other system, due to the wide application areas of ZrO_2 alone and the absence of intermediate phases between ZrW_2O_8 and ZrO_2 as proposed by the WO_3-ZrO_2 phase diagram [51]. However, as the evaporation tendency of WO_3 at temperatures higher than 1200°C increases, a higher limit to the sintering temperature and time spent at that temperature is imposed. This higher temperature limit will be accompanied by weak sinterability between the composite components due to the big gap between decomposition temperature of ZrW_2O_8 and melting point of ZrO_2 which is a challenge for composite synthesis that should be countermeasured.

Table 2.8 Studies in which sol-gel method has been adopted to produce zirconium tungstate. Hydrolytic sol-gel methods can be distinguished by existence of water in "Starting Materials" column.

Author	Starting Materials	Aging & Heat Treatment	Product Phase	Remark(s)
Sleight et al. (1996) [63]	zirconium oxyhalides or zirconium oxynitrates or $ZrCl_4$ – TA or WCl_6 - Water or ammonia or H_2O_2 or ethanol	•800°C for 15hr & 1200°C for 5hr & quenching •600°C for 2hr & 1200°C for 2hr & quenching •400°C for 1hr & 600°C for 2hr	Cubic	Different methods of synthesis with variety of pH's and solvents
Tzeng et al. (2005) [64]	zirconium oxyhalides or zirconium oxynitrates - tungsten powder or tungsten oxide – ammonia – water	600 to 800°C for 30min & 1180 to 1200°C for <5hr & quenching	Cubic	Ammonia as complexing agent
De Buysser et al. (2007) [5]	$ZrCl_2O \cdot 8H_2O$ - $(NH_4)_6H_2W_{12}O_{40} \cdot xH_2O$ – citric acid - water	aging time: 24hr 700 to 800°C for 12hr & 1180°C for 2hr & quenching	Cubic	The aim is to reach to clear gel by varying the pH by ammonia and Zr^{4+}:CA ratio
De Buysser et al. (2008) [62]	$ZrCl_2O \cdot NH_2O$ - $(NH_4)_6H_2W_{12}O_{40} \cdot 1.98\ H_2O$ – EDTA - water	1180°C for 2hr heating rate to reach 1180°C: 10°C/min & quenching	Cubic	One step heat treatment
Wilkinson et al. (1998) [9]	$Zr(OiPr)_4 \cdot iPrOH$ in CH_3OH - WCl_6 in (THF + iPr_2O)	•500°C for 2hr & 600°C for 1hr & 740°C for 30min (Trigonal phase was obtained) •1200°C for 15min (Cubic phase was obtained)	•Trigonal •Cubic	Crystallization occurred at about740 °C to a phase that was identified as being structurally related to trigonal $ZrMo_2O_8$.
Lind et al. (2002) [65]	$Zr(OiPr)_4 \cdot iPrOH$ in CH_3OH - WCl_6 in (THF + iPr_2O) – Seed	500°C for 2hr & 600°C for 1hr & 740°C for 30min	Cubic	Seed: small particles of cubic ZrW_2O_8.
Noailles et al. (2004) [49]	$(Zr[OCH(CH_3)_2]_4.(CH_3)_2CHOH$ - $WOCl_4$ - anhydrous 2-propanol	aging time: 1hr to 2 days (depending on molarity) 200 to 600°C for 15min 900°C for 30s 1100°C for 1.5min	•Amorphous (<700°C) •Trigonal (750°C<T <850 °C) •Cubic (> 900°C)	•Solvent to liquid CO_2 exchange took 1week. •Aerogel was obtained by supercritically drying of gel in liquid CO_2.
Kanamori et al. (2008) [8][1]	$ZrCl_2O \cdot 8H_2O$ in 2-butyl alcohol /ethyl alcohol /water solution - WCl_6 in ethyl alcohol	aging time: 72hr 450°C for 12hr & 520 to 680°C for 1hr	Cubic	Amorphous ZrW_2O_8 after calcination
Kanamori et al. (2009) [58][1]	$ZrCl_2O \cdot 8H_2O$ in 2-butyl alcohol /ethyl alcohol /water solution - WCl_6 in ethyl alcohol	aging time: 72hr 450°C for 12hr & 600°C for 10min in SPS	Cubic	Product with relative density of 98.6 was obtained by spark plasma sintering
Georgi et al. (2009) [6]	$ZrO(NO_3)_2 \cdot xH_2O$ - $(NH_4)_6W_{12}O_{39} \cdot xH_2O$ – citric acid – water	•740°C for 30min (Trigonal phase was obtained) •1125°C for 6sec (Cubic phase was obtained)	•Trigonal •Cubic	Smaller particle size (500nm to 20micron) was obtained.

[a] As the major solvents used in these researches are not water, the used method can also be categorized as non-hydrolytic sol-gel.

Two classes of methods were followed by researchers to sinter ZrO_2/ZrW_2O_8 composites which can be named as conventional [10, 74-76] and in-situ [74, 77, 78]. In conventional method ZrO_2 and ZrW_2O_8 powders were separately synthesized. Then the two powders were mixed, pressed and sintered generally just under the decomposition temperature of ZrW_2O_8. In-situ method followed the solid state reaction of off-stoichiometric mixture of ZrO_2 and WO_3. A rapid quenching step from the sintering temperature was needed in both methods in order to prevent decomposition of ZrW_2O_8 as it cools down between 1105 and 750°C. Regardless of the methods used, as formation of orthorhombic ZrW_2O_8 due to the high pressures applied in the pressing step [75] and low relative densities have been reported, the produced composites had relatively weak mechanical properties. It is noteworthy that in-situ method is capable of providing homogenous distribution of constituent oxides throughout the composite body. However, since formation of ZrW_2O_8 interfaces is necessary, it suffers from the prolonged sintering time and the increasing risk of WO_3 evaporation. To increase the sintered densities, Al_2O_3 was added as a sintering aid to the composite mixtures in quantities less than 0.35wt% [10, 15, 76, 77]. Higher quantities have led to increased risk of liquefaction and so loss of given shape. This is because of the existence of eutectics and the incongruently melting intermediate compounds with low melting points in the Al_2O_3-WO_3 system. As an alternative to lower the sintering temperature spark plasma sintering has been used [73], but it necessitated the use of nanoparticles produced from a precursor that has a complicated preparation method and air-sensitivity [8]. In addition, SiO_2 could only be added up to 30wt%, which implied that the CTE of composites remained negative.

By encapsulating the ZrW_2O_8 in the core of novel core-shell ZrO_2/ZrW_2O_8 composite particles one would be able to offer authentic solutions to the specific processing challenges faced. With such an encapsulation process one is capable of forming ZrO_2/ZrW_2O_8 interfaces with homogenous spatial distribution prior to sintering and attaining precise volume proportion of the constituent oxides along those interfaces which could be an asset to decrease interfacial stresses and so help in shape-retention during quenching from sintering temperature. Moreover, limiting the contacts between particles of the composite to ZrO_2/ZrO_2 during sintering will pave the way for future ZrW_2O_8-ceramic composites, in which ZrW_2O_8 and the other component have a process-limiting reactivity (i.e. composites between Al_2O_3 and ZrW_2O_8 could be possible with a buffer ZrO_2 layer in between). In this research, the ZrW_2O_8 particles obtained from a modified version of our previous method [66] was used to produce ZrW_2O_8/ZrO_2 core-shell composite particles. The ZrO_2 precursor was precipitated on the synthesized ZrW_2O_8 particles by means of urea hydrolysis and the factors affecting the rate of precursor precipitation was investigated. This was followed by a detailed analysis on the final phase distributions in the core-shell particles.

CHAPTER 3

EXPERIMENTAL

In this chapter, first the chemicals used in the study are given which is followed by the details of experiments conducted to modify the precursor preparation as well as heat treatment protocol of the previously developed sol-gel method. In the end, use of phase pure ZrW_2O_8 in production of core-shell ZrW_2O_8-ZrO_2 composite particles by urea hydrolysis is described.

3.1 Materials

In this study, Tungstic acid (TA) and zirconium acetate (ZrAc) are used as tungsten and zirconium sources, respectively, to prepare the precursor of the sol-gel process. Ammonia is used for dissolving TA. Zirconium(IV) oxychloride octahydrate (ZrOc) is used to prepare zirconia precursor of precipitation process and urea is used as the precipitating agent.

3.1.1 Tungstic Acid (TA) and Ammonia

TA is hydrated form of tungsten oxide, WO_3. TA is an intermediate product in tungsten factories which is aimed to produce tungsten from its minerals, scheelite and wolframite. Firstly, the mineral is fused with sodium carbonate in an iron crucible and the produced sodium tungstate is leached and crystallized. Secondly, the sodium tungstate is decomposed to TA by HCl or sulfuric acid [79]:

$$Na_2WO_4 + 2HCl \xrightarrow{heat} H_2WO_4 + 2NaCl \qquad (6)$$

$$Na_2WO_4 + H_2SO_4 \xrightarrow{heat} H_2WO_4 + Na_2SO_4 \qquad (7)$$

To achieve tungsten, the dried and calcined tungstic acid is reduced by charcoal within sealed clay crucible. In our research, the TA purchased from Aldrich was used.

TA is pale yellow solid powder with density of 5.59gr/cm^3. Upon heating, it is decomposed, rather than melting, at 100°C. TA is insoluble in cold water and most acids, slightly soluble in hot water and soluble in caustic alkalies, hydrofluoric acid and ammonia. Though TA is not soluble in cold water, TA which contains crystal water can be dissolved in water to some extent [80]. In this study, aqueous ammonia solution (32% NH_3) obtained from Merck is used to dissolve TA. The solution obtained from dissolution of TA in ammonia solution is called Ammoniacal Tungstic Acid (ATA) [81].

3.1.2 Zirconium(IV) Acetate (ZrAc)

Zirconium acetate with formula of $(CH_3COO)_xZr(OH)_y$ (where x+y=4) is industrially used in water repellents. It is clear to pale-amber liquid. One grade of zirconium acetate is available as 13% ZrO_2 aqueous solution with density of approximately 1.2 and pH of 3.3 to 4.0 at 20°C. It is stable at room temperature but rate of hydrolysis at lower temperatures increases as pH decreases [82]. The zirconium acetate solution used in our experiments was

purchased from Aldrich which includes approximately 16% zirconium in dilute acetic acid. Its density is 1.279gr/mL at 25°C.

3.1.2 Zirconium(IV) Oxychloride (ZrOc) and Urea

Zirconium(IV) oxychloride octahydrate, $ZrOCl_2 \cdot 8H_2O$, is industrially used in water repellants, cosmetic, textile, acidizing aid of oil fields, antiperspirants, etc. It is white silky crystals which loses $6H_2O$ upon heating on 150°C and $8H_2O$ upon heating on 210°C. Its density is 1.91gr/mL and it is soluble in water, methanol and ethanol and insoluble in other organic solvents [83]. Zirconium oxychloride from Merck was selected to precipitate zirconia precursor on zirconium tungstate particles. Urea which was obtained from Aldrich was used as precipitating agent.

3.2 Modification of Synthesis of Zirconium Tungstate

3.2.1 Recipe of Sol-Gel Method

A typical recipe of production of zirconium tungstate by sol-gel method developed previously in our group can be summarized as [66]:

- Preparation of 65mL ATA solution with molarity of 0.2M. **pH** of ATA solution was adjusted to **9.88**.
- To regard **stoichiometric ratio**, an aqueous solution of 0.1M ZrAc with equal volume was prepared and poured into a **burette**.
- While mixing the ATA solution by magnetic mixture, the ZrAc solution dripped by burette on ATA solution.
- After mixing for 2 hours, the formed gel was dried at 110°C and ground.
- The xerogel was calcined at 600°C for 3 hours to form zirconium and tungsten oxides solid mixture.
- The oxides mixture was pelletized by pressing at 60MPa.
- The pellet was heat treated at **1200°C** for 4 hours within **alumina crucible** in a **tubular furnace**.
- The fired pellet was quenched by dropping it into cold water to obtain the product.

3.2.2 Modified Sol-Gel Method

Modifications to the previous method were performed on both precursor preparation and heat treatment levels. Modifications on precursor level were:

- Applying 2wt.% excess TA relative to stoichiometric ratio.
- To centrifuge ATA solution to separate any undissolved TA remaining in the solution.
- Increase in pH of ATA solution over 11.00 by adding more ammonia.
- Applying simultaneous mixing of ATA and ZrAc solutions by syringe (M2) rather than adding ZrAc solution to the bulk of ATA solution by burette (M1).

Modifications on heat treatment level were:

- Decrease in sintering time from 4 to 2 hours.
- Decrease in sintering temperature from 1200 to 1180°C.
- Sintering in a chamber furnace rather than tubular one for ease of quenching.
- Using platinum type crucible rather than alumina.

Five experiments designed and combination of modifications was considered for each experiment which are given in Table 3.1. M2 was adopted as mixing method in experiments A and B. Moreover, excess TA was added while making ATA solution in these experiments.

In precursor level, excess TA and high pH of ATA solution were the modifications adopted in precursor level for experiment C. In experiment D in comparison with experiment C, instead of high pH of ATA solution, centrifugation of ATA solution was applied. To have a reference from previous method, experiment R was done, in which no modification in precursor level was used. But all modifications for heat treatment level were considered for experiment R. The heat treatment modifications were also applied for experiments B, C and D. Calcination process was the same for all experiments

Table 3.1 Experiments conducted to modify the sol-gel method to achieve phase pure product in which combination of modifications in both precursor and heat treatment levels has been considered in each experiment.

Experiment	Precursor Level				Heat Treatment Level			
	Excess TA	M2	High pH	Centrifuge	Chamber Furnace	Pt crucible	Sintering time (hr)	Sintering T (°C)
A	✓	✓	×	×	✓	✓	2	1200
B	✓	✓	×	×	✓	✓	2	1180
C	✓	×	✓	×	✓	✓	2	1180
D	✓	×	×	✓	✓	✓	2	1180
R	×	×	×	×	✓	✓	2	1180

3.2.3 Effect of pH of ATA Solution on Product Composition

In these experiments preparations of five ATA solutions with identical molarity of 0.2M but different pH was targeted. To achieve the goal, a stock of ATA solution with volume of, e.g. 100mL was prepared in which 2wt.% excess TA was regarded. The stock included some ammonia which increased the pH of the stock to 8.90. The undissolved TA of the stock was separated by centrifugation. In this step, the stock divided into five equal volume proportions and 5mL ammonia plus water was added to each solution to achieve 5×25mL ATA solutions with molarities of 0.2M. The amount of ammonia plus water added to each solution and pHs of final solutions are shown in Table 3.2.

Table 3.2 Composition and pH of five ATA solutions prepared to investigate the effect of pH of ATA solution on composition of the product.

ATA Solution Number	Volume of			Final Volume (mL)	Final pH
	Stock(mL)[a]	Ammonia(mL)	Water(mL)		
1	20.0	0.0	5.0	25.0	8.60
2	20.0	0.3	4.7	25.0	9.34
3	20.0	1.2	3.8	25.0	9.86
4	20.0	3.0	2.0	25.0	10.34
5	20.0	5.0	0.0	25.0	11.80

[a] pH of the stock was measured as 8.90.

Next, 5×25mL ZrAc solution with molarities of 0.1M were prepared and each added by burette to one of ATA solutions. The five gellous precursors were aged for two hours and dried at 110°C and calcined for three hours at 600°C to form zirconium and tungsten oxides

mixtures. The five oxides mixtures were pressed and heat treated in a platinum crucible for two hours at 1180°C in a chamber furnace and then quenched by dropping them into cold water.

3.3 Synthesis of ZrW_2O_8/ZrO_2 Core-Shell Composite Particles

The aim of these experiments was to precipitate ZrO_2 precursor on ZrW_2O_8 particles by urea hydrolysis method. Typically, 2gr of zirconium tungstate core particles was dispersed in 50mL aqueous solution that was prepared by dissolving appropriate amount of zirconium oxychloride in it. The mixture, then, was mildly sonicated at room temperature and heated to 93±1ºC. While continuously mixing with a magnetic mixer at elevated temperature the mixture was refluxed. As precipitation agent, 25mL urea solution was prepared by dissolving appropriate amount of urea in water and added to the refluxing mixture. Upon the addition of urea solution into refluxing mixture, temperature was decreased to about 80ºC momentarily, but recovered to reaction temperature in less than 5 minutes. The pH and temperature of the reaction mixture were continuously recorded until the end of reaction. Once the temperature of reaction mixture was recovered, data collection was initiated and when the reaction was considered finished (i.e. leveling off of the reaction pH around 6.00), the precipitate was filtered and washed by water and isopropyl alcohol. The filtered cake was dried in an oven at 110°C overnight and calcined at 500°C for 4 hours. In order to adjust volume ratio of ZrO_2: ZrW_2O_8 in the final core-shell particles, initial zirconium source concentrations, and to change the rate of reaction, urea concentrations in the mother liquor were varied. Table 3.3 presents the conditions of experiments. In one experiment (i.e. D*), the effect of an initial increase in pH before the addition of urea solution to the refluxing mixture was assessed. For this, ammonia was dripped into the $ZrOCl_2$/ ZrW_2O_8 mixture to increase the initial pH from 2.21 to 2.64.

The ZrW_2O_8 powder which was used as core was prepared in five batches with the procedure given in experiment C of section 3.2.1. Batch 1 was heat treated at 1180°C while other batches heat treated at 1150°C. The product of batch 1 was used only in experiment A. The products of the four batches heat treated at 1150°C, batch 2, 3, 4 and 5, were mixed and used in experiments B, C, D and D*.

Table 3.3 Conditions of precipitation experiments.

Experiment	ZrW_2O_8 (gr)	[ZrOc] (M)	[Urea] (M)	[Urea]/[ZrOc]
A[a]	0.3	0.0080	0.5	63
B	0.2	0.0053	1.0	189
C	0.2	0.0121	0.5	41
D	0.2	0.0121	1.0	83
D*, [b]	0.2	0.0121	1.0	83

[a] In the discussions related to rate of precipitation from each solution, Experiment A should be excluded since the amount of 'core' particles which potentially act like seeds is different in this experiment.

[b] In Experiment D*, initial pH of the solution was increased by approximately half a pH unit with ammonia addition before mixing urea solution into the reaction mixture.

3.4 Characterization Methods

XRD (X-ray Diffraction), PSA (Particle Size Analysis) and SEM/EDX (Scanning Electron Microscope/Energy Dispersive using X-ray) were the characterization methods used in this research. Instrumental specifications and details of the methods are described in this section.

3.4.1 XRD (X-ray Diffraction) Analysis

The structural characterization of synthesized zirconium tungstate and composite particles were performed by the X-Ray Diffraction instrument located at Department of Metallurgical and Materials Engineering, METU (Model No: RIGAKU – D/Max-2200/PC) by using CuKα (λ = 0.154 nm) radiation at 40 kV and 40 mA and 2θ values of 10^o and 80^o. The peak assignments were carried out by comparing the peaks with standard XRD peaks of ZrW_2O_8, ZrO_2 and WO_3. The standard peaks were gathered from JCPDS card of the intended materials which can be found in Appendix A. In the absence of cards or doubt, as an alternative standard peaks of a phase of ZrW_2O_8 (e.g. γ-ZrW_2O_8) were extracted by CaRIne Crystallography (version 3.1) software. Details of the extraction method are described in Appendix B. The adjacent overlapped peaks were deconvoluted by Peak Fit™ (version 4.11). Details of the method are described in Appendix C. The area underneath or normalized intensity of the most intense peak of the components extracted from the software can be utilized to calculate the composition of impure zirconium tungstate product or composite particles. To calculate the primary crystallite size of any component, Scherrer equation is commonly used which can be written as:

$$t = \frac{s \times \lambda}{F \times \cos(\alpha)} \qquad (8)$$

where; t = thickness of crystallite (nm)
s = constant shape factor of the crystallite
λ = X-ray wavelength (nm)
F = Corrected full-width at half-maximum, FWHM, of the peak (radians)
α = Bragg angle (^{o})

Shape factor, s, is geometrical constant of the unit cell which is usually between 0.85 and 0.99. Shape factor is considered as 0.9 in this study. FWHM of the peaks can also be extracted from peak analysis with Peak Fit software. To calculate an accurate size from Scherrer equation, the FWHM of the peak should be corrected considering the peak broadening due to the instrument. Here, FWHM of a well-crystallized zirconium tungstate synthesized by the modified sol-gel method was used to calculate corrected FWHM values.

3.4.2 PSA (Particle Size Analysis)

Particle sizes and distributions were determined by laser diffraction with a wide angle particle size analyzer (Malvern Zetasizer Nano Instrument – Model No: ZEN3500, and Mastersizer 2000, Malvern Instruments Ltd.).

3.4.3 SEM (Scanning Electron Microscope) Analysis

The morphological characterization of zirconium tungstate and core-shell particles was performed by a scanning electron microscope in Central Laboratory, METU (Model No: Quanta FEI 400F Field Emission SEM) equipped with an energy dispersive X-ray spectroscope probe which was used in semi-quantitative analyses of elemental composition of the composite particles. The specimens were sputtered with gold before analysis.

CHAPTER 4

RESULTS AND DISCUSSIONS

4.1 Preliminary Study on Sol-gel Synthesis of ZrW_2O_8

Synthesis of zirconium tungstate by high temperature approach which is based on phase diagram of WO_3- ZrO_2, inherently bears several constraints which underestimating any of them leads to synthesis of impure product. Figure 1.1 shows that zirconium tungstate is stable in a very narrow strip on temperature-composition surface. Horizontally, the strip is confined within a composition range which is in very close proximity to the stoichiometric ratio of W:Zr in $Zr(WO_4)_2$. On the other hand, as the reaction is solid state type, the inhomogeneity of ZrO_2 and WO_3 mixture is a concern which can potentially deviate the actual stoichiometric ratio from apparent ratio gained from solely mixing stoichiometric grams of the oxides. Applying wet chemical methods is an asset to decrease the inhomogeneity of the mixture which typically occurs in the reaction of solid stately mixed oxides, but still does not guarantee the homogeneity of oxides mixture achieved after calcination of dried precursor of the wet chemical method. Agglomeration of dispersed species of the W and Zr sources in the mixture, formation of polyionic species which is common among salts of transient metals and immiscibility of Zr and W sources in the solvent are the recurring phenomena which disturb homogeneity of mixture of Zr and W sources in the precursor. Consequently, an ideal homogeneous mixture of zirconium and tungsten oxides could not be expected from calcined xerogel or precipitates. Therefore, to achieve phase pure product from sintering of such inhomogeneous oxides mixture, the dwelling time in the furnace must be increased to provide the adequate opportunity to the oxides to diffuse to each other from increased distance as a result of inhomogeneity. The homogeneity disturbing phenomenon in the sol-gel method developed in our group was mostly due to insolubility of TA in water. Though TA is soluble in ammonia solution, it does not form a miscible aqueous solution at room temperature so ATA remains as a turbid colloidal mixture. Adding more ammonia to the ATA mixture which increases the pH and mixing the ATA mixture by ultrasonic horn can increase the solubility of TA in ATA mixture. Applying slightly more than stoichiometric ratio of W:Zr sources as well as centrifugation of ATA solution to separate the undissolved TA particles from ATA mixture can also be beneficial in attaining more homogeneous oxides mixture. Another improvement can be proposed by changing the way ATA and ZrAc solution are mixed. In the former method, ZrAc solution is added to the mixing ATA solution by burette. Regarding the gradual increase of TA in ZrAc solution as well as increase in viscosity as a result of gelation it necessitates aggressive mixing to reach to a uniform gel. In the modified method ATA and ZrAc solutions are charged into two syringes and dripped into a beaker in which some water was poured. The tips of the syringes are adjusted in a way that the ATA and ZrAc drops were partially mixed at the tips of the syringes before falling into the beaker. In this way, the concentrations of both Zr and W sources increase simultaneously. Hence, the precursor would be expected to be more homogeneous and the aging time would decrease.

Stoichiometric ratio of W:Zr can also deviate as a result of volatility of WO_3 at elevated temperature of 1200°C. Having such a constraint in the process limits both sintering temperature and dwell time at elevated temperatures. Applying covered crucible [51, 52] and use of the W source slightly more than stoichiometric ratio [51] have been proposed in the papers to counter measure this problem.

The zirconium tungstate strip is vertically restricted between 1230 and 1250°C on phase diagram. Wet chemical methods are capable of synthesis of zirconium tungstate at lower temperatures, e.g. 1180°C, and short dwell time as 2 hours [5, 62]. Therefore, such methods can effectively resolve the stoichiometry problems that would potentially arise from volatility of WO_3. As reactive sintering of tungsten and zirconium oxides take places at this high temperature range, crucible material should be inactive in the reaction. Any effect of crucible on diffusivity of the oxides or reactively taking part in the reaction will lead to impure product. Platinum type crucible is commonly used as sintering medium in synthesis of zirconium tungstate. The reason why alumina crucibles give negative results should be examined.

Having lower stability limit of 1230°C implies the metastability of zirconium tungstate. To have the pure product stable at room temperature the sintered body should be quenched fast enough to temperatures where it would remain kinetically stable. Hence, the design of furnace should facilitate the rapid removal of the hot crucible and dropping into cold water. Chamber type furnaces, rather than tubular ones, are the most suitable type for this purpose. The proposed modification for both precursor and heat treatment levels are represented in fish-bone chart in Figure 4.1.

4.2 Modifications on Sol-Gel Method

XRD pattern of a sample prepared by our previous sol-gel method [66] is given in Figure 4.2. The pattern exhibits peaks of ZrW_2O_8 as well as its constituent oxides. The purity of the sample was calculated as 64vol.% which was the greatest purity obtained by his method [66].

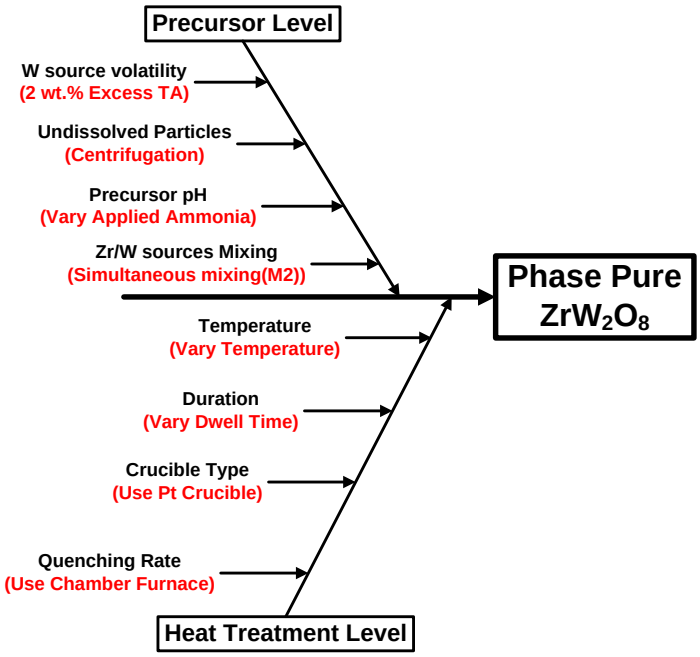

Figure 4.1 Fish-bone representation of potential modifications of the sol-gel method developed in our group.

Figure 4.3 represents the XRD patterns of the products of the experiments performed to modify the former sol-gel method. As the peaks belonging to ZrO_2 and WO_3 are nearly eliminated, it can be deduced that the modifications effectively made a leap toward achieving phase pure product. Except the products of experiment A and R which represent minor ZrO_2 and WO_3 peaks respectively, the products of the other experiments can be considered as phase pure. Attaining a nearly phase pure product from experiment R infers that heat treatment countermeasures played more influential role on achieving pure product than the ones in precursor level.

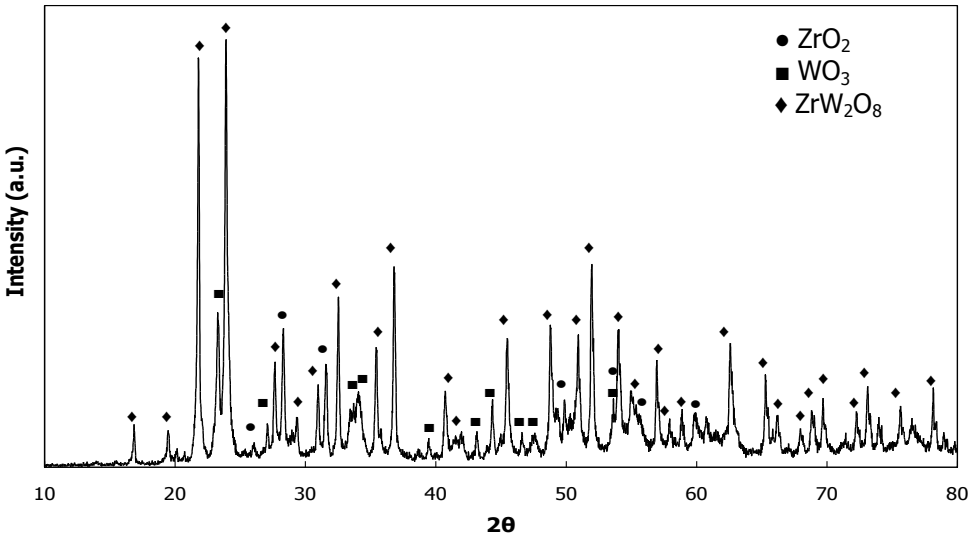

Figure 4.2 XRD pattern of a typical specimen prepared by former sol-gel method developed in our group [66].

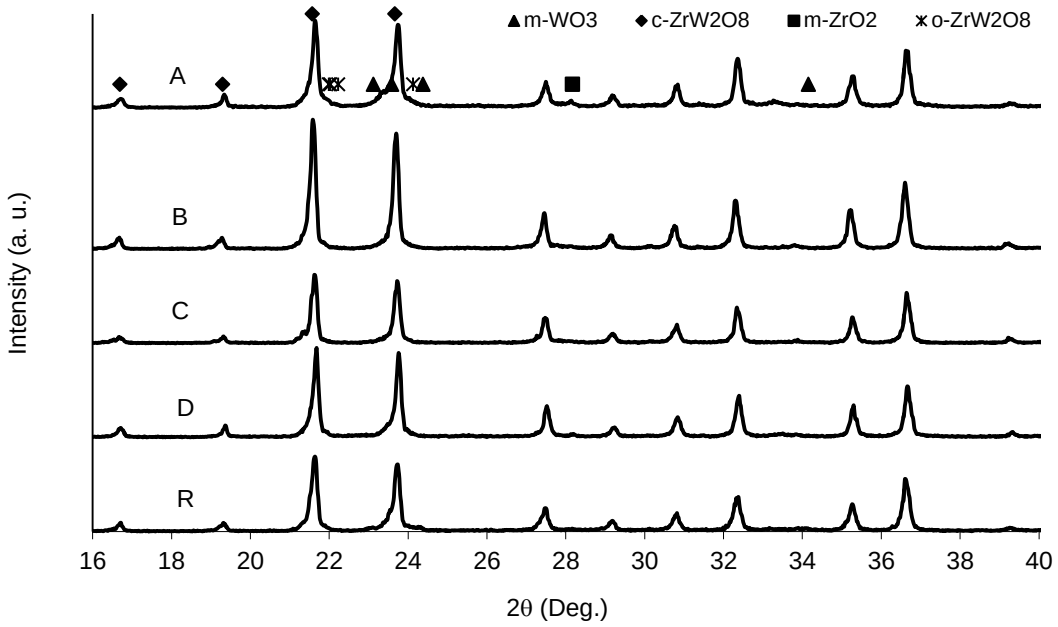

Figure 4.3 XRD pattern of the products from modified sol-gel experiments.

Except heat treatment temperature, experiments A and B had the same preparation parameters. Having a minor ZrO_2 peak in experiment A implies that reducing dwell time from four hours to two hours was not adequate to prevent the impurity arising from volatility of WO_3 and a decrease in temperature was also needed. On the other hand, reaching to phase pure product from experiment B shows that two hours dwell time at 1180°C was well enough to complete reactive sintering of constituent oxides.

To check the effect of further decrease in temperature, three identical calcined precursors were heat treated at 1150, 1140 and 1130°C for two hours, respectively. The results of XRD analyses are shown in Figure 4.4 which confirms that as the temperature decreased the intensity of WO_3 peaks increased. Therefore, with dwell time of two hours, heat treatment at 1150°C or less was not sufficient to achieve phase pure product.

To justify the role of crucible type in the purity, a precursor was prepared based on the conditions of experiment C and the tablet of calcined and pressed precursor was put on a piece of alumina pellet and located in the platinum type crucible and then heat treated at 1180°C. Figure 4.5 illustrates the XRD pattern of the product achieved from this experiment. The WO_3 and ZrO_2 peaks appeared in the pattern infer that alumina imparted in the reaction between WO_3 and ZrO_2. The peaks in the XRD pattern belong only to ZrO_2, WO_3 and ZrW_2O_8. This is because of the fact that WO_3 which reacted with the sintered alumina walls of the crucible remains on the walls and cannot be separated.

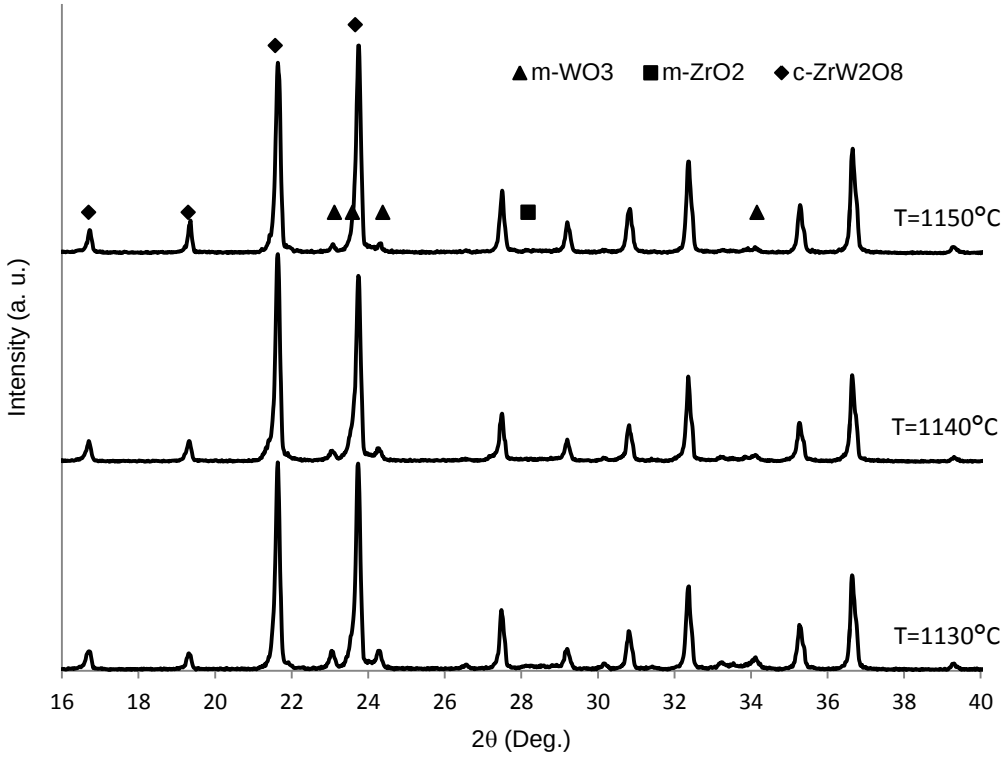

Figure 4.4 XRD pattern of the products treated at different temperatures; 1150, 1140 and 1130°C.

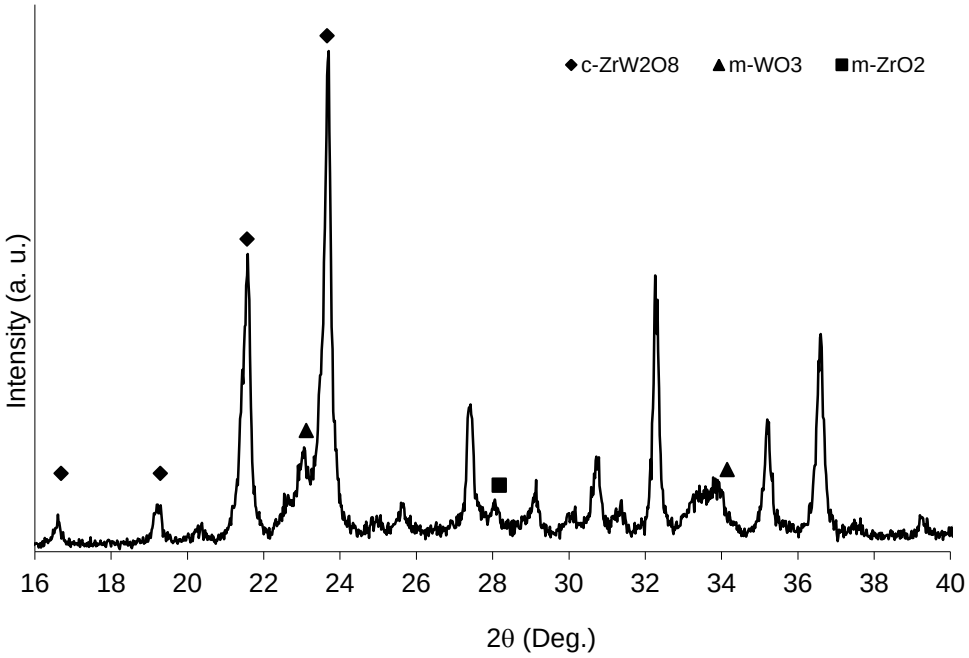

Figure 4.5 XRD pattern of the sample prepared to identify the role of alumina type crucible on the purity of the product.

Due to the evident effect of chamber type furnace on facile quenching of the heat treated ceramic, treatment in platinum type crucible in a chamber furnace had the most dominant effect on achieving phase pure product. On the other hand, existence of small intensity peaks of WO_3 in experiment R in comparison with phase pure products of experiments B, C and D declares the role of precursor level modifications on fine tuning of the product purity. As the reaction of WO_3 and ZrO_2 could take place at low temperature of 1180°C and short dwell time of two hours, the modifications in precursor level which aimed to countermeasure volatility of WO_3 might be of less effect. Among the precursor level modifications, as pH can vary in a wide range over 7, precise verification of its effect on purity and determination of the pH above which the product would be phase pure was worthy of investigation. XRD patterns of the ZrW_2O_8 products synthesized from precursors with different pH values to investigate the effect of pH values of ATA solution on product composition are given in Figure 4.6. Products were mainly cubic ZrW_2O_8 (c-ZrW_2O_8) but minor peaks of impurities can be distinguished. As the standard peaks of product constituents are in close vicinity, Peak Fit™ software was used to deconvolute the overlapped peaks and extract the composition of phase mixture. Results of the peaks analysis are tabulated in Table 4.1. Monoclinic WO_3 (m-WO_3) that was distinguished in products from precursors with higher pH values (approximately 10.3vol.% at pH 10.34), was observed to be reduced with decreasing pH (approximately 5.3 and 5.1vol.% at pH's 9.86 and 9.34). It was totally removed at pH of 8.60. On the other hand, while it was not present at pH 10.34, monoclinic ZrO_2 (m-ZrO_2) started to increase in quantity with decreasing pH (approximately 3.8, 4.4 and 10.3vol.% at pH values of 9.86, 9.34 and 8.60, respectively). When pH value was adjusted at above 11, such as 11.44 and 11.80 (Figure 4.6) neither ZrO_2 nor WO_3 was found to exist in the product. Therefore, to achieve a phase pure product keeping pH of ATA solution higher than 11 was necessary.

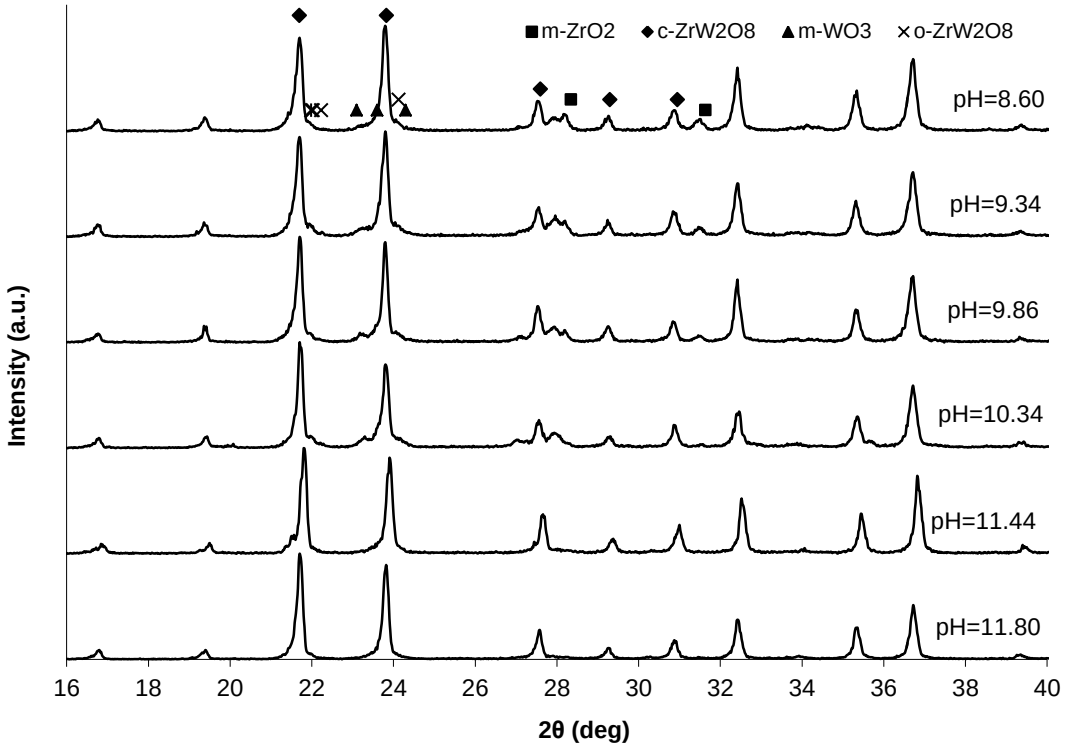

Figure 4.6 XRD patterns of the products yielded from precursors with varied pH's of ATA solution.

Table 4.1 Phase mixture of the products yielded from precursors with varied pH values of ATA solution.

pH	Composition (vol. %)			
	WO_3 (2θ=23.12°)[a]	m-ZrO_2 (2θ=28.18°)[a]	c-ZrW_2O_8 (2θ=21.57°)[a]	γ-ZrW_2O_8 (2θ=22.03°)[a]
8.60	0.0	10.3	89.7	0.0
9.34	5.1	4.4	90.5	1.8
9.86	5.3	3.8	90.9	1.1
10.34	10.1	0.0	89.9	1.8
11.80	0.0	0.0	100.0	0.0

[a] location of the most intense peak which was used to calculate the composition of the products in peak analysis.

At all pH values experimented, the amount of γ-ZrW_2O_8 was found to vary between 1 and 1.8 vol.%. Formation of γ-ZrW_2O_8 was attributed to the cold pressing of calcined oxides mixture which was sufficient to make a phase transition from α to γ phase [75]. To evaluate the effect of pressing on purity and phase behavior of the product, half of the oxides mixture resulted from calcination of a desiccated precursor were pressed into tablet from and the other half left in powder form. The tablet and powder were treated in platinum crucible at 1200°C simultaneously. The XRD patterns of the products are shown in Figure 4.7. Although both products includes minor impurity of constituent oxides, which regarding the sintering temperature and pH of ATA solution (pH was equal to 10.8) is expected, the peaks of the

impurities were of the same intensities. Therefore, pressing of calcined powder which is believed to facilitate counter-diffusion of zirconium and tungsten oxides during reactive sintering process, did not have significant effect on purity of the product. On the other hand, the XRD pattern related to pressed specimen represents traces of γ-ZrW_2O_8 of which the powder form is free. Therefore, pressing step after calcination can be eliminated from the procedure as long as the quenching step can be applied with the same efficiency for the powder form.

Although pH of ATA solution in experiments B and D were 10.3 and 10.5 respectively, like the product from precursor with pH of ATA solution more than 11, phase pure products were achieved from these precursors. As higher pH which was achieved by adding more ammonia lead to higher dissolution of TA in water, it may be deduced that in pH's less than 11 an auxiliary measure like embracing of Zr and W sources before gel formation (experiment B) or separation of undissolved particles (experiment D) in necessary to implement better dispersion of the Zr and W sources within precursor. Moreover, as far as the simplicity of the sol-gel procedure is concerned, phase pure product can be achieved by increasing pH over 11 without applying centrifugation or mixing method M2.

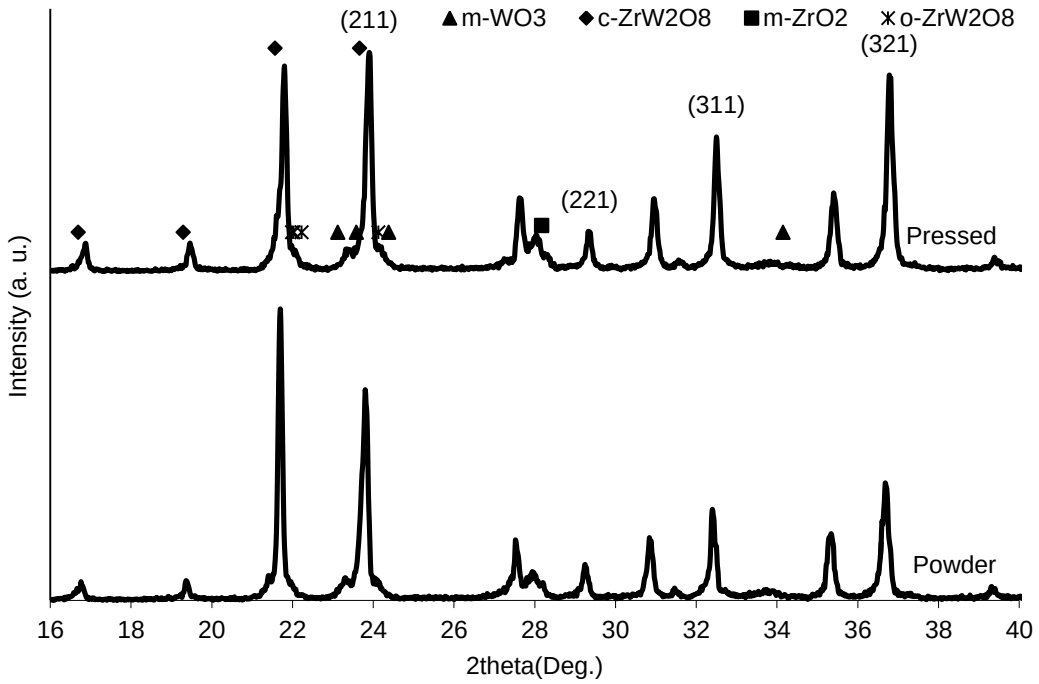

Figure 4.7 XRD patterns of the products yielded from heat treatment of the same calcined mixture; half of mixture was pressed and half was left in powder form.

4.3 ZrO_2-ZrW_2O_8 Core-Shell Composite Particles

4.3.1 Synthesis

Figure 4.8 (a) and (b) show the XRD patterns of ZrW_2O_8 cores used for the production of core–shell particles. The ZrW_2O_8 particles used to conduct experiment A was from a batch that was heat treated at 1180°C.

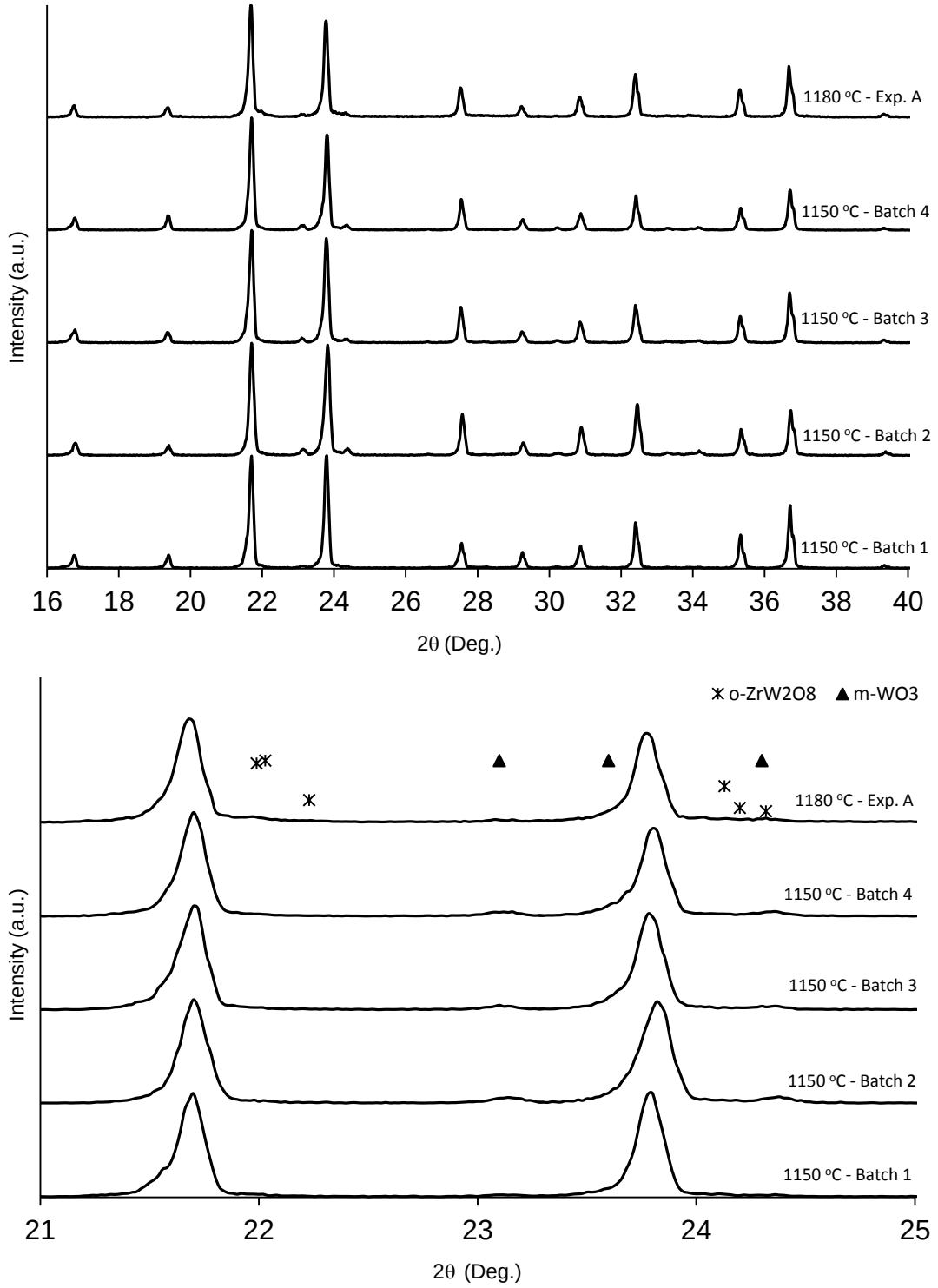

Figure 4.8 XRD patterns of (a) ZrW_2O_8 products used in the production of core–shell particles. (b) A zoomed section (21–25°) from the patterns given in (a) with the marked positions and relative intensities of standard peaks of m-WO_3 and γ-ZrW_2O_8 phases.

On the other hand, a mixture of four separate batches that were heat treated at 1150°C were used in experiments B, C, D and D*. Final pH values of all the precursors were set between 10.50 and 10.60.

Performing peak fit analyses, m-ZrO_2, m-WO_3 and γ-ZrW_2O_8 phases were calculated to be less than 2vol.% in the well-crystalline obtained products. γ-ZrW_2O_8 was negligible in all four batches but, based on the estimation from each XRD pattern, there is approximately 1.5 vol.% m-WO_3 in their mixture. On the other hand, about 1 vol.% γ-ZrW_2O_8 was calculated to be existent in the core particles of experiment A, but actually no m-WO_3. All five batches were free of ZrO_2. This information is summarized in Table 4.2. The average particle size of the core particles was measured to be 8 µm (d10 = 0.6 µm and d90 = 22 µm).

Table 4.2 Phase mixture of the products of different experiments.

	Experiment				
	A	B	C	D	D*
ZrW_2O_8 (vol.%)	60	59	34	32	33
γ-ZrW_2O_8/c-ZrW_2O_8 (vol./vol.)	0.02	0.00	0.03	0.06	0.01
ZrO_2 (vol.%)	40	41	66	68	67
c-ZrO_2/t-ZrO_2 (vol./vol.)	0.08	0.21	0.22	0.00	0.05
$ZrOCl_2$/ZrW_2O_8 Solution(mol/mol)[a]	1.18	1.18	2.66	2.66	2.66
ZrO_2/ZrW_2O_8 Predicted (vol./vol.)[b]	0.22	0.22	0.5	0.5	0.5
ZrO_2/ZrW_2O_8 XRD (vol./vol.)[c]	0.67	0.69	1.94	2.13	2.03
ZrO_2 in the Core	×	×	×	×	×
m-WO_3 in the Core	×	√	√	√	√
m-WO_3 in the C/S[d]	×	√	√	√	√
γ-ZrW_2O_8 in the Core	√	×	×	×	×
γ-ZrW_2O_8 in the C/S	√	×	√	√	√

[a] Molar ratio of Zr^{4+} ions to ZrW_2O_8 particles in the mother liquor.
[b] Predicted volume ratio of shell to the core. In calculations, all Zr^{4+} ions are assumed to be precipitated on ZrW_2O_8 particles and calcined to ZrO_2 during heat treatment.
[c] Actual volume ratio of shell to the core according to XRD results.
[d] C/S: core-shell

4.3.2 Reaction Analysis

When an aqueous solutions of urea ($CO(NH_2)_2$) is heated at approximately 90°C it slowly decomposes into ammonia and cyanate in the first step. Cyanate decomposes into ammonia and carbonic acid in the second step. The detail of reactions and associated acid/base equilibria are [84]:

$OC(NH_2)_2 \rightarrow NCO^- + NH_4^+$ (9)
$NCO^- + 2H_2O \rightarrow NH_3 + HCO_3^-$ (10)
$NCO^- + 2H_2O + HCO_3^- \rightarrow NH_3 + 2HCO_3^-$ (11)
$NCO^- + 2H_2O + NH_3 \rightarrow 2NH_3 + HCO_3^-$ (12)
$HNCO + H_2O + H^+ \rightarrow NH_4^+ + CO_2$ (13)
$HNCO + H_2O \rightarrow NH_3 + CO_2$ (14)
$H_2O \rightarrow H^+ + OH^-$ (15)

$NH_4^+ \rightarrow NH_3 + H^+$ (16)
$CO_2 + H_2O \rightarrow HCO_3^- + H^+$ (17)
$HCO_3^- \rightarrow CO_3^{-2} + H^+$ (18)
$HNCO \rightarrow NCO^- + H^+$ (19)

Reactions 9 to 14 are independent reactions related to the decomposition of the urea and hydrolysis. Equations 15 to 19 are acid/base equilibria coupled with the decomposition of urea products which include carbonic acid, ammonium ion, and cyanic acid dissociations. The overall acid/base dissociation creates a slow and homogeneous increase in the pH of the aqueous solution. Control of size and size distribution can also be added to the advantages of this method. This mechanism of homogenous introduction of the precipitating agent has been used in precipitation of precursor of several metal oxides [84].

Figure 4.9(a) shows the trend of pH of the reaction mixtures with time at 93±1°C. The initial values of pH were in the range of 2.00–2.50. The values of pH increased rapidly when urea started to decompose. The pH trends of the experiments show that supersaturation level was at a pH between 4.00 and 4.50 in which heterogeneous nucleation of ZrO_2 precursor on ZrW_2O_8 particles started. This was followed by the growth of the particles. pH tended to stabilize at 6.00–6.50 which is indication of consumption of $ZrOCl_2$ in the reaction mixture. The interaction in the reaction mixture dominant of which is the interaction between zirconium ions and hydroxyl ions released by the decomposition of urea formed an "S" shape curves in pH versus time graphs of all experiments. In contrast with some late transition metal ions (like Ni^{2+}) which form variety of complexes with products of decomposition of urea, early transition metal ions (like Zr^{4+}) react mainly with hydroxyls. Hence, unlike the rate of precipitation with late transition metal ions which is not easily predictable [84], the precipitation system with Zr^{4+} is quiet well-behaved. Therefore, in this system, the time required to reach to the deflection point of the time trend of pH curves can be assigned as an appropriate criterion for the rate of reaction. It can be seen that experiment B which reached to the deflection point in 8 minutes, had the highest reaction rate. Among the experiments, experiment B had the lowest $ZrOCl_2$ and highest urea initial concentrations (Table 3.3). On the contrary, the slowest reaction rate among the experiments was experiment C with 21 minutes. This experiment was performed with the highest $ZrOCl_2$ and lowest urea initial molarities. Experiments D with 15 minutes represented an intermediate rate. Therefore, [Urea]/[$ZrOCl_2$] ratio can be taken into account as a consistent yardstick to predict the rate of reactions (Figure 4.9(b)). The time for experiment D* with the same initial concentration of chemicals as experiment D but higher initial pH (2.64 rather than 2.21) was decreased to 9 minutes. This puts forward the assisting function of initial increase in the pH of reaction mixture in increasing the rate of precipitation as well as the dominant contribution of hydroxyls in the precipitation.

4.3.3 Composition and Phase Analyses

Figure 4.10(a) and (b) give the XRD patterns of the core–shell particles synthesized in the experiments. Position of standard peaks of c-ZrW_2O_8 (JCPDS 50-1868), γ-ZrW_2O_8 (JCPDS 56-566), m-ZrO_2 (JCPDS 37-1484), tetragonal ZrO_2 (t-ZrO_2) (JCPDS 17-0923), cubic ZrO_2 (c-ZrO_2) (JCPDS 27-0997) and m-WO_3 (JCPDS 43-1035) are indicated on the graph. The full range XRD data for these materials are given in the Appendix A. None of the products contains any monoclinic ZrO_2 phase, but t-ZrO_2 evidently existent in all products. As the positions of standard peaks of c-ZrO_2, t-ZrO_2, c-ZrW_2O_8 and γ-ZrW_2O_8 are very close to each other, peaks in the range of 28° to 32° had the tendency to merge to give a broad cluster of peaks. Therefore, to determine the presence of c-ZrO_2 peak deconvolution analysis is

necessary. On the other hand, as Figure 4.10(b) represents, the most intense peaks of c-ZrW_2O_8 and γ-ZrW_2O_8 are located around 22.0° and those of c-ZrO_2 and t-ZrO_2 are situated around 30°. Hence, to find the volumetric composition of ZrO_2 and ZrW_2O_8 phases in the resultant mixtures of core–shell particles the ranges from 21.0 to 22.5° and 28.5 to 31.5° should be deconvoluted separately. As an example, Figure 4.11 illustrates the deconvolution analysis executed on XRD pattern of the product of experiment A from 21.0 to 22.4° and 28.5 to 31.5°, respectively. Before deconvolution, the observed peaks were generated by performing several refinement processes. To calculate the composition of the phases in the each product, the intensity of corresponding standard peak in the JCPDS cards was assisted to normalize the area underneath of the peaks extracted from deconvolution software. Results of the analyses are presented in Table 4.2. The details of peak fit analyses and numerical data extracted from the analyses are given in Appendix C.

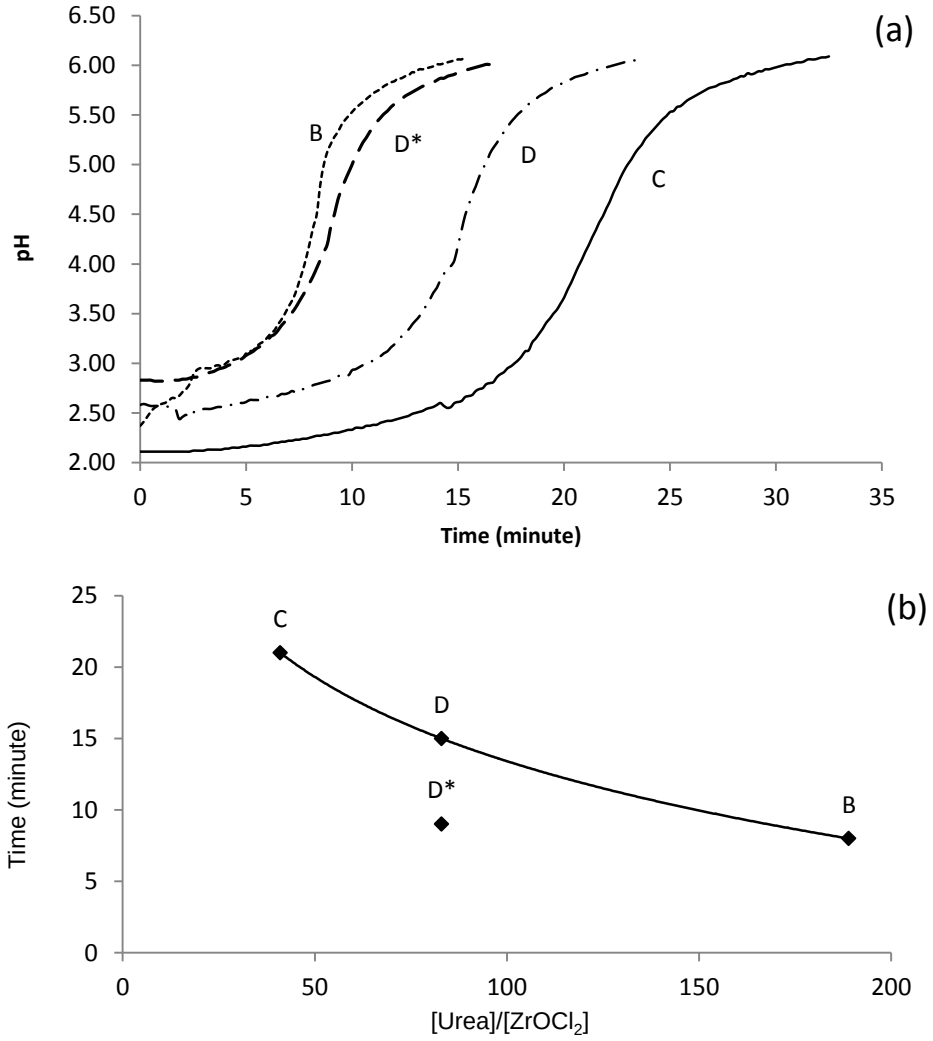

Figure 4.9 (a) Trends of pH variation with time in different experiments (as the amount of 'core' particles which act as seeds is different in experiment A, this experiment is excluded from the plot), (b) Rate of precipitation with respect to the [Urea]/[$ZrOCl_2$] ratio. Time needed to reach to the deflection point of the pH versus time curves was used as time values of y-axis.

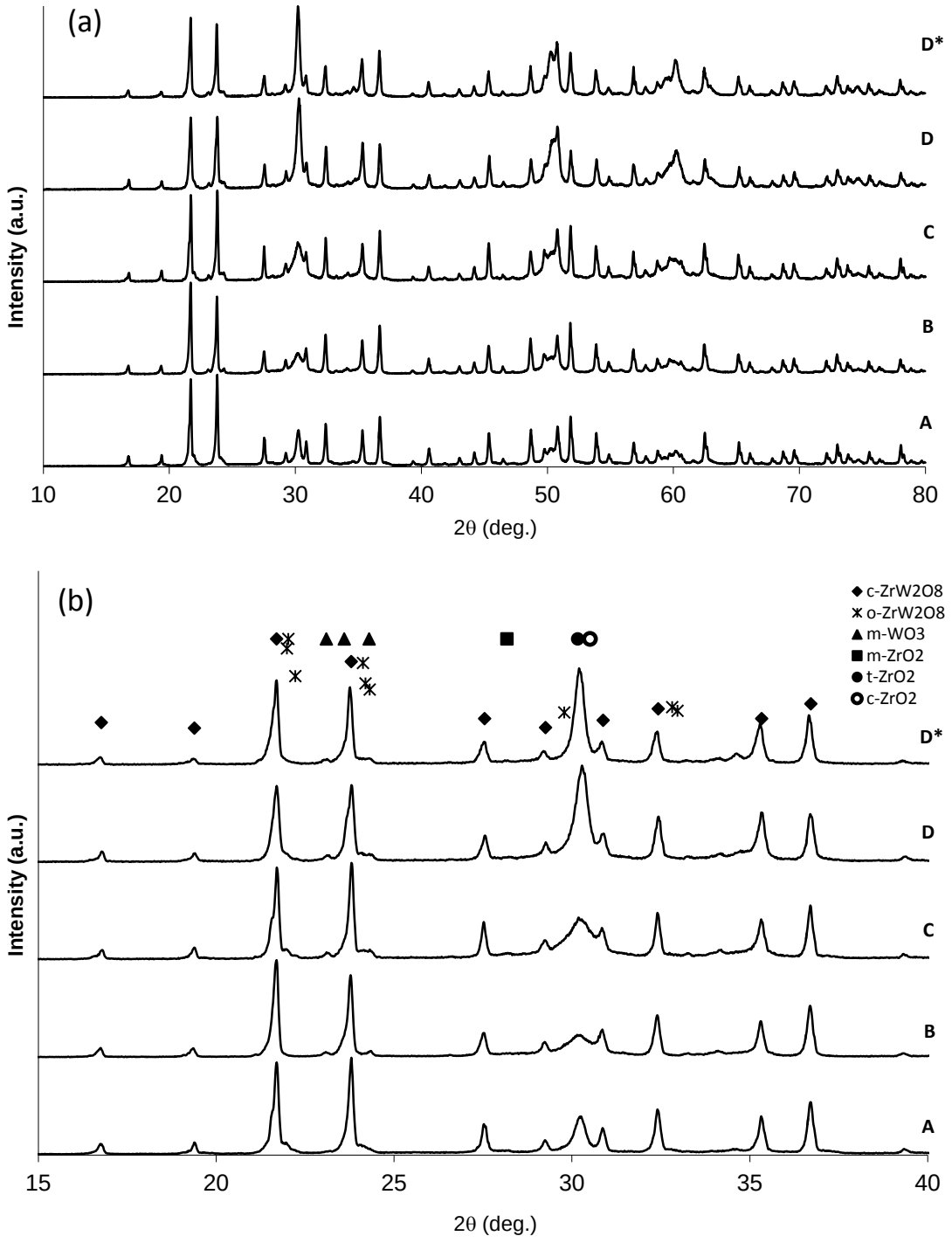

Figure 4.10 (a) XRD patterns of core–shell particles produced in experiments. (b) For clarity data are given between 15° and 40° 2θ. Positions and relative intensities of standard peaks of the phases are marked.

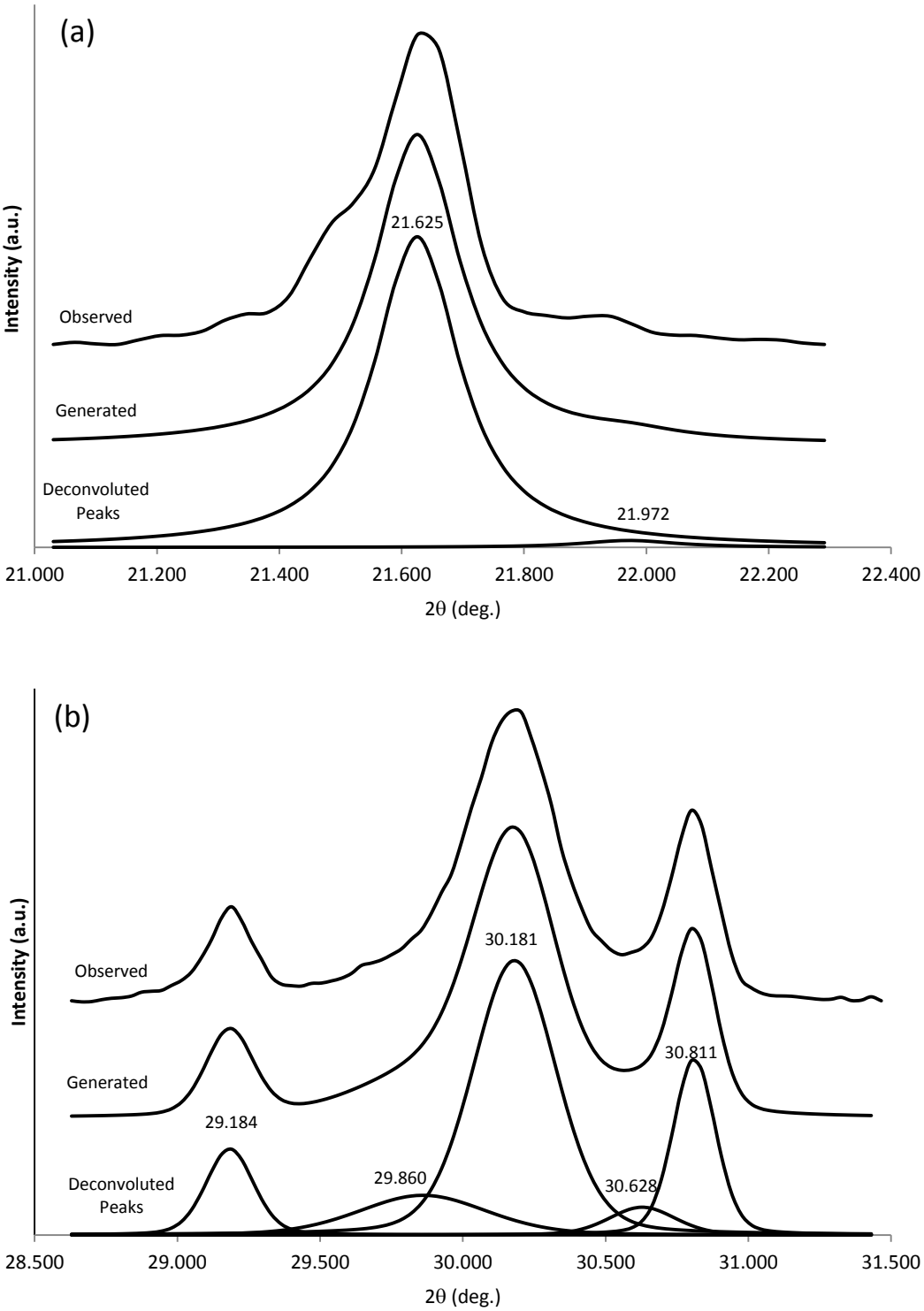

Figure 4.11 Deconvolution analysis performed on XRD pattern of the product produced in experiment A. The observed peaks between 21.0 to 22.4° (a) and 28.5 to 31.5 (b) were generated and deconvoluted into two and five peaks respectively.

The ideal precipitation with highest yield would result when all $ZrOCl_2$ existing in the reaction mixture precipitated in the form of ZrO_2 precursor, and subsequently calcined to ZrO_2. For such ideal case maximum achievable ZrO_2 was predicted for each experiment and ZrO_2/ZrW_2O_8 volume ratio was calculated as an index for progress of precipitation reactions. The ideal ratios were compared with actual volume ratios extracted from the XRD phase analyses (Table 4.2). From the comparison, XRD results demonstrated a positive variation from predicted values. The difference was increased by increase in $ZrOCl_2/ZrW_2O_8$ molar ratio which can be justified by the limited penetration of X-ray to the core of the particles and, consequently, a relatively less expression of core phase with an increase in the shell thickness. Another noteworthy fact is that, the same ideal volume ratios resulted in approximately the same values among the equivalent actual ratios. This also supports the above-mentioned justification and renders the discussion of the analyses persuading.

Another fact reveals itself upon comparison of ZrO_2 precipitated as the shell of the products of experiments C, D and D*. Within this series initial $ZrOCl_2$ concentration and amount of dispersed ZrW_2O_8 were the same but urea concentrations or initial values of pH in the reaction mixture were different. As the amount of ZrO_2 precipitated as shell phases of these products were nearly the same it can be claimed that neither concentration of urea nor an initial raise in pH by ammonia affected the final ZrO_2 existent in the products of these experiments. Furthermore, as leveling off of pH at proximity of 6.00 in all experiments implies, precipitation of ZrO_2 precursor was thorough. Experiments A and B with different $ZrOCl_2$ initial concentration and ZrW_2O_8 quantity but with the same $ZrOCl_2/ZrW_2O_8$ molar ratio were also independent of urea concentration so that variation of the concentration from 0.5 to 1.0 M did not significantly affect the progress of the precipitation of ZrO_2 precursor reaction, provided time is allowed for urea decomposition, which is known to be first order with respect to initial urea concentration. Therefore, it can be said that the molar ratio of $ZrOCl_2/ZrW_2O_8$ in the solution is maintained in the products. From EDXS analysis executed on two arbitrary regions of the particles of experiments D and D*, Zr/W atomic ratios were calculated as 2.61/2.45 and 7.71/9.44, respectively. As the results were more than the stoichiometric ratio of Zr/W for ZrW_2O_8 (i.e. 0.5) particles, the formation in core–shell arrangement can be deduced.

Table 4.2 shows also that except in experiment D, c-ZrO_2 formed in all experiments though in small quantities. At ambient pressure ZrO_2 is existent in three polymorphs namely monoclinic, tetragonal and cubic. Baddeleyite type monoclinic phase (P21/c) is the polymorph which is stable at ambient temperature and it is transformed to tetragonal phase (P42/nmc) at 1200°C. Tetragonal phase is stable till 2370°C above which it is transformed to fluorite type cubic structure (Fm3m). Cubic structure is stable up to its melting point [85]. Although monoclinic phase is the stable phase at ambient temperature, it is known that amorphous hydrated $ZrO_2 \cdot nH_2O$ forms a tetragonal phase as a result of dehydration and crystallization at 500°C. This fact is ascribed to the lower specific surface free enthalpy of tetragonal phase ($0.77 j/m^2$) compared to that of monoclinic phase ($1.13 j/m^2$) [86, 87]. Large surface area of precursor nanopowders plays the role of thermodynamic obstacle for transformation from t-ZrO_2 to m-ZrO phase and, as a result, tetragonal phase is maintained. The critical particle size below which the phase transformation is hindered was reported as 60nm [88]. Another important fact is that, in case the diameters of ZrO_2 particles are even smaller, fluorite type cubic structure rather than the tetragonal phase is formed which is as a result of the increase in oxygen vacancies. Higher surface energy of finer particles in this case imposes formation of isotropic cubic phase rather than anisotropic tetragonal phase. The critical size above which cubic phase is transformed to tetragonal phase was reported as 2nm. Such size-induced phase transformation has also reported to form perovskite type cubic structure in which the cubic structure formation was attributed to increase in ionicity,

rather than covalency, by decrease in particle size [88, 89]. Figure 4.12 represents crystallite sizes calculated based on the most intense peak of t-ZrO_2 against the c-ZrO_2/t-ZrO_2 ratio in the shells of particles synthesized in different experiments. When the crystallite size was 15 nm cubic phase in the shell was calculated as approximately 20%. The transformation of c-ZrO_2 to t-ZrO_2 was almost complete when crystallite size increased to 25 nm.

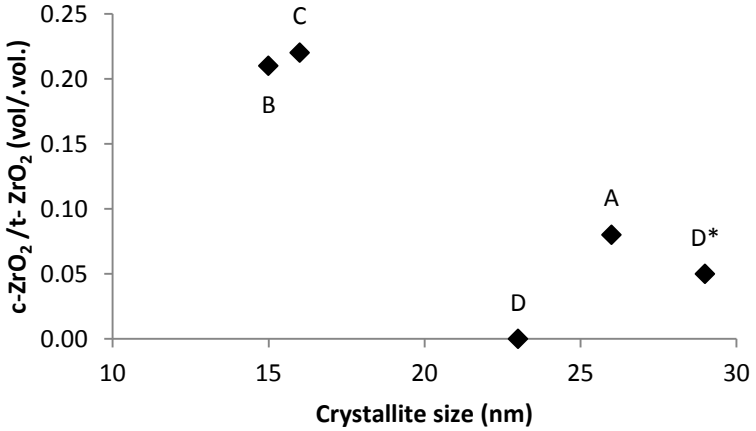

Figure 4.12 Relationship between crystallite size of ZrO_2 and ratio of cubic to tetragonal phases of ZrO_2 in the shells of products.

In precursor level, crystallite size of ZrO_2 and possibly resultant phase mixture are dependent on nucleation and growth rates. A comparison between crystallite size and reaction rate of the experiments shows that the fastest and the slowest precipitation rates (i.e. experiments B and C, respectively) resulted in smaller crystallite sizes with about 20% leftover c-ZrO_2 phase. On the other hand, at intermediate rates (i.e. experiments A, D and D*) the products were of slightly larger sizes and with trace of remnant c-ZrO_2 phase. These facts cannot be justified by using the data presented in this work. Nonetheless, as characteristic of precipitation reactions initiated by urea hydrolysis, it can be claimed that the growth mechanism of the shell was through the agglomeration of the primary crystallites [84]. Derived from this, it can be hypothesized that precursor nucleation could be triggered heterogeneously on the ZrW_2O_8 core particles and/or homogeneously on the bulk of reaction solution which is dependent on the rate of hydroxyl liberation in the solution. Even if precursor nucleated both homogeneously and heterogeneously, nuclei formed homogeneously in the bulk of solution would still have a high affinity towards ones heterogeneously formed on the surfaces of core–shell particles. Considering the abundance of nucleation sites on the solid particles surfaces, precursor particles expected to form homogeneously in the solution would remain relatively small in size before they agglomerate with the particles that already have nucleated heterogeneously on the surface. In such a case, since the stable nuclei size for c-ZrO_2 is known to be small, it would be intuitive to observe relatively small t-ZrO_2 crystallites in the presence of remnant c-ZrO_2. Conditions under which small size nuclei becomes more stable needs further investigation. However, for phase pure t-ZrO_2 shells, intermediate reactions rates can be advised.

Except in experiment A, a trace of m-WO_3 was observed in core–shell particles (as presented in Table 4.2). This is expected in view of the fact that core particles already contained small amounts of m-WO_3 phase in experiments carried out with the mixture of four batches. On the other hand, since γ-ZrW_2O_8 was only existent and, therefore, expected to be detected in the core particles of experiment A, observation of this phase in experiments C and D (and to a smaller extend in D*) should be justified. Cubic phase is the stable phase of ZrW_2O_8 under ambient conditions and start to transform into γ-ZrW_2O_8 at elevated pressures of around 2kbar. The transformation was reported to be completed at approximately 6kbar [41, 46]. As a result of heat treatment at 500°C, along with calcination of thermally expanded shell precursor to ZrO_2, the core of ZrW_2O_8 was contracted. During cooling down, due to its negative CTE the core would need to expand, whereas as a result of positive coefficient of thermal expansion, ZrO_2 on the shell would start to contract simultaneously. It can be speculated that the expansion–contraction during the calcination step induced a pressure on the interface of core and shell which was evidently enough to lead to phase transformation from c-ZrW_2O_8 to γ-ZrW_2O_8 at the interface. Such pressure induced phase transformation was observed on c-ZrW_2O_8 and ZrO_2 particles cold pressed at 750MPa [75]. Owing to the distinct nature of the shell produced, the abovementioned pressure induction is not expected to develop afar from a limited region. The core–shell particles produced under slower precursor reaction conditions exhibited more γ-ZrW_2O_8. Slower reaction rates could have allowed a close pack of crystallites on the interface which would sequentially clarify the comparatively higher quantities of γ-ZrW_2O_8 detected in C and D in comparison with D* and B. This hypothesis would need more direct evidence from comprehensive phase analyses conducted directly on the interface of particles. The proposed mechanism of pressure induced phase transformation is summarized in Figure 4.13.

Figure 4.14(a) and (b) show SEM micrographs of as-synthesized ZrW_2O_8 particles and Figure 4.14(c) and (d) exhibit SEM images of core–shell particles from experiment B. It can be noticed that the shells remained free of crack after heat treatment. This could be explained by the crystallite sizes of shell which remained small even after heat treatment. This may have helped in restricting extend of the interface stresses which could have been relieved to a certain extend due to the phase transformation at the interface as discussed above.

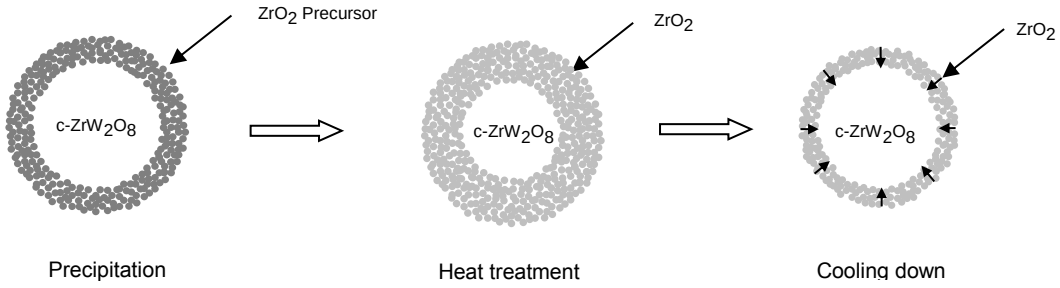

Figure 4.13 Sketch of phase transformations during heat treatment of the core–shell particles. After calcination volume of ZrO_2 will be smaller than that of its precursor.

Zr

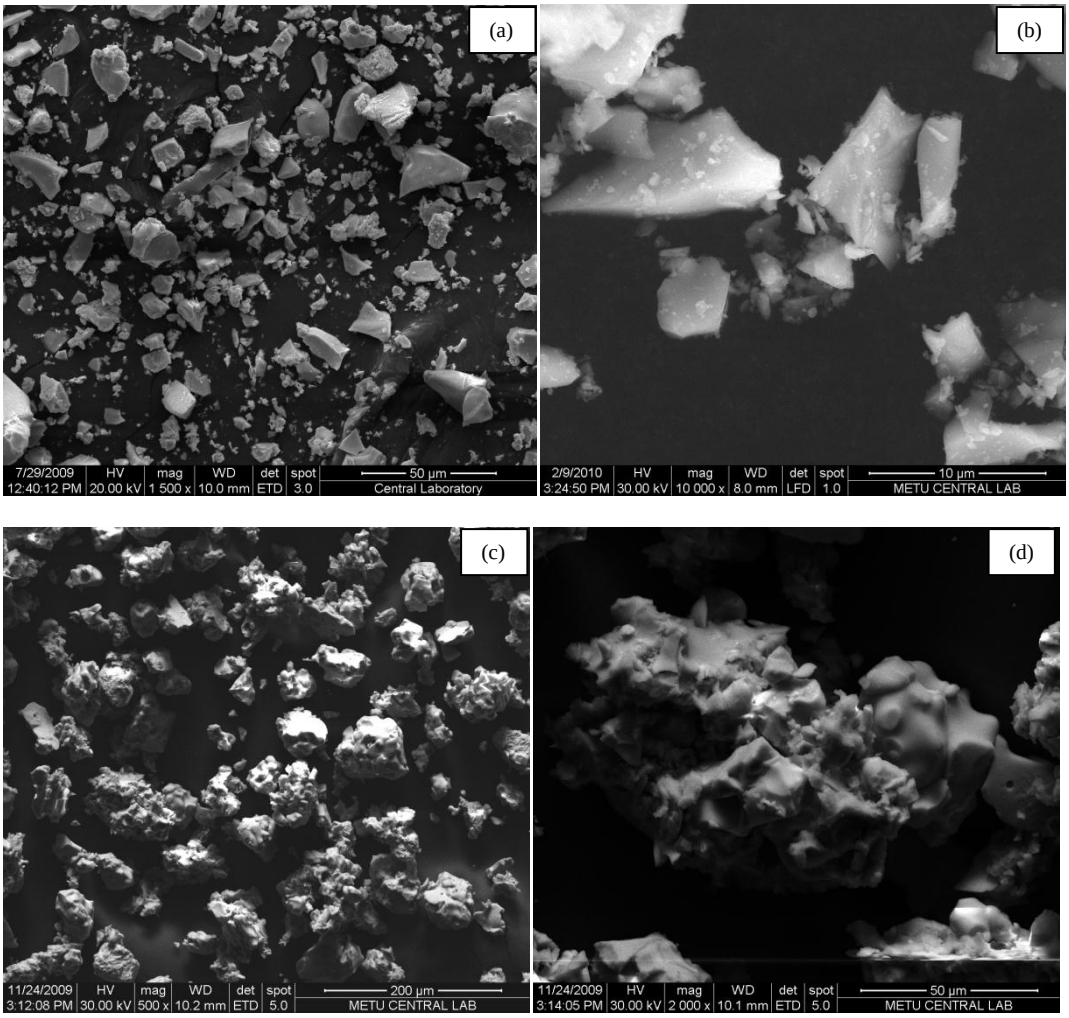

Figure 4.14 (a) and (b) SEM micrographs of as-synthesized ZrW_2O_8 particles and (c) and (d) the images of core–shell particles from experiment B.

CHAPTER 5

CONCLUSIONS

A sol-gel strategy to produce zirconium tungstate with fairly abundant zirconium and tungsten sources, zirconium acetate and tungstic acid respectively, had been proposed and set up in our group which had led to synthesis of a product with purity of 64vol.% [66]. In this study both precursor preparation and heat treatment protocols of this sol-gel strategy were modified to increase the phase purity of the products of the method. Dissolution of tungstic acid in aqueous ammonia solution was challenging step of precursor preparation. The quantity of ammonia which increases the pH of TA mixture above 11 was determined as optimum amount that should be added to the TA mixture to achieve phase pure product. In case of lower pH, use of TA in excess of stoichiometric ratio and centrifugation of undissolved TA was necessary to reach the phase pure product. The optimum temperature for heat treatment was determined as 1180°C. It was also shown that any additional interaction between treated body and crucible, can lead to an impure product. Presence of trace amounts of γ-ZrW_2O_8 in the product was attributed to the cold pressing of calcined powder before sintering a step that was previously believed to be indispensible for the reactive sintering of the oxides mixture.

In the second part of the study, urea hydrolysis method in the presence of zirconium ions was used to precipitate a precursor as shell phase on the ZrW_2O_8 cores particles produced by sol-gel method. Increasing the initial ratio of urea to zirconium ion concentration from 41 to 189 led to decrease in the supersaturation time from 21 to 8 minutes. The precipitation reaction rate exhibited a well-predictable behavior which might be attributed to the dominancy of zirconium ion and hydroxyl interactions in the solutions. Reactions with intermediate rates yielded almost phase pure t-ZrO_2 in the shell. As a result of complete consumption of the metal ion source at a pH value above 6.0 calculation of shell volumes were possible. To crystallize the shell of composite particles, heat treatment at 500°C was used. Based on opposing nature of thermal expansion in ZrW_2O_8 and ZrO_2, a pressure induced phase transformation resulted in formation of γ-ZrW_2O_8 at the interface of core and shell of the composite particles.

CHAPTER 6

RECOMMENDATIONS

Production of ZrW_2O_8 nanoparticles could play a critical role in application of zirconium tungstate in controlled thermal expansion composites:

- Having nanoparticles in the composite structure, micro cracks that can result due to recurring expansion-contraction can be prevented.

- Achieving a higher relative density and, therefore, better mechanical properties of composite can be facilitated if nanoparticles were used in the composite production.

- Production of the nanoparticles paves the way to produce zirconium tungstate nanofibers and core-shell composite fibers.

- Having the nanoparticles in hand one would be able to apply state-of-art sintering methods like spark plasma sintering.

Hence, focusing on low temperature approaches as well as microemulsion strategy production of zirconium tungstate nanoparticles is recommended.

As a second alternative for core-shell configuration precipitation of zirconium tungstate precursor on zirconia particles can be worthy of attempt. Sintering of such composite particles could be possible at temperature as low as 800°C.

REFERENCES

1. J. S. O. Evans, T. A. Mary, T. Vogt, M. A. Subramanian, A. W. Sleight, "Negative Thermal Expansion in ZrW_2O_8 and HfW_2O_8," Chemistry of Materials 8, 2809 (1996).
2. T. A. Mary, J. S. O. Evans, T. Vogt, A. W. Sleight, "Negative Thermal Expansion from 0.3 to 1050 Kelvin in ZrW_2O_8," Science 272, 90 (1996).
3. J. Graham, A. D. Wadsley, J. H. Weymouth, L. S. Williams, "A New Ternary Oxide, ZrW_2O_8," Journal of the American Ceramic Society 42, 570 (1959).
4. M. S. Sutton, J. Talghader, "Zirconium tungstate (ZrW_2O_8)-based micromachined negative thermal-expansion thin films," Journal of Microelectromechanical Systems 13, 688 (2004).
5. K. De Buysser, P. Smet, B. Schoofs, E. Bruneel, D. Poelman, S. Hoste, I. Van Driessche, "Aqueous sol–gel processing of precursor oxides for ZrW_2O_8 synthesis," Journal of Sol-Gel Science and Technology 43, 347 (2007).
6. C. Georgi, H. Kern, "Preparation of zirconium tungstate (ZrW_2O_8) by the amorphous citrate process," Ceramics International 35, 755 (2009).
7. U. Kameswari, A. W. Sleight, J. S. O. Evans, "Rapid synthesis of ZrW_2O_8 and related phases, and structure refinement of $ZrWMoO_8$," International Journal of Inorganic Materials 2, 333 (2000).
8. K. Kanamori, T. Kineri, R. Fukuda, K. Nishio, A. Yasumori, "Preparation and Formation Mechanism of ZrW_2O_8 by SolGel Process," Journal of the American Ceramic Society 91, 3542 (2008).
9. A. P. Wilkinson, C. Lind, S. Pattanaik, "A New Polymorph of ZrW_2O_8 Prepared Using Nonhydrolytic Sol-Gel Chemistry," Chemistry of Materials 11, 101 (1998).
10. X. Yang, X. Cheng, X. Yan, J. Yang, T. Fu, J. Qiu, "Synthesis of ZrO_2/ZrW_2O_8 composites with low thermal expansion," Composites Science and Technology 67, 1167 (2007).
11. C. Closmann, A. W. Sleight, J. C. Haygarth, "Low-Temperature Synthesis of ZrW_2O_8 and Mo-Substituted ZrW_2O_8," Journal of Solid State Chemistry 139, 424 (1998).
12. L. Zhang, J. Y. Howe, Y. Zhang, H. Fong, "Synthesis and Characterization of Zirconium Tungstate Ultra-Thin Fibers," Crystal Growth & Design 9, 667 (2009).
13. J. A. Colin, D. V. Camper, S. D. Gates, M. D. Simon, K. L. Witker, C. Lind, "Zirconium tungstate hydroxide hydrate revisited: Crystallization dependence on halide and hydronium ions," Journal of Solid State Chemistry 180, 3504 (2007).
14. L. C. Kozy, M. N. Tahir, C. Lind, W. Tremel, "Particle size and morphology control of the negative thermal expansion material cubic zirconium tungstate," Journal of Materials Chemistry 19, 2760 (2009).
15. X. Sun, J. Yang, Q. Liu, X. Cheng, "Influence of sodium dodecyl benzene sulfonate (SDBS) on the morphology and negative thermal expansion property of ZrW_2O_8 powders synthesized by hydrothermal method," Journal of Alloys and Compounds 481, 668 (2009).

16. Q. Xing, X. Xing, R. Yu, L. Du, J. Meng, J. Luo, D. Wang, G. Liu, "Single crystal growth of ZrW_2O_8 by hydrothermal route," Journal of Crystal Growth 283, 208 (2005).

17. X. Xing, Q. Xing, R. Yu, J. Meng, J. Chen, G. Liu, "Hydrothermal synthesis of ZrW_2O_8 nanorods," Physica B: Condensed Matter 371, 81 (2006).

18. W. D. J. Callister, Fundamentals of Materials Science and Engineering: An Interactive e . Text, John Wiley and Sons, ed. 5, 2000, pp. 552.

19. A. K. Jonscher, Dielectric Relaxation in Solids, Chelsea Dielectrics Press, London, 1983, pp. 396.

20. G. Shirane, S. Hoshino, "On the Phase Transition in Lead Titanate," Journal of the Physical Society of Japan 6, 265 (1950).

21. G. Shirane, A. Takeda, "Phase Transitions in Solid Solutions of $PbZrO_3$ and $PbTiO_3$ (I) Small Concentrations of $PbTiO_3$," Journal of the Physical Society of Japan 7, 5 (1951).

22. A. W. Sleight, "Thermal contraction," Endeavour 19, 64 (1995).

23. V. Heine, P. R. L. Welche, M. T. Dove, "Geometrical Origin and Theory of Negative Thermal Expansion in Framework Structures," Journal of the American Ceramic Society 82, 1793 (1999).

24. K. D. Hammonds, M. T. Dove, A. P. Giddy, V. Heine, B. Winkler, "Rigid-unit phonon modes and structural phase transitions in framework silicates," American Mineralogist 81, 1057 (1996).

25. A. W. Sleight, "Isotropic Negative Thermal Expansion ", Annual Review of Materials Science 28, 29 (1998).

26. J. Z. Tao, A. W. Sleight, "The role of rigid unit modes in negative thermal expansion," Journal of Solid State Chemistry 173, 442 (2003).

27. J. Z. Tao, A. W. Sleight, "Very low thermal expansion in TaO_2F," Journal of Solid State Chemistry 173, 45 (2003).

28. M. P. Attfield, A. W. Sleight, "Exceptional Negative Thermal Expansion in $AlPO_4$-17," Chemistry of Materials 10, 2013 (1998).

29. T. G. Amos, A. Yokochi, A. W. Sleight, "Phase Transition and Negative Thermal Expansion in Tetragonal $NbOPO_4$," Journal of Solid State Chemistry 141, 303 (1998).

30. V. Korthuis, N. Khosrovani, A. W. Sleight, N. Roberts, R. Dupree, W. W. Warren, Jr., "Negative Thermal Expansion and Phase Transitions in the $ZrV_{2-x}P_xO_7$ Series," Chemistry of Materials 7, 412 (1995).

31. J. S. O. Evans, T. A. Mary, A. W. Sleight, "Negative Thermal Expansion in $Sc_2(WO_4)_3$," Journal of Solid State Chemistry 137, 148 (1998).

32. P. M. Forster, A. W. Sleight, "Negative thermal expansion in $Y_2W_3O_{12}$," International Journal of Inorganic Materials 1, 123 (1999).

33. P. M. Forster, A. Yokochi, A. W. Sleight, "Enhanced Negative Thermal Expansion in $Lu_2W_3O_{12}$," Journal of Solid State Chemistry 140, 157 (1998).

34. A. K. A. Pryde, K. D. Hammonds, M. T. Dove, V. Heine, J. D. Gale, M. C. Warren, "Origin of the negative thermal expansion in and ZrW_2O_8 and ZrV_2O_7," Journal of Physics: Condensed Matter 8, 10973 (1996).

35. M. Auray, M. Quarton, M. Leblanc, "Zirconium Tungstate," Acta Crystallographica C 51, 2210 (1995).

36. in Wikipedia the Free Encyclopedia. (2007), http://en.wikipedia.org/wiki/Zirconium_tungstate.

37. R. D. Shannon, "Revised effective ionic radii and systematic studies of interatomic distances in halides and chalcogenides," Acta Crystallographica A 32, 751 (1976).

38. P. M. Woodward, A. W. Sleight, T. Vogt, "Structure refinement of triclinic tungsten trioxide," Journal of Physics and Chemistry of Solids 56, 1305 (1995).

39. C. D. Meyer, dissertation, "Perspectives in the chemistry of negative thermal expansion," Ghent University (2004).

40. Y. Yamamura, T. Tsuji, K. Saito, M. Sorai, "Heat capacity and order-disorder phase transition in negative thermal expansion compound ZrW_2O_8," The Journal of Chemical Thermodynamics 36, 525 (2004).

41. J. S. O. Evans, Z. Hu, J. D. Jorgensen, D. N. Argyriou, S. Short, A. W. Sleight, "Compressibility, Phase Transitions, and Oxygen Migration in Zirconium Tungstate, ZrW_2O_8," Science 275, 61 (1997).

42. J. D. Jorgensen, Z. Hu, S. Teslic, D. N. Argyriou, S. Short, J. S. O. Evans, A. W. Sleight, "Pressure-induced cubic-to-orthorhombic phase transition in ZrW_2O_8," Physical Review B 59, 215 (1999).

43. J. S. O. Evans, J. D. Jorgensen, S. Short, W. I. F. David, R. M. Ibberson, A. W. Sleight, "Thermal expansion in the orthorhombic gamma phase of ZrW_2O_8," Physical Review B 60, 14643 (1999).

44. G. D. Barrera, et al., "Negative thermal expansion," Journal of Physics: Condensed Matter 17, R217 (2005).

45. A. K. Arora, et al., "The pressure-amorphized state in zirconium tungstate: a precursor to decomposition," Journal of Physics: Condensed Matter 16, 1025 (2004).

46. J. M. Gallardo-Amores, U. Amador, E. Morán, M. Á. Alario-Franco, "XRD study of ZrW_2O_8 versus temperature and pressure," International Journal of Inorganic Materials 2, 123 (2000).

47. C. A. Perottoni, J. A. Jornada, nbsp, H., da, "Pressure-Induced Amorphization and Negative Thermal Expansion in ZrW_2O_8," Science 280, 886 (1998).

48. A. Grzechnik, W. A. Crichton, K. Syassen, P. Adler, M. Mezouar, "A New Polymorph of ZrW_2O_8 Synthesized at High Pressures and High Temperatures," Chemistry of Materials 13, 4255 (2001).

49. L. D. Noailles, H. h. Peng, J. Starkovich, B. Dunn, "Thermal Expansion and Phase Formation of ZrW_2O_8 Aerogels," Chemistry of Materials 16, 1252 (2004).

50. J.-i. Tani, H. Kido, "Precursor effects on ZrW_2O_8 formation kinetics," Ceramics International 34, 1533 (2008).

51. G. R. Kowach, "Growth of single crystals of ZrW_2O_8," Journal of Crystal Growth 212, 167 (2000).

52. J. C. Chen, G. C. Huang, C. Hu, J. P. Weng, "Synthesis of negative-thermal-expansion ZrW_2O_8 substrates," Scripta Materialia 49, 261 (2003).

53. E. J. Liang, T. A. Wu, B. Yuan, M. J. Chao, W. F. Zhang, "Synthesis, microstructure and phase control of zirconium tungstate with a CO_2 laser," Journal of Physics D: Applied Physics 40, 3219 (2007).

54. C. Martinek, F. A. Hummel, "Linear Thermal Expansion of Three Tungstates," Journal of the American Ceramic Society 51, 227 (1968).

55. C. A. Martinek, F. A. HUMMEL, "Subsolidus Equilibria in the System ZrO_2-WO_3-P_2O_5," Journal of the American Ceramic Society 53, 159 (1970).

56. S. Nishiyama, T. Hayashi, T. Hattori, "Synthesis of ZrW_2O_8 by quick cooling and measurement of negative thermal expansion of the sintered bodies," Journal of Alloys and Compounds 417, 187 (2006).

57. M. N. Mancheva, R. S. Iordanova, Y. B. Dimitriev, K. P. Petrov, G. V. Avdeev, "Direct Synthesis of Metastable Nanocrystalline ZrW_2O_8 by a Melt-Quenching Method," The Journal of Physical Chemistry C 111, 14945 (2007).

58. K. Kanamori, T. Kineri, R. Fukuda, K. Nishio, M. Hashimoto, H. Mae, "Spark Plasma Sintering of SolGel Derived Amorphous ZrW_2O_8 Nanopowder," Journal of the American Ceramic Society 92, 32 (2009).

59. X. H. Yan, X. N. Cheng, X. B. Yang, C. H. Zhang, "Combustion synthesis of ZrW_2O_8 and preparation of its composite with near zero thermal expansion," Key Engineering Materials 353-358, 1235 (2007).

60. L. M. Sullivan, C. M. Lukehart, "Zirconium Tungstate (ZrW_2O_8)/Polyimide Nanocomposites Exhibiting Reduced Coefficient of Thermal Expansion," Chemistry of Materials 17, 2136 (2005).

61. I. Vural, "Synthesis of Zirconium Tngstate and Its Use in Composites with Tunable Thermal Expansion Coefficient," Middle East Technical University (2011).

62. K. De Buysser, I. Van Driessche, J. Schaubroeck, S. Hoste, "EDTA assisted sol–gel synthesis of ZrW_2O_8," Journal of Sol-Gel Science and Technology 46, 133 (2008).

63. A. W. Sleight, M. A. Thundathil, J. S. O. Evans, "Negative thermal expansion materials," 5514360 A, (1996).

64. Tzeng, D. Liang, H. C. Chang, J. C. Wu, "Method for making negative thermal expansion material zirconium tungstate," US 2005/0101133 A1, (2005).

65. C. Lind, A. P. Wilkinson, "Seeding and the Non-Hydrolytic Sol-Gel Synthesis of ZrW_2O_8 and $ZrMo_2O_8$," Journal of Sol-Gel Science and Technology 25, 51 (2002).

66. B. Özerciyes, "A Novel Precursor for Synthesis of Zirconium Tungstate and Preliminary Studies for Nanofiber Production," Middle East Technical University (2009).

67. I. Vural, N. Khazeni, B. Mavis, G. Gunduz, U. Colak, paper presented at the CIMTEC, Montecatini, Italy, 2010.

68. H. Holzer, D. C. Dunand, "Phase transformation and thermal expansion of Cu/ZrW_2O_8 metal matrix composites," Journal of Materials Research 14, 780 (1999).

69. C. Verdon, D. C. Dunand, "High-temperature reactivity in the ZrW_2O_8-Cu system," Scripta Materialia 36, 1075 (1997).

70. S. Yilmaz, "Thermal mismatch stress development in Cu-ZrW_2O_8 composite investigated by synchrotron X-ray diffraction," Composites Science and Technology 62, 1835 (2002).

71. A. Matsumoto, K. Kobayashi, T. Nishio, K. Ozaki, "Fabrication and Thermal Expansion of Al-ZrW_2O_8 Composites by Pulse Current Sintering Process," Materials Science Forum Volumes 426 - 432, 2279 (2003).

72. J.-i. Tani, H. Kimura, K. Hirota, H. Kido, "Thermal expansion and mechanical properties of phenolic resin/ZrW_2O_8 composites," Journal of Applied Polymer Science 106, 3343 (2007).

73. K. Kanamori, T. Kineri, R. Fukuda, T. Kawano, K. Nishio, "Low-temperature sintering of ZrW_2O_8–SiO_2 by spark plasma sintering," Journal of Materials Science 44, 855 (2009).

74. K. de Buysser, P. Lommens, C. de Meyer, E. Bruneel, S. Hoste, I. Van Driessche, "ZrO_2-ZrW_2O_8 composites with tailor-made thermal expansion," Ceramics-Silikaty 48, 139 (2004).

75. P. Lommens, C. De Meyer, E. Bruneel, K. De Buysser, I. Van Driessche, S. Hoste, "Synthesis and thermal expansion of ZrO_2/ZrW_2O_8 composites," Journal of the European Ceramic Society 25, 3605 (2005).

76. E. Niwa, S. Wakamiko, T. Ichikawa, S. Wang, T. Hashimoto, K. Takahashi, Y. Morito, "Preparation of Dense ZrO_2/ZrW_2O_8 Cosintered Ceramics with Controlled Thermal Expansion Coefficients," Journal of the Ceramic Society of Japan 112, 271 (2004).

77. L. Sun, P. Kwon, "ZrW_2O_8/ZrO_2 composites by in situ synthesis of ZrO_2 + WO_3: Processing, coefficient of thermal expansion, and theoretical model prediction," Materials Science and Engineering: A 527, 93 (2009).

78. X. Yang, J. Xu, H. Li, X. Cheng, X. Yan, "In Situ Synthesis of ZrO_2/ZrW_2O_8 Composites With Near-Zero Thermal Expansion," Journal of the American Ceramic Society 90, 1953 (2007).

79. F. A. Forward, Vizsolyi, Andrew I., "Process for the production of tungstic acid," 3193347, (1965).

80. P. Patnaik, Handbook of Inorganic Chemicals, McGraw-Hill, 2003, pp. 953.

81. A. P. Baker, S. N. B. Hodgson, M. J. Edirisinghe, "Production of tungsten oxide coatings, via sol-gel processing of tungsten anion solutions," Surface and Coatings Technology 153, 184 (2002).

82. R. J. Lewis, Sr., Hawley's Condensed Chemical Dictionary (15th Edition), John Wiley & Sons, 2007, pp. 1351.

83. R. J. Lewis, Sr., Hawley's Condensed Chemical Dictionary (14th Edition), John Wiley & Sons, 2002.

84. B. Mavis, M. Akinc, "Kinetics of Urea Decomposition in the Presence of Transition Metal Ions: Ni2+," Journal of the American Ceramic Society 89, 471 (2006).

85. M. Trubelja, D. Potter, J. Helble, "Effect of process conditions on phase mixtures of sol–gel-synthesized nanoscale orthorhombic, tetragonal, and monoclinic zirconia," Journal of Materials Science 45, 4480 (2010).

86. J. Liang, X. Jiang, G. Liu, Z. Deng, J. Zhuang, F. Li, Y. Li, "Characterization and synthesis of pure ZrO2 nanopowders via sonochemical method," Materials Research Bulletin 38, 161 (2003).

87. M. M. Rashad, H. M. Baioumy, "Effect of thermal treatment on the crystal structure and morphology of zirconia nanopowders produced by three different routes," Journal of Materials Processing Technology 195, 178 (2008).

88. S. Tsunekawa, S. Ito, Y. Kawazoe, J. T. Wang, "Critical Size of the Phase Transition from Cubic to Tetragonal in Pure Zirconia Nanoparticles," Nano Letters 3, 871 (2003).

89. S. Roy, J. Ghose, "Synthesis of stable nanocrystalline cubic zirconia," Materials Research Bulletin 35, 1195 (2000).

APPENDIX A

XRD STANDARD PEAKS

Standard peaks of different phases of ZrW_2O_8, $ZrW_2O_7(OH)_2 \cdot 2(H_2O)$, ZrO_2 and WO_3 appeared in synthesis of ZrW_2O_8 which are extracted from their JCPDS carts are provided in this appendix. XRD patterns of γ-ZrW_2O_8 are created by CaRIne Crystallography version 3.1 software details of which can be found in Appendix B. Intensities of the peaks are normalized to 100 and the peaks with intensities below 10 were eliminated.

Table A.1 Standard XRD pattern of different phases of ZrW_2O_8.

Tetragonal ZrW_2O_8 (JCPDS #: 31-1500)

2θ (°)	Intensity (a.u.)
20.017	60
26.996	100
32.568	10
33.795	20
35.624	100
38.488	60
40.679	40
43.757	100
47.619	60
52.162	60
53.476	100
55.583	60
62.024	40
62.865	60
67.800	100

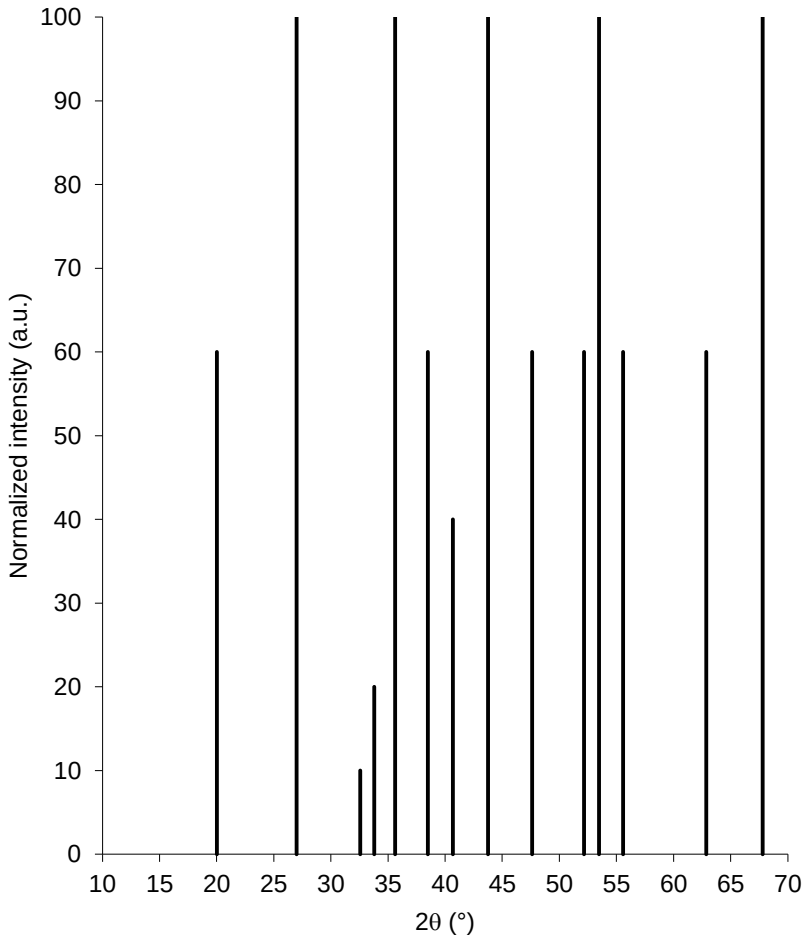

Table A.1 Continued.

Cubic ZrW_2O_8 (JCPDS #: 50-1868)	
2θ (°)	Intensity (a.u.)
16.695	12
19.295	14
21.569	100
23.662	90
27.443	25
29.183	10
30.724	18
32.318	30
35.193	25
36.680	35
40.639	10
45.391	20
48.748	20
50.121	8
50.838	16
51.922	25
53.933	18
56.908	14

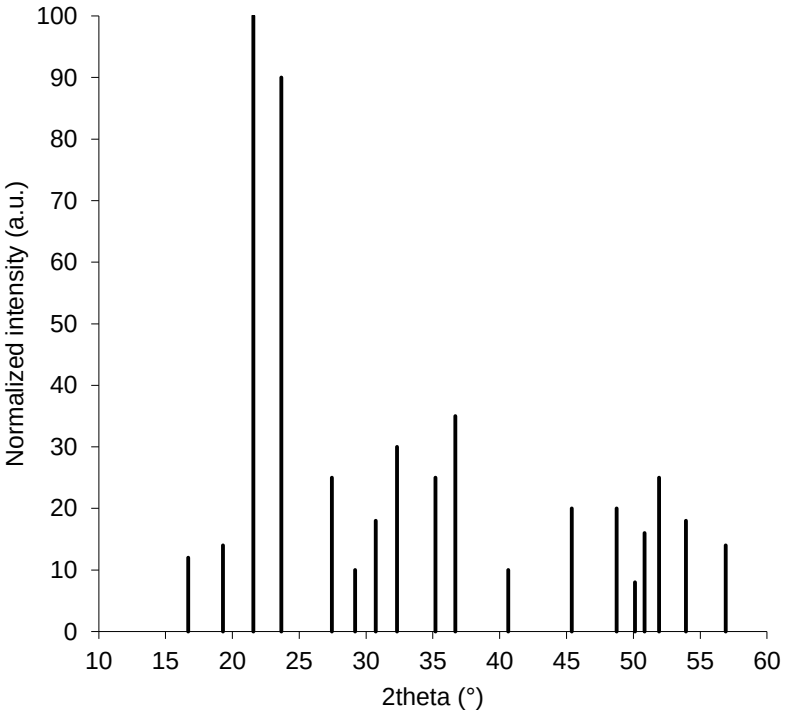

Orthorhombic ZrW_2O_8 (from CaRIne)	
2θ (°)	Intensity (a.u.)
10.440	16
13.960	13
19.700	19
19.890	10
21.990	97
22.030	100
22.230	62
24.130	75
24.200	54
24.320	51
28.050	10
28.250	22
29.790	24
32.820	29
32.970	25
33.210	14
35.770	13
37.210	14

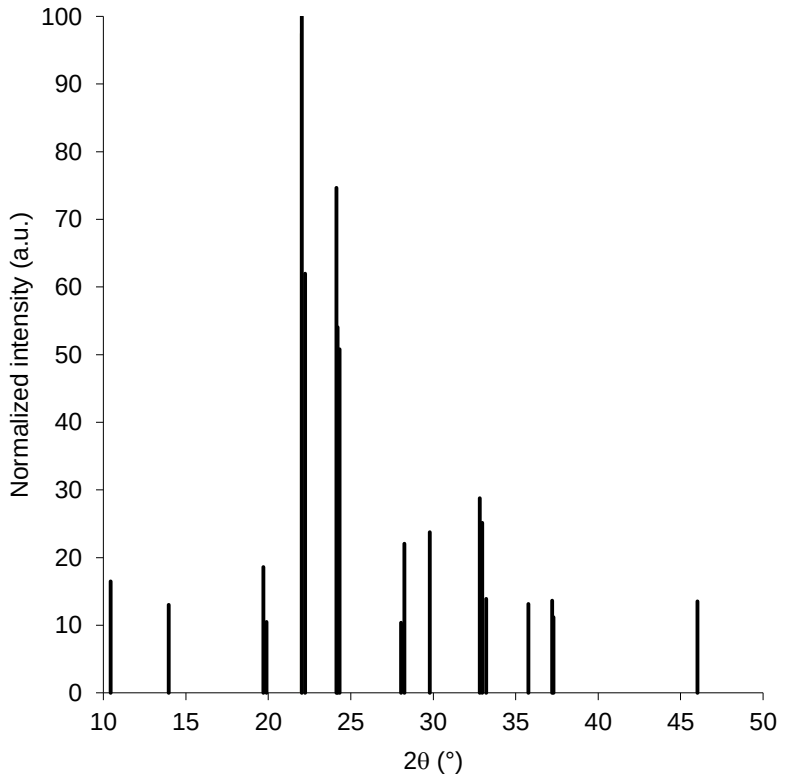

Table A.2 Standard XRD pattern of $ZrW_2O_7(OH)_2 \cdot 2(H_2O)$.

Tetragonal $ZrW_2O_7(OH)_2 \cdot 2(H_2O)$ (JCPDS#: 28-1500)	
2θ (°)	Intensity (a.u.)
15.451	85
17.905	12
20.984	100
24.571	95
28.493	85
34.439	25
36.236	25
38.016	17
46.358	13
47.621	25
50.493	10
52.649	10
56.515	10

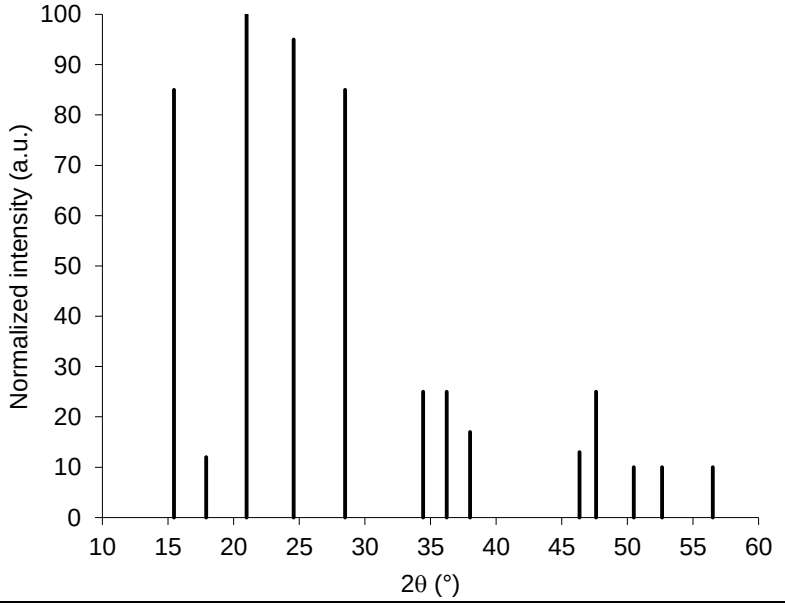

Table A.3 Standard XRD pattern of WO_3.

Monoclinic WO_3 (JCPDS#: 43-1035)	
2θ (°)	Intensity (a.u.)
23.119	100
23.586	97
24.380	99
26.595	19
28.615	16
28.937	17
33.266	39
33.575	27
34.155	62
41.443	14
41.906	14
49.948	24
50.341	13
50.742	12
53.485	12
55.957	18
56.109	15

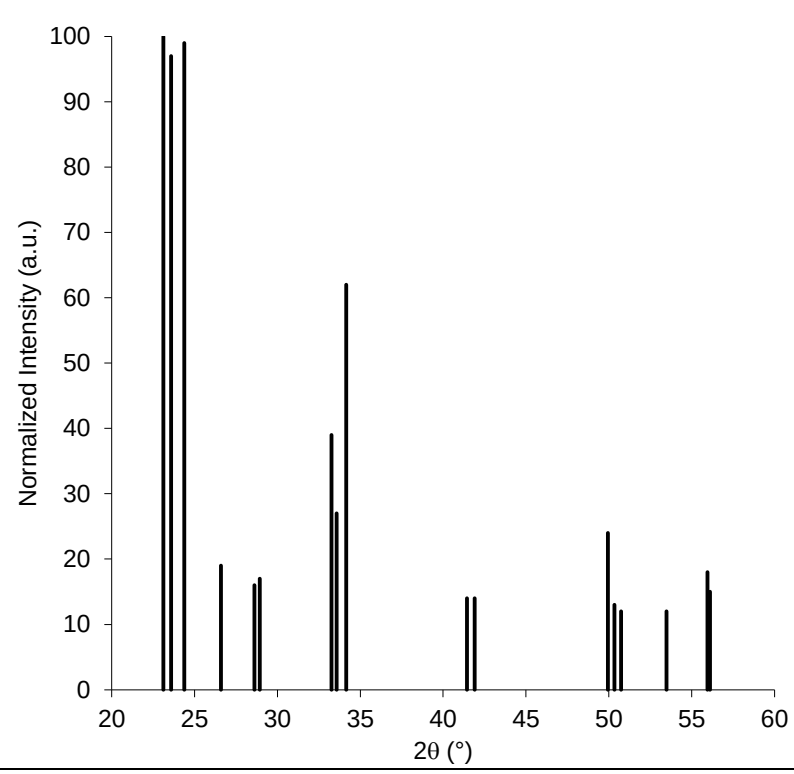

Table A.4 Standard XRD pattern of different phases of ZrO_2.

Cubic ZrO_2 (JCPDS#: 27-997)

2θ (°)	Intensity (a.u.)
30.509	100
35.193	25
50.686	50
60.337	20

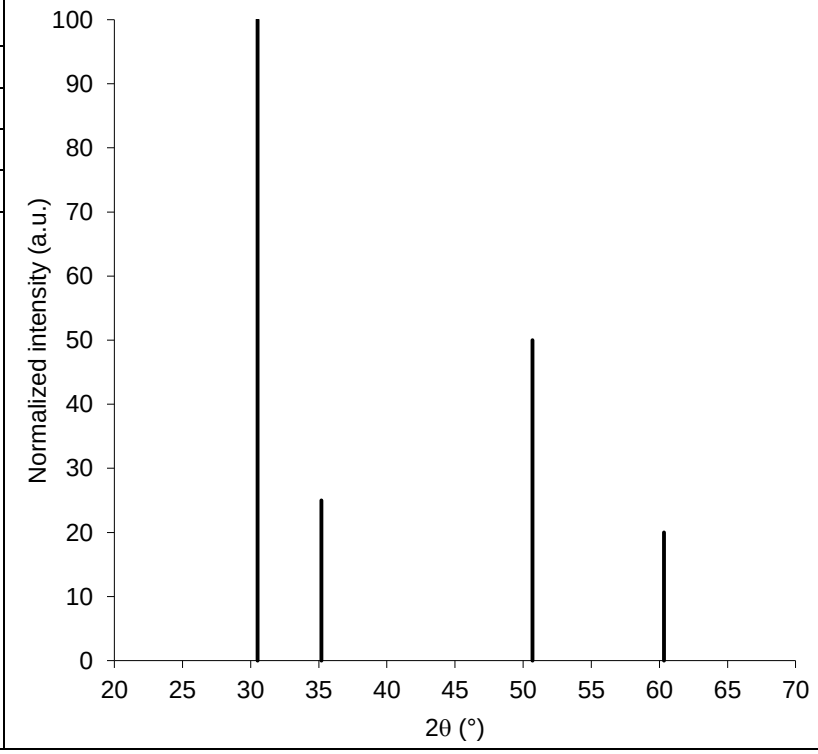

Monoclinic ZrO_2 (JCPDS#: 37-1484)

2θ (°)	Intensity (a.u.)
24.048	14
24.441	10
28.175	100
31.468	68
34.160	21
34.383	11
35.309	13
40.725	12
49.266	18
50.116	22
50.559	13
54.104	11
55.270	11
55.400	11

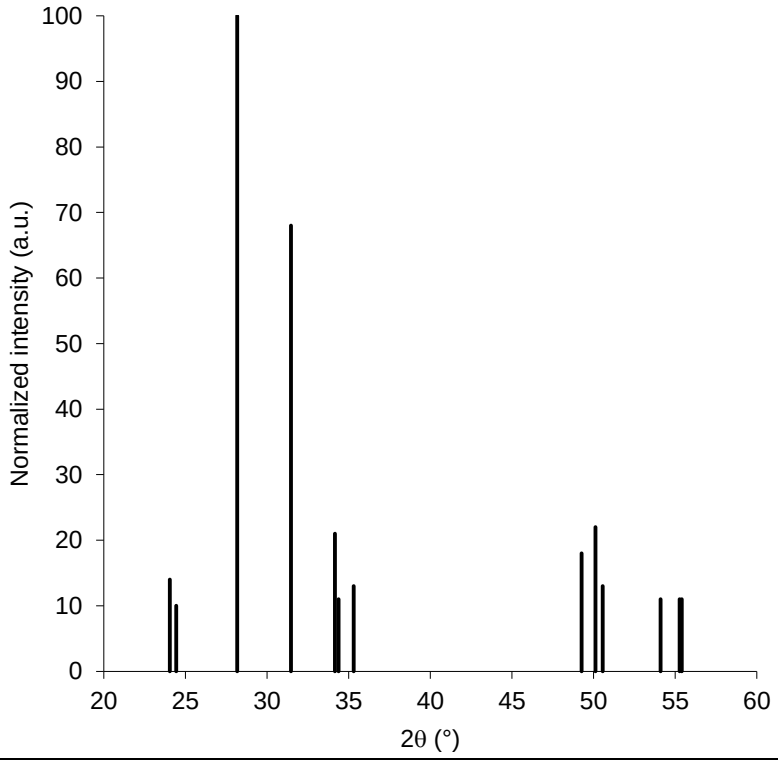

Table A.4 Continued.

Tetragonal ZrO_2 (JCPDS#: 17-923)	
2θ (°)	Intensity (a.u.)
30.166	100
34.465	18
35.306	25
49.783	65
50.371	35
58.556	25
59.722	45
62.116	12
80.672	12

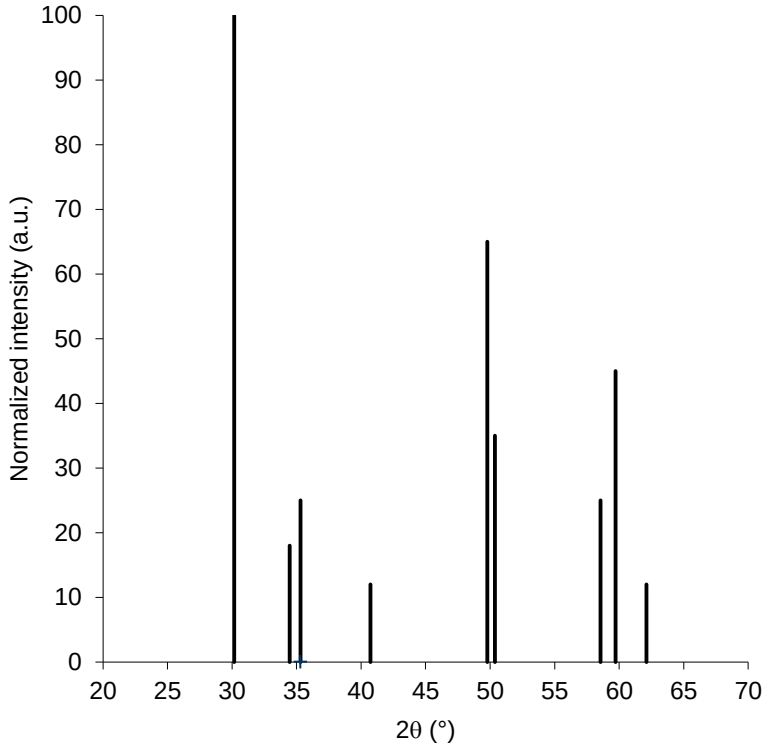

APPENDIX B

CREATION OF XRD PEAKS

Having lattice parameters and position of atoms within unit cell, XRD spectrum of a crystal structure can be created. CaRIne Crystallography version 3.1 is software capable of creating XRD pattern of crystalline materials. As an example creation of standard peaks of orthorhombic phase of γ-ZrW_2O_8 this software has been described.

Step 1: Creation of unit cell

Pushing "Ctrl+0" (or from menu bar pushing Cell→ Creation / List) will open "Cell Creation / Cell List" window. Different parts of the window are illustrated in Figure B.1.

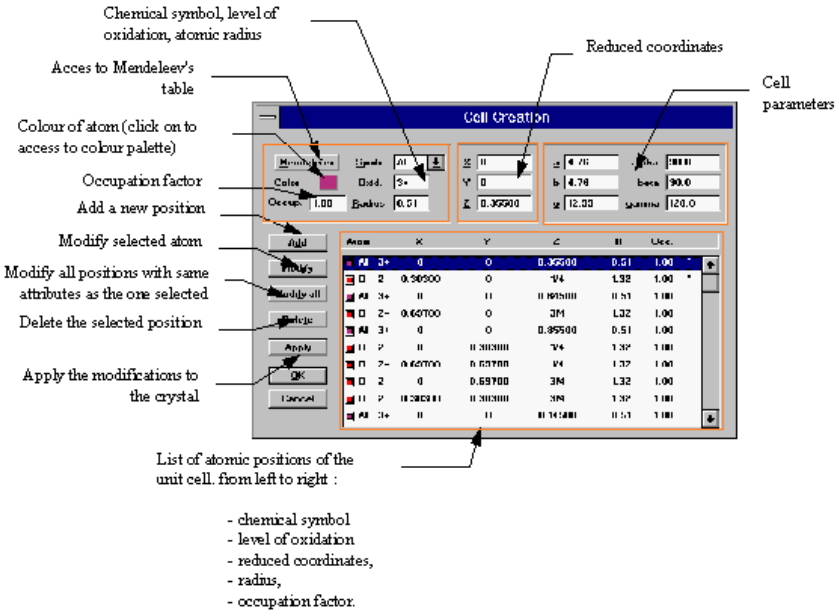

Figure B.1 Different parts of cell creation window.

First of all, lattice parameters of γ-ZrW_2O_8 are entered in "Cell Parameters" fields. Second, "Mendeleev" button is pushed to open elements table from which the atoms of crystal structure and their level of oxidation and a color for each atom are chosen. Atomic radius will automatically appear in the corresponding field. The occupation factor enables a percentage of vacancies to be given and should be between 0 and 1. Finally, atomic positions are entered in "Reduced Coordinates" fields and "Add" button is pushed for each atom by which the atomic positions are listed in a table. When the table is completed, "OK" button is pushed and, consequently, the graphical structure of the crystal will appear in a new window. For γ-ZrW_2O_8, the level of oxidations for Zr, W and O are +4, +6 and -2, respectively. The reduced atomic positions of the crystal structure are entered from Table 2.5. The atom list window and created graphical structure of γ-ZrW_2O_8 are shown in Figure B.2.

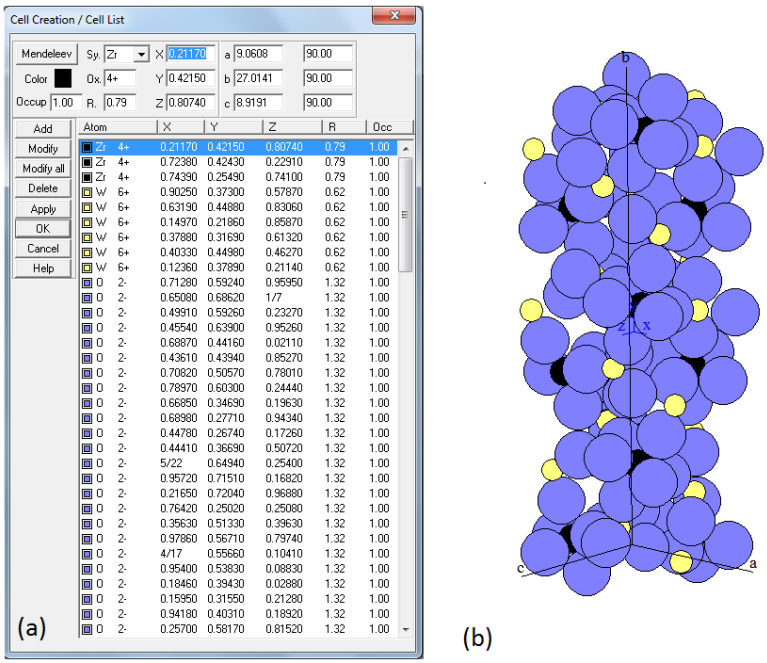

Figure B.2 (a) Cell creation window and (b) crystal structure of γ-ZrW_2O_8.

Step 2: Creation of XRD pattern:

Choosing "Creation XRD" from (Specials → XRD) menu list is led to opening of a dialogue box which is shown in Figure B.3. Different parameters of the analysis can be set up in the dialogue box:

- The wavelength of the X-Rays
- The minimum and maximum Bragg angles
- The temperature factor[1]
- In the case of existence of associated lattices to the current crystal, these lattices appear in the "Mixture" box

As radiation wavelength used for all XRD analyses of this work were λ = 0.154 nm (CuKα type), "Cu 1.540562" was chosen from the list to create XRD pattern of γ-ZrW_2O_8. Temperature factor was adopted as 1. By pushing "OK" button XRD pattern is plotted in a new window which is shown in Figure B.4. The software is also capable of exporting the data table associated with XRD pattern which is tabulated in Table B.1.

[1] The atomic vibrations in a crystal result in an angle dependent effect on the intensities of diffracted peak. By increase in an atomic vibration, i.e. by increase in temperature, the scattering power decreases as a result of spreading of the scattering power of the atom. As an approximation it is assumed that atoms vibrate equally.

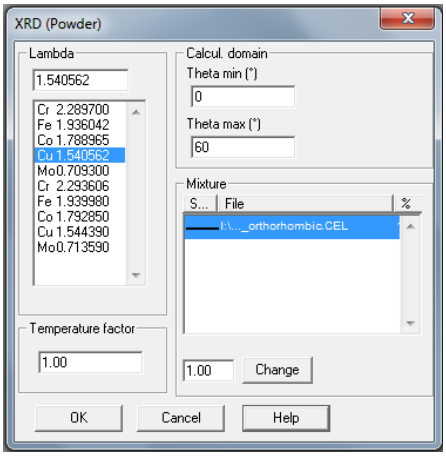

Figure B.3 Dialogue box creation of XRD pattern.

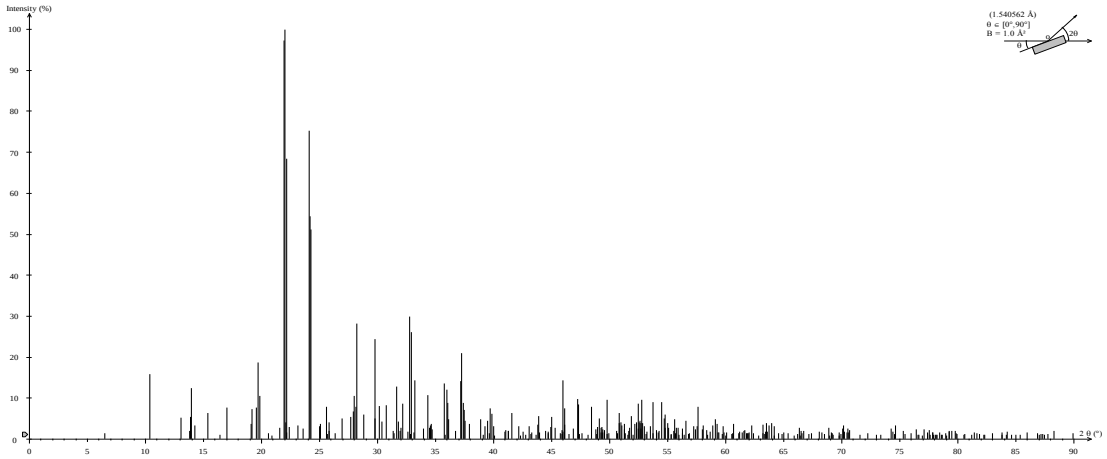

Figure B.4 XRD pattern of γ-ZrW_2O_8.

Table B.1 Data table associated with XRD pattern of γ-ZrW_2O_8.

(hkl)	2θ	Intensity	(hkl)	2θ	Intensity	(hkl)	2θ	Intensity
(0 2 0)	6.54	1.57	(1 4 0)	16.36	0.94	(0 2 2)	20.96	1.02
(1 1 0)	10.29	0.08	(0 4 1)	16.45	1.12	(1 5 1)	21.57	2.93
(0 1 1)	10.44	15.91	(1 3 1)	17.06	7.79	(2 3 0)	21.94	0.06
(1 2 0)	11.75	0.39	(1 5 0)	19.11	0.90	(2 -3 0)	21.94	0.06
(0 2 1)	11.88	0.13	(1 4 1)	19.16	3.75	(2 0 1)	21.99	97.33
(0 2 -1)	11.88	0.13	(0 5 1)	19.19	7.43	(1 6 0)	22.03	100.00
(0 4 0)	13.1	5.36	(2 0 0)	19.58	7.80	(0 6 1)	22.1	4.22
(1 3 0)	13.85	2.09	(0 6 0)	19.7	18.71	(1 0 2)	22.2	1.63
(1 0 1)	13.92	5.56	(2 1 0)	19.85	0.92	(0 3 2)	22.23	61.94
(0 3 1)	13.96	12.56	(0 0 2)	19.89	10.55	(2 1 1)	22.23	6.49

Table B.1 Continued.

(hkl)	2θ	Intensity	(hkl)	2θ	Intensity	(hkl)	2θ	Intensity
(1 1 1)	14.3	3.39	(3 1 1)	31.42	0.78	(2 1 3)	36.26	0.26
(1 2 1)	15.39	6.53	(0 9 1)	31.42	0.65	(3 2 2)	36.51	0.23
(2 2 1)	22.96	0.15	(0 1 2)	20.16	0.07	(2 7 2)	36.6	0.27
(1 2 2)	23.17	3.42	(2 2 0)	20.66	1.52	(2 2 3)	36.73	1.99
(2 4 0)	23.63	2.69	(1 0 3)	31.65	3.42	(1 1 2)	22.44	3.12
(0 4 2)	23.89	0.04	(0 3 3)	31.67	9.56	(2 2 -1)	22.96	0.15
(2 3 1)	24.13	75.38	(1 1 3)	31.82	4.35	(3 6 1)	37.21	14.27
(1 6 1)	24.2	54.51	(3 2 1)	31.95	2.05	(3 3 2)	37.29	9.29
(1 3 2)	24.32	51.19	(2 7 1)	32.05	2.93	(2 9 1)	37.29	11.72
(1 7 0)	25.06	3.21	(1 7 2)	32.2	8.76	(1 9 2)	37.42	8.97
(0 7 1)	25.12	3.79	(1 2 3)	32.35	0.83	(2 3 3)	37.51	7.13
(2 5 0)	25.64	7.91	(3 4 0)	32.45	0.45	(1 6 3)	37.56	4.51
(2 4 1)	25.68	1.28	(2 5 2)	32.66	1.85	(3 7 0)	37.79	0.10
(1 4 2)	25.86	2.02	(3 3 1)	32.82	30.00	(1 11 0)	37.93	3.79
(0 5 2)	25.88	4.16	(0 4 3)	32.89	1.38	(0 11 1)	37.97	0.02
(0 8 0)	26.37	1.53	(1 9 1)	32.97	26.19	(0 7 3)	38.18	0.02
(1 7 1)	27.01	5.16	(2 8 0)	33.06	0.12	(3 4 2)	38.35	0.18
(2 5 1)	27.55	0.47	(0 10 0)	33.13	1.69	(2 4 3)	38.56	0.74
(1 5 2)	27.72	5.55	(1 3 3)	33.21	14.50	(2 10 0)	38.78	0.03
(2 6 0)	27.91	6.85	(0 8 2)	33.25	0.55	(2 8 2)	38.88	4.96
(2 0 2)	28.05	10.72	(3 5 0)	33.98	0.50	(0 10 2)	38.95	0.21
(0 6 2)	28.14	8.06	(3 4 1)	34.01	2.67	(3 7 1)	39.17	1.11
(1 8 0)	28.18	0.95	(1 4 3)	34.38	3.00	(1 11 1)	39.3	3.29
(0 8 1)	28.24	5.75	(0 5 3)	34.4	7.85	(1 7 3)	39.5	4.62
(2 1 2)	28.25	22.58	(2 6 2)	34.52	2.86	(3 5 2)	39.68	1.44
(2 2 2)	28.83	5.98	(2 8 1)	34.59	2.85	(4 0 0)	39.76	7.52
(2 6 -1)	29.69	0.03	(1 10 0)	34.62	3.43	(2 5 3)	39.89	1.92
(2 6 1)	29.69	0.03	(0 10 1)	34.67	3.72	(4 1 0)	39.9	4.43
(3 1 0)	29.74	0.72	(1 8 2)	34.73	2.40	(3 8 0)	40.02	0.01
(2 3 2)	29.79	24.45	(3 5 1)	35.48	0.11	(0 12 0)	40.02	3.25
(1 6 2)	29.85	5.21	(3 6 0)	35.77	13.75	(2 10 1)	40.12	1.00
(1 8 1)	29.94	0.83	(1 5 3)	35.84	1.10	(1 10 2)	40.25	0.14
(0 1 3)	30.22	8.07	(2 9 0)	35.86	0.01	(4 2 0)	40.34	0.00
(3 2 0)	30.3	0.47	(2 -9 0)	35.86	0.01	(0 8 3)	40.39	0.24
(2 7 0)	30.4	4.41	(3 0 2)	35.88	0.02	(0 0 4)	40.42	0.01
(0 7 2)	30.61	0.91	(3 0 -2)	35.88	0.02	(0 1 4)	40.56	0.21
(0 2 3)	30.77	8.32	(3 1 2)	36.04	2.50	(0 2 4)	40.99	1.94
(2 4 2)	31.07	0.03	(0 9 2)	36.04	9.62	(4 3 0)	41.05	2.19
(3 3 0)	31.21	0.01	(1 10 1)	36.1	0.85	(4 0 1)	41.08	0.01
(3 0 1)	31.24	0.72	(2 0 3)	36.11	8.09	(4 1 1)	41.22	0.57
(1 9 0)	31.37	2.16	(0 6 3)	36.18	4.91	(3 6 2)	41.26	0.23

Table B.1 Continued.

(hkl)	2θ	Intensity	(hkl)	2θ	Intensity	(hkl)	2θ	Intensity
(1 12 0)	41.29	2.15	(2 12 0)	44.93	3.05	(0 13 2)	48.28	0.54
(3 8 1)	41.33	0.67	(4 1 2)	44.97	0.15	(4 8 0)	48.34	0.33
(0 12 1)	41.33	0.14	(3 10 0)	44.98	0.25	(2 5 4)	48.48	7.93
(2 9 2)	41.34	1.36	(1 5 4)	45.07	0.08	(3 11 1)	48.83	2.39
(2 6 3)	41.46	0.47	(3 8 2)	45.08	3.23	(0 8 4)	48.91	1.30
(4 2 1)	41.64	0.71	(0 12 2)	45.08	2.11	(3 7 3)	49.01	2.99
(1 8 3)	41.65	5.73	(2 8 3)	45.26	0.44	(1 11 3)	49.12	5.07
(1 0 4)	41.68	0.47	(2 0 4)	45.29	0.71	(2 13 1)	49.27	1.74
(0 3 4)	41.69	0.18	(0 10 3)	45.32	0.01	(1 14 1)	49.31	2.91
(2 11 0)	41.8	0.19	(0 10 -3)	45.32	0.01	(1 13 2)	49.38	3.03
(1 1 4)	41.82	0.45	(0 6 4)	45.35	2.38	(4 6 2)	49.42	1.70
(0 11 2)	41.96	0.07	(4 2 2)	45.37	0.37	(4 8 1)	49.48	2.50
(4 4 0)	42.04	0.95	(2 1 4)	45.42	0.76	(2 12 2)	49.58	2.19
(1 2 4)	42.24	3.28	(2 2 4)	45.81	1.61	(3 10 2)	49.64	0.20
(4 3 1)	42.34	1.01	(1 13 1)	45.91	1.24	(2 10 3)	49.81	1.26
(3 9 0)	42.42	0.73	(4 6 1)	45.95	2.27	(2 6 4)	49.84	9.74
(1 12 1)	42.57	1.92	(3 5 3)	45.97	1.93	(1 8 4)	50	1.47
(3 0 3)	42.64	0.90	(4 3 2)	46.02	14.46	(5 1 0)	50.43	0.02
(0 4 4)	42.67	0.48	(2 12 1)	46.12	7.58	(4 9 0)	50.43	0.01
(3 1 3)	42.77	0.45	(3 10 1)	46.18	3.59	(4 -9 0)	50.43	0.01
(0 9 3)	42.77	0.61	(1 12 2)	46.23	0.39	(3 12 0)	50.52	0.94
(1 3 4)	42.93	0.31	(4 7 0)	46.44	0.03	(4 0 3)	50.62	2.09
(3 7 2)	43.07	3.05	(2 3 4)	46.46	0.83	(4 1 3)	50.74	1.48
(2 11 1)	43.07	0.08	(1 10 3)	46.47	0.51	(5 2 0)	50.79	0.03
(3 2 3)	43.18	0.08	(1 6 4)	46.5	1.33	(3 8 3)	50.83	2.51
(1 11 2)	43.19	0.37	(2 11 2)	46.7	0.45	(0 12 3)	50.83	1.45
(2 7 3)	43.26	0.03	(4 4 2)	46.92	2.68	(3 0 4)	50.86	6.37
(4 5 0)	43.27	1.29	(0 7 4)	47.03	0.06	(3 1 4)	50.98	2.86
(4 4 1)	43.3	1.68	(0 14 0)	47.06	0.00	(0 9 4)	50.98	0.90
(3 9 1)	43.67	1.19	(3 9 2)	47.27	9.93	(4 7 2)	50.99	0.41
(3 3 3)	43.86	0.83	(2 4 4)	47.35	8.61	(4 2 3)	51.1	3.43
(1 4 4)	43.87	2.83	(3 6 3)	47.38	0.95	(0 1 5)	51.28	2.53
(0 5 4)	43.89	0.27	(2 9 3)	47.45	1.39	(3 2 4)	51.34	3.86
(2 10 2)	43.95	5.75	(4 7 1)	47.61	1.52	(5 3 0)	51.39	0.34
(1 9 3)	43.98	1.64	(3 11 0)	47.69	0.53	(2 7 4)	51.4	0.40
(4 5 1)	44.51	2.14	(0 11 3)	48.01	0.00	(5 0 1)	51.41	1.33
(1 13 0)	44.71	1.57	(4 5 2)	48.05	0.62	(2 14 0)	51.43	0.23
(0 13 1)	44.74	0.01	(2 13 0)	48.14	1.01	(5 1 1)	51.53	0.64
(4 6 0)	44.75	1.93	(1 7 4)	48.15	0.18	(4 9 1)	51.53	0.06
(3 4 3)	44.79	0.90	(1 14 0)	48.18	0.04	(0 14 2)	51.57	0.04
(4 0 2)	44.84	0.80	(0 14 1)	48.21	0.24	(3 12 1)	51.62	0.35

APPENDIX C

DECONVOLUTION OF XRD PEAKS

Convolution of peaks in XRD patterns is a recurring phenomenon which happens when there is small distance between 2θ of adjacent peaks and/or the peaks are naturally wide as a result of small (i.e. nano) size crystallites. Convolution of peaks renders peak analysis, i.e. distinguish of existence of phases available in the product and calculation of phase composition, intricate. The case is more severe when at least one of the convoluted peaks belongs to a phase with low concentration in the phase mixture. Peak analysis softwares facilitate deconvolution of merged peaks. These softwares are also capable of calculation of peak characteristics like intensity, area underneath and full width at half maximum of peaks which are beneficial in evaluation of phase composition and primary crystallite size. Peak Fit™ version 4.11 is the software used to perform peak analysis in this study. To do peak analysis raw data extracted from XRD instrument is imported to the software. Next, the interval intended for analysis is determined to the software. The software generates the peaks cluster after performing peak smoothening and baseline subtraction. The generated peak is used to execute deconvolution. The idea for deconvolution is to create all possible peaks at their standard positions based on JCPDS cart and vary their widths and intensities so that the peaks cluster created from superimposition of these peaks show the best fit with respect to the generated peak. The criterion for successful fit is the R^2 calculated by software which should be as close as possible to 1.

As mentioned in 4.3.3, to find out the composition of the core-shell composites produced in experiments A to D* (refer for Table 3.3) the ranges from 21.0 to 22.5° and 28.5 to 31.5° were considered to be deconvoluted separately. Results of peaks deconvolution for product of experiment A was shown in Figure 4.11. Fit analyses results related to experiments B, C, D and D* are provided in this appendix.

The peaks characteristic data associated with each experiment can be used to calculate phase composition result of which are tabulated in Table C.1. The columns under "Deconvoluted Peak", Area, 2θ and Int. Area (which is area achieved by numerical integration of the peak) were extracted from peak characteristics data file. The columns under "Standard Peak" achieved from JCPDS cart (refer to Appendix A). The cluster between 28.5 to 31.5° includes two peaks of c-ZrW_2O_8 which are first peak (peak 1) and last peak (peak 5) of deconvoluted peaks. To calculate the composition of composites, peak 5 was used to calculated the composition of c-ZrW_2O_8. Compositions are calculated based on the following folmula:

$$Composition_i = ((Area_i/Intensity_i)\times 100) / \sum(Area_i/Intensity_i) \qquad (20)$$

In which:

$Composition_i$ (vol. %): composition of material i in the composite

$Area_i$ (%): Area underneath of deconvoluted peak of material i

$Intensity_i$ (%): Standard intensity of material i in JCPDS cart

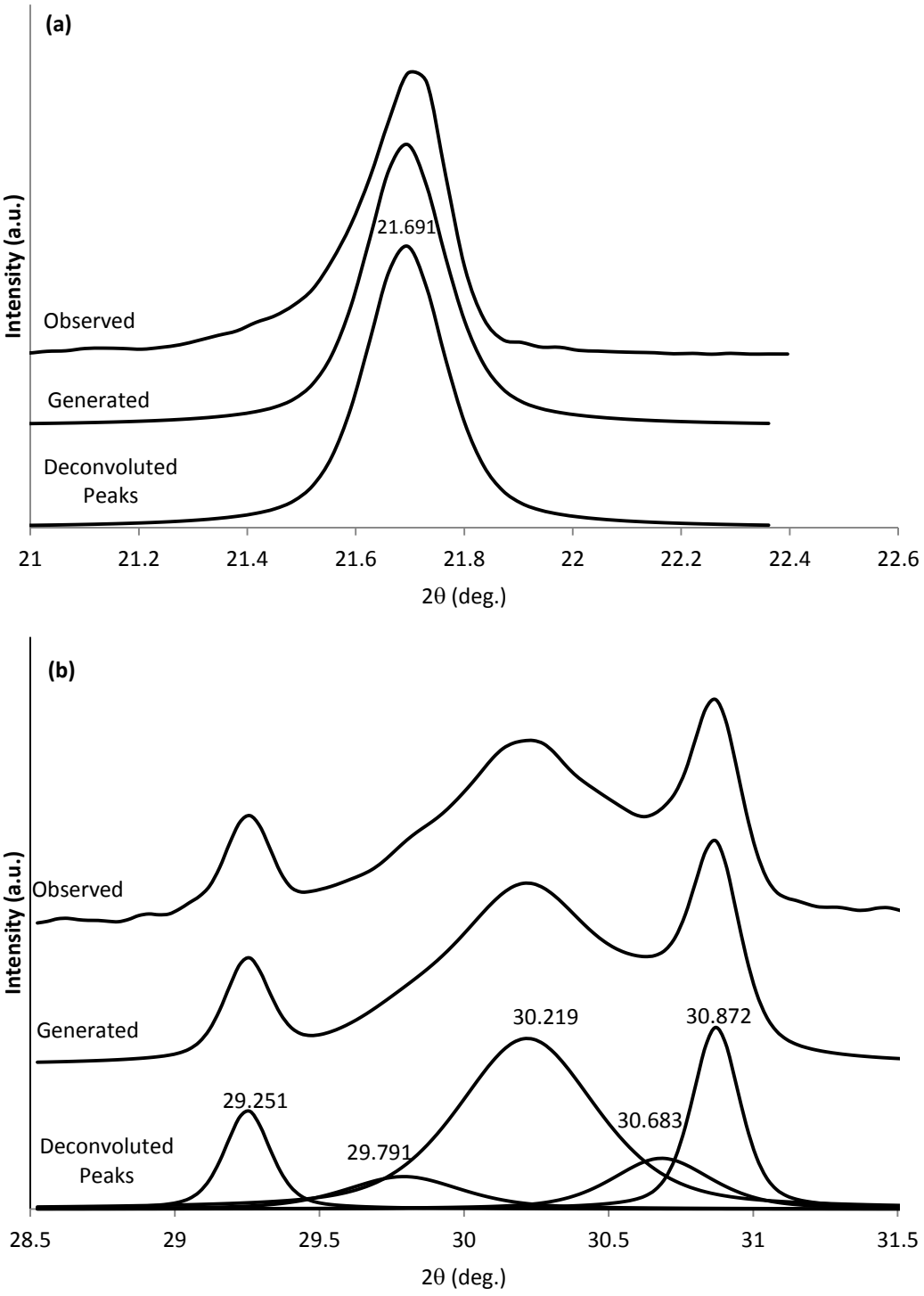

Figure C.1 Deconvolution analysis of experiment B. The observed peaks between 21.0 to 22.4° (a) and 28.5 to 31.5 (b) were generated and deconvoluted into two and five peaks respectively.

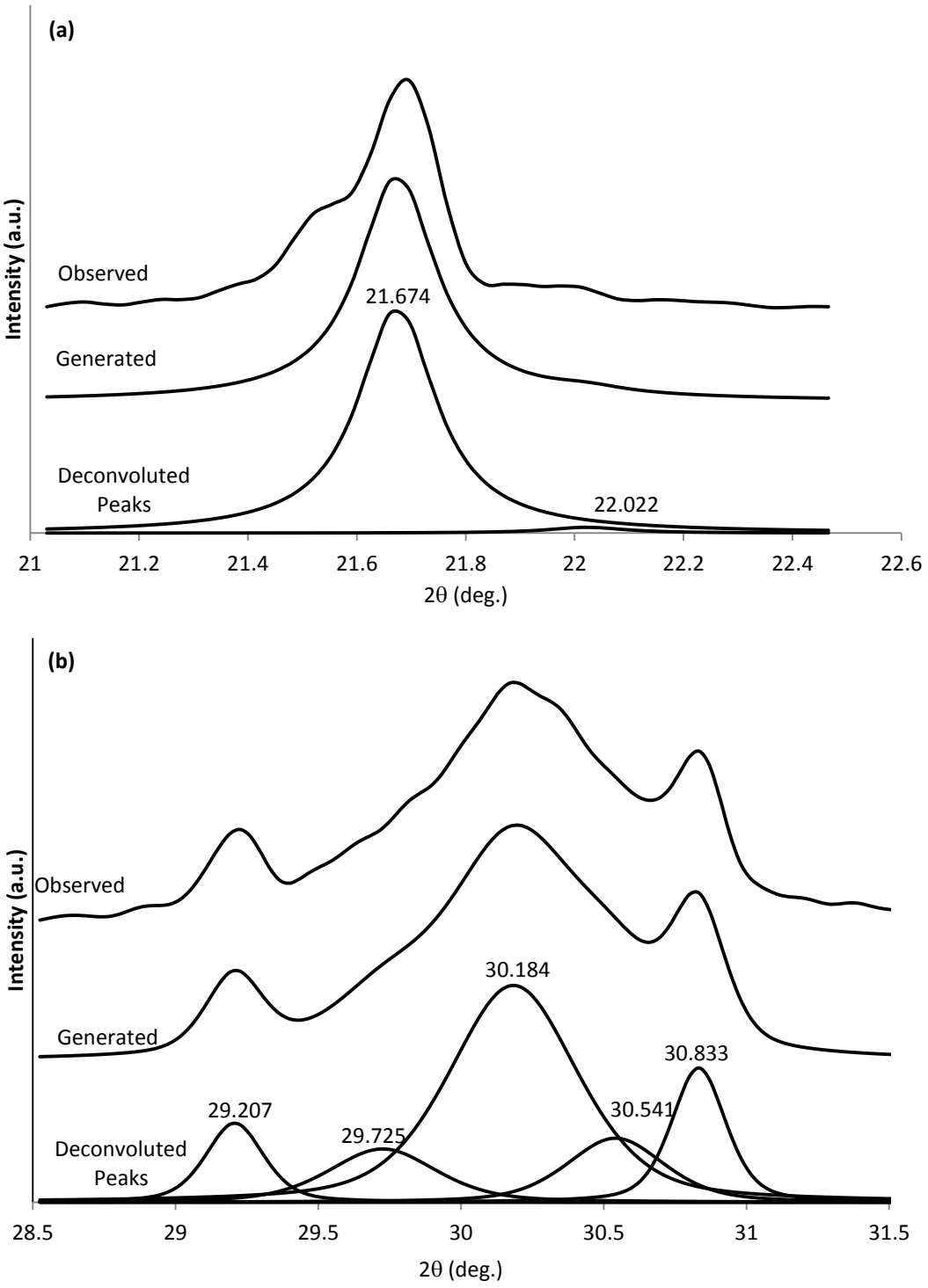

Figure C.2 Deconvolution analysis of experiment C. The observed peaks between 21.0 to 22.4° (a) and 28.5 to 31.5 (b) were generated and deconvoluted into two and five peaks respectively.

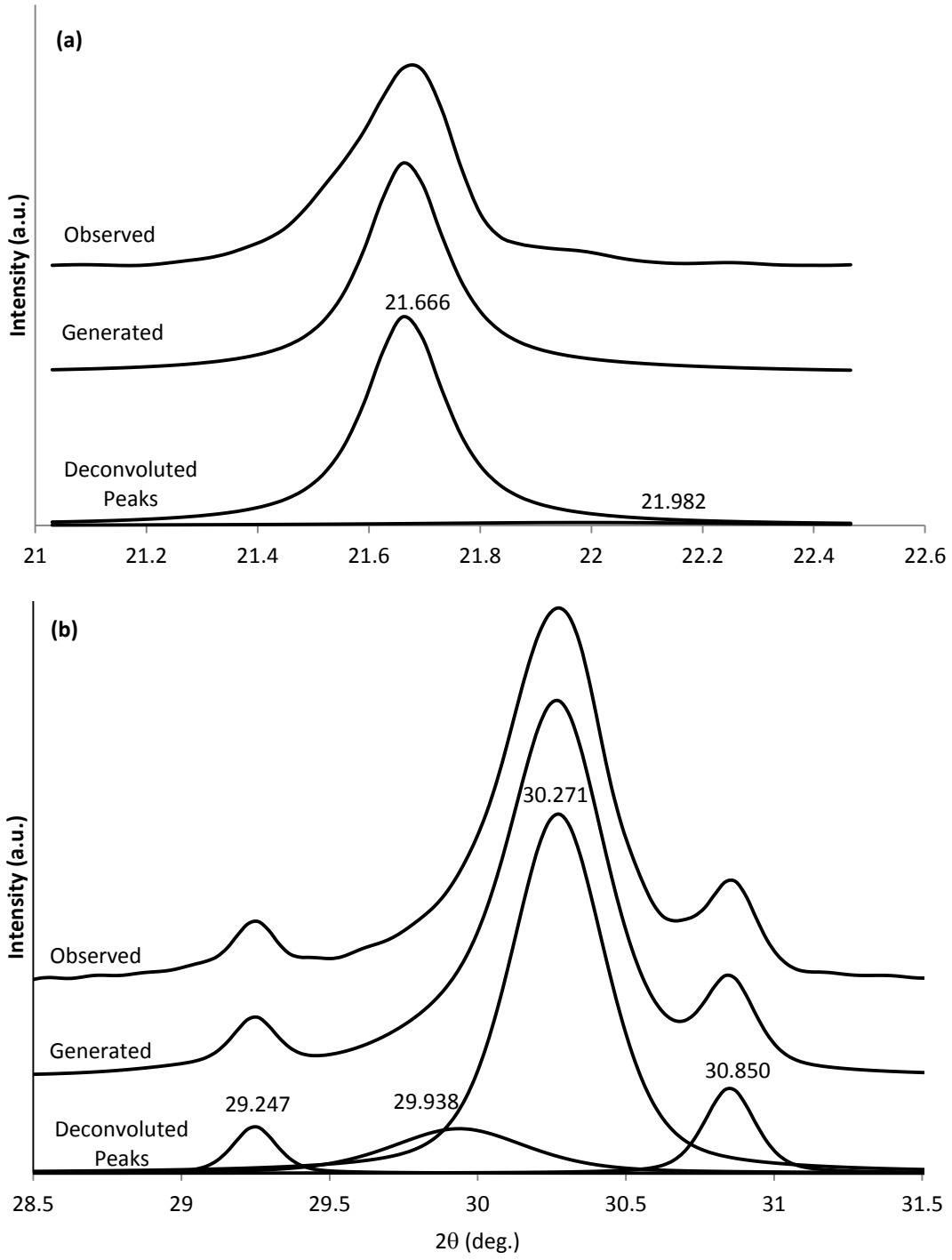

Figure C.3 Deconvolution analysis of experiment D. The observed peaks between 21.0 to 22.4° (a) and 28.5 to 31.5 (b) were generated and deconvoluted into two and five peaks respectively.

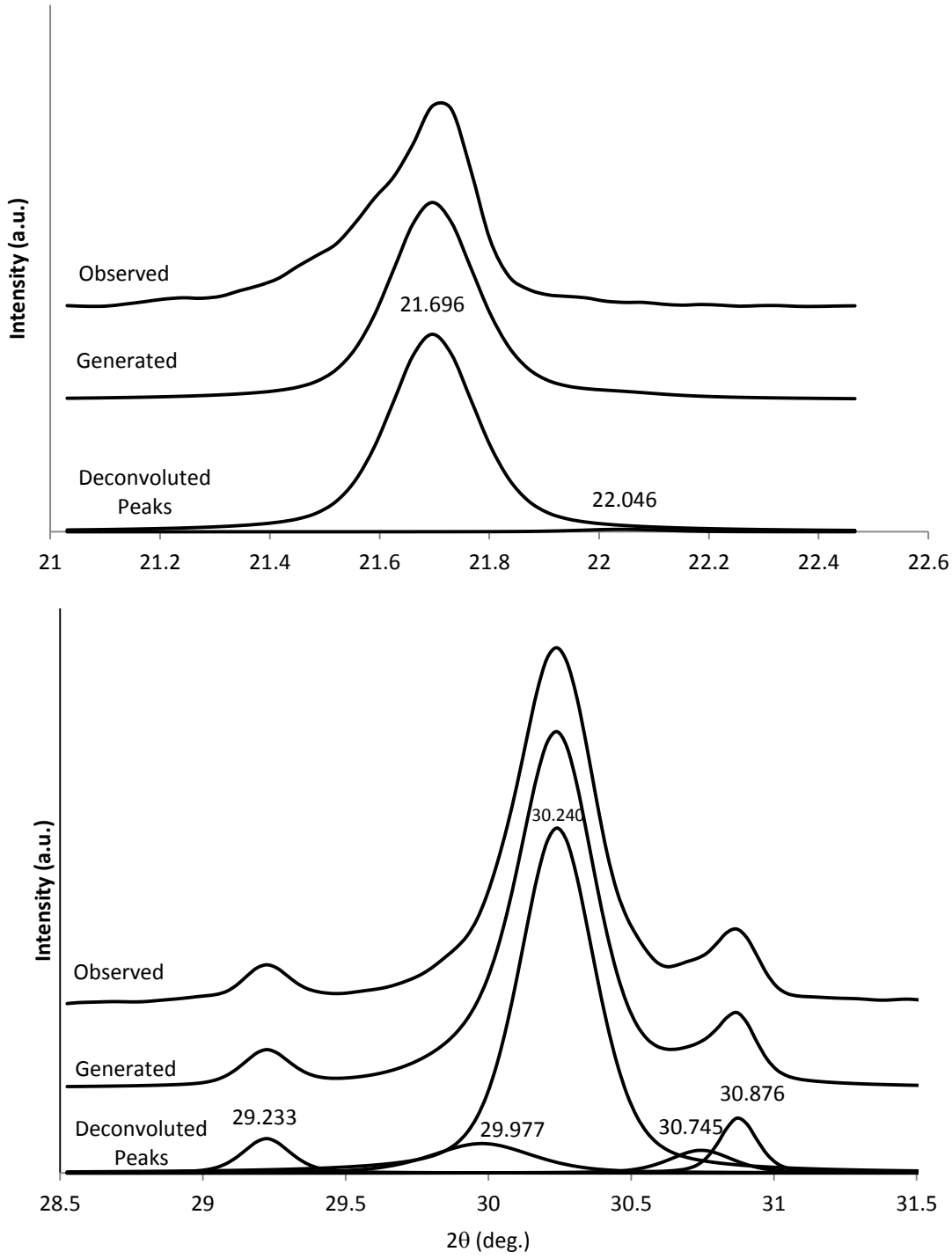

Figure C.4 Deconvolution analysis of experiment D*. The observed peaks between 21.0 to 22.4° (a) and 28.5 to 31.5 (b) were generated and deconvoluted into two and five peaks respectively.

Table C.1 Calculation pad of composites compositions produced in experiment A to D*.

A									
	Deconvoluted Peak			Standard Peak		Composition based on Area			
	Area	2θ	Int. Area[a]	Intensity	2θ	Peak5 for c-ZrW2O8			
	(%)	(Deg.)		(%)	(Deg.)	Area/ Intensity	Composition		
Peak 1(c-ZrW2O8)	9.88	29.18	250.02	10.00	29.18		(%)		ZrW2O8
Peak 2(γ-ZrW2O8)	12.24	29.86	305.19	24.00	29.79	0.51	24.17		59.72
Peak 3(t-ZrO2)	55.42	30.18	1399.35	100.00	30.17	0.55	26.27	(c/t)ZrO2	ZrO2
Peak 4(c-ZrO2)	4.43	30.63	112.09	100.00	30.51	0.04	2.10	0.08	40.28
Peak 5(c-ZrW2O8)	18.03	30.81	458.28	18.00	30.72	1.00	47.46	c-ZrW2O8/t-ZrO2	
		Total	2524.94			2.11	100.00	1.81	100.00
	Deconvoluted Peak			Standard Peak		Composition based on Area			
	Area	2θ	Int. Area[a]	Intensity	2θ	Area/ Intensity	Composition		
	(%)	(Deg.)		(%)	(Deg.)		(%)		
Peak 1(c-ZrW2O8)	97.62	21.63	2189.22	100.00	21.60	97.62	97.62	(o/c)ZrW2O8	
Peak 2(γ-ZrW2O8)	2.38	21.97	51.38	100.00	22.00	2.38	2.38	0.02	
		Total	2240.60			100.00	100.00		
B									
	Deconvoluted Peak			Standard Peak		Composition based on Area			
	Area	2θ	Int. Area[a]	Intensity	2θ	Peak5 for c-ZrW2O8			
	(%)	(Deg.)		(%)	(Deg.)	Area/ Intensity	Composition		
Peak 1(c-ZrW2O8)	9.93	29.25	245.70	10.00	29.18		(%)		ZrW2O8
Peak 2(γ-ZrW2O8)	8.29	29.79	199.67	24.00	29.79	0.35	16.97		59.48
Peak 3(t-ZrO2)	51.63	30.22	1234.84	100.00	30.17	0.52	25.38	(c/t)ZrO2	ZrO2
Peak 4(c-ZrO2)	11.03	30.68	267.28	100.00	30.51	0.11	5.42	0.21	40.52
Peak 5(c-ZrW2O8)	19.12	30.87	474.54	18.00	30.72	1.06	52.23	c-ZrW2O8/t-ZrO2	
		Total	2422.03			2.03	100.00	2.06	
	Deconvoluted Peak			Standard Peak		Composition based on Area			
	Area	2θ	Int. Area[a]	Intensity	2θ	Area/ Intensity	Composition		
	(%)	(Deg.)		(%)	(Deg.)		(%)		
Peak 1(c-ZrW2O8)	100.00	21.69	2204.76	100.00	21.60	100.00	100.00	(o/c)ZrW2O8	
Peak 2(γ-ZrW2O8)	0.00	-	0.00	100.00	22.00	0.00	0.00	0.00	
		Total	2204.76			0.00	100.00		

Table C.1 Continued.

C									
	Deconvoluted Peak			Standard Peak0		Composition based on Area			
	Area	2θ	Int. Area[a]	Intensity	2θ	Peak5 for c-ZrW2O8			
	(%)	(Deg.)		(%)	(Deg.)	Area/ Intensity	Composition		
Peak 1(c-ZrW2O8)	8.83	29.21	842.87	10.00	29.18		(%)		ZrW2O8
Peak 2(γ-ZrW2O8)	11.05	29.73	567.66	24.00	29.79	0.46	24.21		34.10
Peak 3(t-ZrO2)	53.85	30.18	2306.11	100.00	30.17	0.54	28.32	(c/t)ZrO2	ZrO2
Peak 4(c-ZrO2)	12.03	30.54	681.80	100.00	30.51	0.12	6.33	0.22	65.90
Peak 5(c-ZrW2O8)	14.08	30.83	1429.16	18.00	30.72	0.78	41.14	c-ZrW2O8/t-ZrO2	
		Total	5827.59			1.90	100.00	1.45	
	Deconvoluted Peak			Standard Peak		Composition based on Area			
	Area	2θ	Int. Area[a]	Intensity	2θ	Area/ Intensity	Composition		
	(%)	(Deg.)		(%)	(Deg.)		(%)		
Peak 1(c-ZrW2O8)	97.53	21.67	1508.24	100.00	21.60	97.53	97.53	(o/c)ZrW2O8	
Peak 2(γ-ZrW2O8)	2.47	22.02	37.81	100.00	22.00	2.47	2.47	0.03	
		Total	1546.04			100.00	100.00		
D									
	Deconvoluted Peak			Standard Peak		Composition based on Area			
	Area	2θ	Int. Area[a]	Intensity	2θ	Peak5 for c-ZrW2O8			
	(%)	(Deg.)		(%)	(Deg.)	Area/ Intensity	Composition		
Peak 1(c-ZrW2O8)	4.28	29.25	161.62	10.00	29.18		(%)		ZrW2O8
Peak 2(γ-ZrW2O8)	12.69	29.94	463.68	24.00	29.79	0.53	30.18		31.70
Peak 3(t-ZrO2)	71.83	30.27	2668.91	100.00	30.17	0.72	40.98	(c/t)ZrO2	ZrO2
Peak 4(c-ZrO2)	0.00	-	0.00	100.00	30.51	0.00	0.00	0.00	68.30
Peak 5(c-ZrW2O8)	9.10	30.85	342.37	18.00	30.72	0.51	28.83	c-ZrW2O8/t-ZrO2	
		Total	3636.57			1.75	100.00	0.70	
	Deconvoluted Peak			Standard Peak		Composition based on Area			
	Area	2θ	Int. Area[a]	Intensity	2θ	Area/ Intensity	Composition		
	(%)	(Deg.)		(%)	(Deg.)		(%)		
Peak 1(c-ZrW2O8)	93.91	21.67	1182.87	100.00	21.60	93.91	93.91	(o/c)ZrW2O8	
Peak 2(γ-ZrW2O8)	6.09	21.98	55.68	100.00	22.00	6.09	6.09	0.06	
		Total	1238.55			100.00	100.00		

Table C.1 Continued.

D*									
	Deconvoluted Peak			Standard Peak		Composition based on Area			
	Area	2θ	Int. Area[a]	Intensity	2θ	Peak5 for c-ZrW2O8			
	(%)	(Deg.)		(%)	(Deg.)	Area/ Intensity	Composition		
Peak 1(c-ZrW2O8)	4.75	29.22	147.65	10.00	29.18		(%)		ZrW2O8
Peak 2(γ-ZrW2O8)	8.75	30.00	268.01	24.00	29.79	0.36	24.22		33.33
Peak 3(t-ZrO2)	76.28	30.24	2363.64	100.00	30.17	0.76	50.70	(c/t)ZrO2	ZrO2
Peak 4(c-ZrO2)	4.19	30.75	129.90	100.00	30.51	0.04	2.78	0.05	66.67
Peak 5(c-ZrW2O8)	6.04	30.88	189.44	18.00	30.72	0.34	22.30	c-ZrW2O8/t-ZrO2	
		Total	3098.65			1.50	100.00	0.44	
	Deconvoluted Peak			Standard Peak		Composition based on Area			
	Area	2θ	Int. Area[a]	Intensity	2θ	Area/ Intensity	Composition		
	(%)	(Deg.)		(%)	(Deg.)		(%)		
Peak 1(c-ZrW2O8)	98.81	21.63	1231.63	100.00	21.60	98.81	98.81	(o/c)ZrW2O8	
Peak 2(γ-ZrW2O8)	1.19	21.72	14.76	100.00	22.00	1.19	1.19	0.01	
		Total	1246.39			100.00	100.00		

[a] "Int. Area" is the area calculated by numeric integration of deconvoluted peak.